An Experimental and Theoretical Investigation of Inverse Annular Film Flow and Dispersed Droplet Flow important under LOCA Conditions. 1980

Ottosen, Per

Publication date:
1982

Document Version
Publisher's PDF, also known as Version of record

Risø-R-424

RISØ

Risø-R-424

An Experimental and Theoretical Investigation of Inverse Annular Film Flow and dispersed Droplet Flow, important under LOCA Conditions

Per Ottosen

Risø National Laboratory, DK 4000 Roskilde, Denmark
July 1980

RISØ-R-424

AN EXPERIMENTAL AND THEORETICAL INVESTIGATION OF INVERSE ANNULAR FILM FLOW AND DISPERSED DROPLET FLOW, IMPORTANT UNDER LOCA CONDITIONS

Per Ottosen

Abstract. The flow regimes inverse annular film flow and the change to dispersed droplet flow have been studied through measurements of void fraction and heat flux.

Equipment for measuring the mean void fraction by the γ-ray absorption method has been developed. Measurements are presented of the axial void fraction distribution, the low flow inverse film boiling heat transfer, and the heat transfer to the dispersed droplet flow.

The experiments were performed in a heated glass tube with a nitrogen gas-liquid two-phase flow at 1 bar. The inlet mass flux was varied through a 10 to 120 kg/m²s range.

(Continue on next page)

July 1980
Risø National Laboratory, DK 4000 Roskilde, Denmark

Furthermore, a few measurements are presented of void fraction during inside reflood of a single heated steel tube with water.

The experimental data from the series of experiments using nitrogen as coolant have been compared with calculations with the one-diemnsional, six-equation computer code RISQUE-N2.

INIS descriptors: COMPUTER CALCULATIONS; DENSIMETERS; DROPLETS; FILM BOILING; FILM FLOW; FLOW MODELS; FLOWMETERS; GAMMA RADIATION; HEAT TRANSFER; LOSS OF COOLANT; NITROGEN; R CODES; REACTOR SAFETY; TUBES; TWO-PHASE FLOW; VOID FRACTION

UDC 621.039.588 : 532.529 : 536.24

This report is submitted to the Technical University of Denmark in partial fulfilment of the requirements for obtaining the lic.tech. (Ph.D.) degree.

ISBN 87-550-0689-2
ISSN 0106-2840

Risø Repro 1982

CONTENTS

1. INTRODUCTION

An essential part of the safety analysis of nuclear power reactors is the study of a postulated loss-of-coolant accident (LOCA) in a boiling-water reactor (BWR) or pressurized-water reactor (PWR).

A LOCA is the consequence of a break in the primary cooling system followed by a blow-down, where the reactor vessel is emptied of water within 10-30 seconds. The process of fission ceases rapidly after the accident due to an increasing void content in the core during blow-down.

The production of power after a LOCA will continue for hours at a level on the order of 5% of the normal reactor power that existed prior to the accident.

This power generation comes from the decay heat of both fission products and actinides.

After the accident, the reactor core must be cooled by an emergency core cooling system (ECCS). Failure or lack of effectiveness of the ECCS represents a dangerous situation, with a risk for core meltdown and release of radioactivity to the surroundings. If the fuel elements are not cooled, the remaining power generation combined with the stored heat in the fuel will cause the fuel temperature to rise rapidly. Within 100-200 seconds the uncooled fuel will reach a temperature on the order of 1200^{o}C, a region where the fuel cladding (zirconium) and steam can react chemically. This exothermic reaction accelerates the increase of temperature and leads in a few minutes to servere fuel element damage.

Two different systems of emergency core cooling are generally used: One is top spray cooling of the core and the other is a reflood system, where the core is flooded from the bottom.

The contents of the present report result from a study concentrated upon a stationary two-phase flow consisting of inverse annular film flow and the transition to dispersed droplet flow.

Non-steady inverse annular film flow, dispersed droplet and single phase gas flow are important flow regimes occurring in the region of post dry out which is characterized by a blow-down situation.

During reflooding the quench front (boundary between the wetted and dry part of the fuel cladding) travels upwards, mainly due to heat conduction in the walls of the hot fuel cladding. In order to make measurements of void fraction, flow rate, and heat transfer, it has been decided to limit the investigation to steady flow, where the quench front is at a fixed position.

The experimental part of this report contains a description of newly developed two-phase instrumentation used for flow measurements in cryogenic liquids and measurements of the mean void fraction. Further, an experimental facility using liquid nitrogen as coolant is described. The experimental results consist of mean void fraction measurements at several different axial positions accompanied by measurements of inlet flow, inlet subcooling, and heat flux. In a special series of experiments the heat flux has been measured separately in the inverse annular flow regime and in the droplet flow regime.

Finally, a few reflood experiments have been performed in a heated steel tube using water as coolant.

In the analytical part of this report the experimental data from the series of experiments using liquid nitrogen as coolant have been compared with calculations using the computer code RISQUE-N2.

2. INVERSE ANNULAR FILM BOILING AND DISPERSED DROPLET FLOW

Inverse annular film boiling is defined as a flow in a channel with wall temperature above that of minimum film boiling, where the liquid phase flows as a core in the middle of the channel separated from the wall by a thin film of gas.

Here the minimum film boiling temperature is defined as the minimum value of the wall temperature leading to a stable gas film between wall and liquid core.

Dispersed droplet flow is a flow regime with droplets moving in a continuous phase of gas.

2.1. Flow regimes during the reflooding phase after a LOCA

If a vertical heating tube with wall temperatures above the minimum film boiling temperature is flooded from the bottom, a quench front starts to travel upwards.

Depending on the heat flux in the wetted region and the inlet flow, one of the two flow patterns shown in Fig. 2.1 can occur.

When the inlet flow is small or the heat flux below the quench front is relatively high the flow is characterized by annular film boiling. If the inlet flow is large or the heat flux in the wetted region zero or small, the flow is characterized by inverse annular film boiling.

Above these two flow regimes the flow pattern changes to dispersed droplet flow. This flow is present until all droplets are evaporated leading to single-phase gas flow.

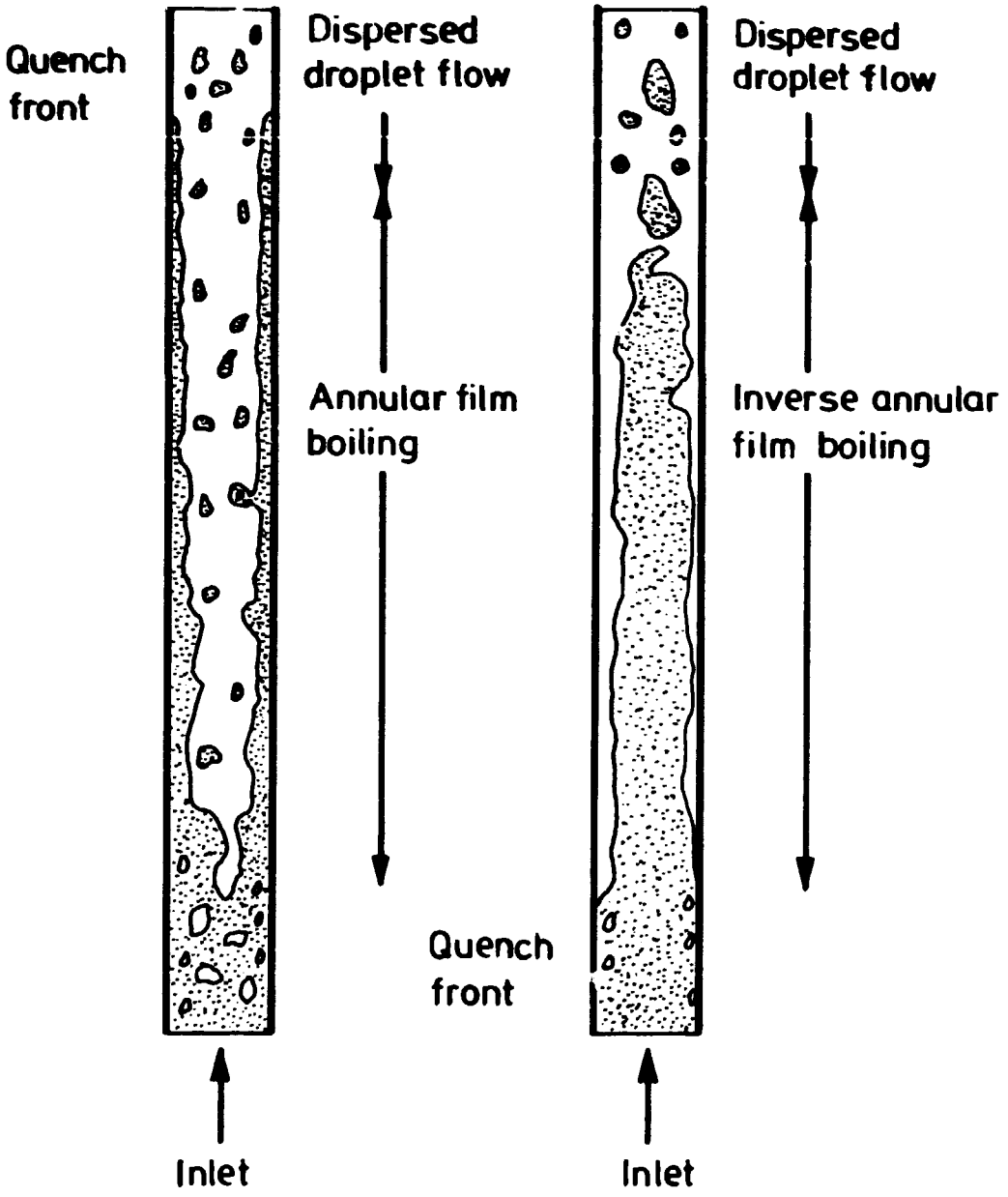

Fig. 2.1. Annular film boiling and inverse annular film boiling.

2.2. Important flow parameters

This section gives the definition of flow parameters used in succeeding chapters.

The total mass flow rate m (kg/s) is defined as

$$m = m_\ell + m_g, \qquad (2.1)$$

where

m_ℓ is the flow rate of liquid, and
m_g is the flow rate of gas.

The total mass flux G(kg/m²s) is defined as

$$G = \frac{m}{A} , \tag{2.2}$$

where A is the cross-sectional area of the flow channel.

For experimental purposes it is necessary to define the thermodynamic quality:

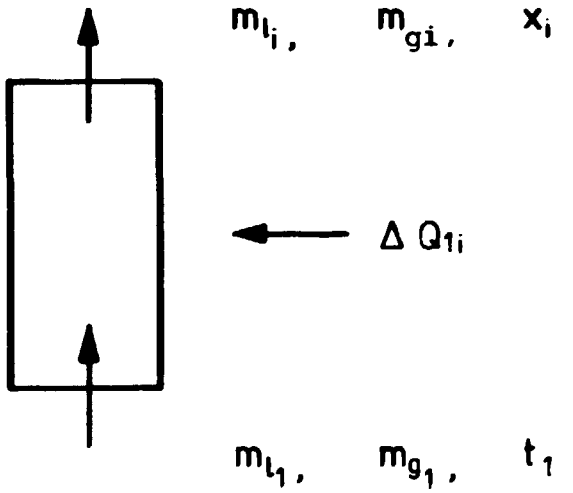

Fig. 2.2

If we assume thermodynamic equilibrium between the two phases at position "i", the equation of energy conservation used for the system expressed in Fig. 2.2 becomes

$$m_{\ell 1} c_p (t_{sat} - t_1) + (m_{\ell 1} - m_{\ell i}) h_{\ell g} = \Delta Q_{1i} . \tag{2.3}$$

Let the quality x_i be introduced by

$$x_i = \frac{m_{gi}}{m} \tag{2.4}$$

Here

$$m_{gi} = m_{\ell 1} - m_{\ell i} + m_{g1}$$

and

$$m = m_{\ell 1} + m_{g1}$$

Solving (2.3) and (2.4) for x_i gives

$$x_i = \frac{\Delta Q_{li} - m_{\ell l}\, c_p(t_{sat} - t_l) + m_{gl} h_{\ell g}}{h_{\ell g}\,(m_{\ell l} + m_{gl})} \,. \qquad (2.5)$$

In the case of subcooling at position "i" x_i becomes negative, and of superheating x_i becomes greater than one.

Another definition of quality is the physical quality that it is defined as

$$x = \frac{m_g}{m} \qquad (2.6)$$

The value of the physical gas quality defined as above is always within the limits of zero and one. Thermodynamic equilibrium has not been assumed.

As the physical gas quality is very difficult to measure, all values of quality presented in this report are thermodynamic ones calculated from Eq. (2.5).

If the two phases are in equilibrium and there is neither subcooling nor superheating, the two different types of quality are equal.

The mean void fraction (the void averaged over a cross-section og the channel) is defined as

$$\alpha = \frac{1}{A} \int_A \alpha(A)\, dA, \qquad (2.7)$$

where

$$\alpha(A) = \frac{1}{T} \int_T \alpha(t)\, dt, \text{ and}$$

$$\alpha(t) = \frac{dA_g(t)}{dA} \,.$$

The mean velocity of the gas V_g is defined as follows:

$$V_g = \frac{m_g}{\rho_g A \alpha} = \frac{m\, x}{\rho_g A \alpha} = \frac{G\, x}{\rho_g \alpha} \,, \qquad (2.8)$$

and the mean velocity of the liquid V_ℓ is defined:

$$V_\ell = \frac{\dot{m}_\ell}{\rho_\ell A(1-\alpha)} = \frac{\dot{m}(1-x)}{\rho_\ell A(1-\alpha)} = \frac{G(1-x)}{\rho_\ell(1-\alpha)} \quad . \tag{2.9}$$

The relative velocity V_r (m/s) is given as

$$V_r = V_g - V_\ell \quad . \tag{2.10}$$

2.3. Previous experimental and theoretical work

Compared to annular film flow, the flow regimes occurring in flow channels with wall temperatures above the minimum film boiling temperature have been investigated only in relatively few earlier experimental and theoretical works. The reason for this is that nuclear safety analysis is a new field of applied science. Annular film boiling is a well-known flow pattern occurring in coal- and oil-burning boilers, boiling-water reactors, and steam generators.

2.3.1. Annular film flow and inverse annular film flow

Among the many studies of annular film flow the following investigations are worth mentioning: Hewitt et al. (1965) performed annular film flow experiments at a pressure range of 1-4 bar. Würtz (1978) reports results obtained at a pressure range of 30-90 bar. Results obtained at low pressures are especially of interest for analysis of the reflood phase after a LOCA.

The studies of flow patterns occurring in the post dry-out region during an emergency core cooling can be divided into two different types: The first is a reflood of a hot electrically heated rod or tube, and the second is a reflood of bundles of internally heated rods simulating flooding of one or more real fuel elements.

Experiments performed with bundles are very expensive, and they do not give the detailed understanding of the physical phenomena

that is needed if one wants to develop models for use in advanced computer codes. However, these large scale experiments are important because they can prove that an actual bundle construction can be cooled by the ECCS.

Single tube experiments have been performed by Groeneveld et al. (1978), who have developed a method of obtaining flow film boiling data during bottom flooding of a hot tube.

Hall and Ardron (1980) have investigated the dispersed droplet flow in the dry-out region above the quench front. They use a glass tube heated by a resistance wire. This test section makes it possible to take high-speed motion pictures, and an analysis of these gives the distribution of droplet sizes and droplet velocities.

2.3.2. Post dry-out film boiling heat transfer

Correlations for stable film boiling heat transfer for high wall temperatures have been published both in experimental and theoretical works.

The first investigation known was performed by Bromley (1950). In this work the coefficient of heat transfer for natural convective film boiling in a horizontal tube is estimated.

Berenson (1961) derived an expression for the film boiling heat transfer from a horizontal surface by application of Taylor-Helmholtz hydrodynamic instability theory.

Later an average film boiling heat transfer coefficient was obtained by Munthe Andersen (1977) by analyzing the Helmholtz instability for the steam-liquid interface for low flow film boiling on a vertical surface.

A modified version of the correlation of Bromley (1950) was proposed by Rathmann and Kortakorpi (1979).

The correlations shown in Table 2.1 are not verified during bottom flooding experiments where other effects consisting of

Table 2.1. Summary of Film Boiling Heat Transfer Correlations

Reference	Correlation
Bromley (1950)	$h_1 = 0.62 \left(\frac{k_g^3 (\rho_\ell - \rho_g)\ g\ h_{\ell g}^*}{\nu_g\ L\ (T_w - T_{sat})} \right)^{1/4}$
Berenson (1961)	$h_2 = 0.425 \left(\frac{k_g^3\ (\rho_\ell - \rho_g)\ g\ h_{\ell g}^*}{\nu_g\ L\ (T_w - T_{sat})} \right)^{1/4}$
Rathmann and Kortakorpi (1979)	$h_3 = F_{sub}\ h_1 \left(\frac{(1-\alpha)}{2\pi L} \right)^{1/4}$
Munthe Andersen (1977)	$h_4 = c_1 \left(\frac{k_g^9 (\rho_\ell - \rho_g)^4\ g^4 h_{\ell g}^{*\ 2}}{\nu_g^4 \rho_g\ \sigma_\ell\ (T_w - T_{sat})^2} \right)^{1/11}$
	where $c_1 = \frac{4}{3} \left(\frac{\left(\frac{3n-1}{8}\right)^4}{\left(\frac{3\sqrt{3}}{2}\pi\right)^2} \right)^{1/11} = \begin{cases} 0.33 & \text{for } n = 0.5 \\ 0.55 & \text{for } n = 1.0 \end{cases}$

$h_{\ell g}^* = h_{\ell g} + 0.5\ c_{pg}\ (T_w - T_{sat})$, $L = \sqrt{\frac{\sigma_\ell}{g(\rho_\ell - \rho_g)}}$ and F_{sub} = effect of subcooling.

heat transfer by radiation and a moving quench front can spoil the measured results.

2.3.3. Methods of void fraction measurements

The void fraction is an important term in models for interfacial transfer of heat, momentum, and mass. As a consequence of this it is necessary to have equipment that can measure the mean void fraction.

Two-phase flow is easily disturbed by probes introduced in the flow channel, and therefore the correct way to measure the void fraction is by using a method that does not involve the introduction of probes into the flow.

The γ-absorption method for measuring voids is a technique which gives the values of the void fraction without disturbing the flow pattern. Using this method Evangelisti and Lapoli (1969) measured the void fraction in an annular channel.

Rouhani (1962) measured the void fraction by the (γ,n) reaction. Its only disadvantage is that the two-phase flow must consist of heavy water (D_2O).

A third technique utilizes neutron-scattering. Here a neutron source of high intensity is required; it is available only from a high-flux reactor. At a void fraction near 100% one obtains high accuracy. Freitas et al. (1980) made use of the neutron-scattering technique for measuring void fractions in a reflooded tube.

3. EXPERIMENTAL PART

The experimental part of this report is divided into four sections: The first describes the equipment for flow-rate and mean void fraction measurements. Then the experimental facilities are described. These consist of a test section for investigation of inverse annular film boiling and dispersed droplet flow in a two-phase flow of nitrogen, and a test section for study of reflooding of a heated steel tube with water. In the third section the experimental procedures are discussed. Finally, the measured data are shown graphically.

3.1. Two-phase instrumentation

In order to measure the important flow parameters of flow rate and mean void fraction, a new flow measurement technique and equipment to measure the mean void fraction have been developed.

3.1.1. Flow-rate measurement

The flow rate of a cryogenic liquid, as liquid nitrogen or another liquid with a temperature near the saturation temperature, is very difficult to measure with an ordinary technique using a venturi or orifice plate flowmeter.

To solve this problem the flow rate has been measured by a tension weighing cell. A container with the reservoir of fluid used as flow medium in the test section is hung in the weighing cell. This container can be connected to the test section by a flexible tube, or the test section can be placed directly in the container. The flow is established by pressing a suitable gas into the container.

The weighing cell has high accuracy and long-term stability, and the signal is directly available as input to a data logger system.

The flow rate is found with the data logger by periodically measuring the mass m and time t. The flow rate is then $\Delta m/\Delta t$, where Δm is the change in mass during the time Δt.

In practice, the data logger collects n paired values of m and t with a given interval Δt.

In the case of constant flow rate during the period Δtn, m, and t are related by the following expression:

$$m = a_1 t + a_0, \tag{3.1}$$

where the coefficient a_1 is the flow rate and a_0 the mass at $t = 0$.

When all pairs of data have become input, a_1 is estimated by linear regression. Then

$$a_1 = \frac{h_1}{h_2}, \tag{3.2}$$

where

$$h_1 = \Sigma mt - \frac{\Sigma m \Sigma t}{n}, \text{ and}$$

$$h_2 = \Sigma t^2 - \frac{(\Sigma t)^2}{n}.$$

The flow rate has remained constant in time if the coefficient of determination r^2 is close to unity. In this case

$$r^2 = \frac{h_1^2}{h_2 \quad h_3}, \tag{3.3}$$

where

$$h_3 = \Sigma m^2 - \frac{(\Sigma m)^2}{n}.$$

The standard deviation $s(a_1)^2$ of the flow rate a_1 is expressed by

$$s(a_1)^2 = \frac{h_3 - \frac{h_1^2}{h_2}}{(n-2)\ h_2}. \tag{3.4}$$

The weighing cell used for the experiments is a Tedea Serie 500 tension weigh cell with a capacity of 0 to 100 kg and a specified total error of less than 0.02%.

Using the method described above it has been possible to measure flow rates down to 1.0 g/s with a typical error of 1-2%.

3.1.2. Void measurements by γ-ray absorption

In this section the theory of void measurement by absorption of a beam of γ-rays is presented. Further, an analysis of possible systematic errors due to different flow regimes, fluctuations in void fraction, and dead time of the electronic equipment is given. The layout of the equipment for void fraction measurement is described. At last correlations for the measured value of the mean void fraction and the count rate are verified through calibration results.

3.1.2.1. The absorption law. In the case of a monoenergetic beam of γ-rays and slab geometry the absorption law becomes

$$dn = - \sigma \rho n \, dx, \tag{3.5}$$

where

n = count rate
σ = cross-section of absorption, and
ρ = density of absorber.

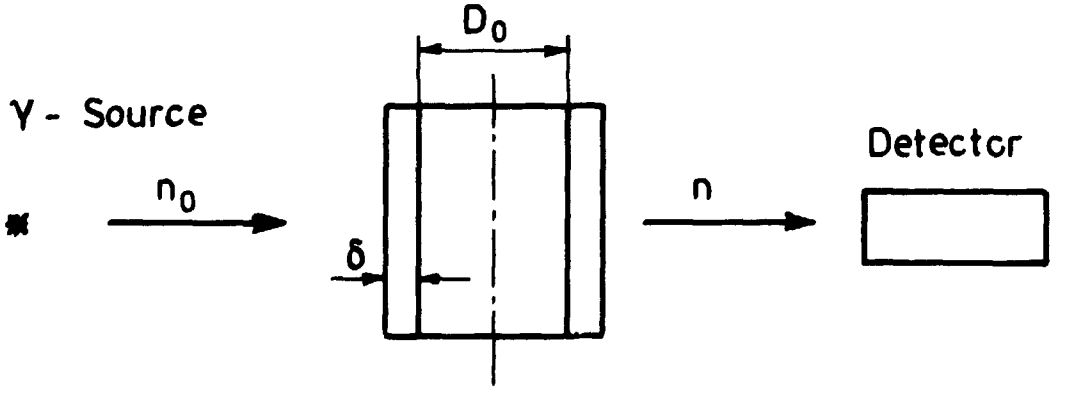

Fig. 3.1

If There is a constant mean void fraction α between the two walls of thickness δ, then by solving (3.5) we obtain:

$$\ln \frac{n}{n_0} = -\mu_w 2\delta - \mu_\ell (1-\alpha) D_0 - \mu_g \alpha D_0 , \tag{3.6}$$

where

$\mu = \sigma \rho$ = coefficient of absorption
D_0 = width of flow channel
δ = wall thickness
g = gas phase
ℓ = liquid phase, and
w = wall

In case gas i present in the channel, $\alpha = 1$; in this case Equation (3.6) becomes:

$$\ln \frac{n_g}{n_0} = - \mu_w 2\delta - \mu_g D_0 , \tag{3.7}$$

and with the liquid only, $\alpha = 0$, and

$$\ln \frac{n_\ell}{n_0} = - \mu_w 2\delta - \mu_\ell D_0 . \tag{3.8}$$

The contrast ratio $\frac{n_g}{n_\ell}$ is found by solving (3.7) and (3.8) for $\frac{n_g}{n_\ell}$, thus

$$\frac{n_g}{n_\ell} = e^{D_o \sigma (\rho_\ell - \rho_g)} . \tag{3.9}$$

Solving (3.6) and (3.8) for the void fraction α gives

$$\alpha = \ln \frac{n}{n_\ell} \; / \; \ln \frac{n_g}{n_\ell} \tag{3.10}$$

If the contrast ratio is small, $\frac{n_g}{n_\ell} \leq 1.15$ then a linear approximation to (3.10) can be made.

The result is

$$\alpha \simeq \frac{n - n_\ell}{n_g - n_\ell} \tag{3.11}$$

and the maximum error of α calculated in this way is about 0.017, under the above restriction.

3.1.2.2. Dependence on flow distribution at different pressure and channel widths. The mean void fraction α estimated by Equations (3.10) or (3.11) is strictly valid for only those slab-geometries where the absorbers, liquid phase, and gas phase are placed perpendicular to the direction of the γ-beam as shown in Fig. 3.2.

It is important to be convinced that the method applies when the two phases are distributed in a non-idealized way, corresponding to different flow regimes.

Consider then the following two different distributions of the two phases:

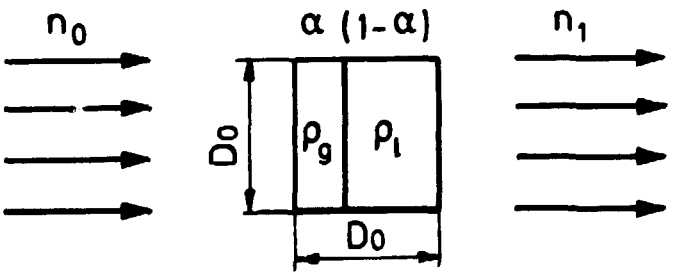

Fig. 3.2. Series distribution.

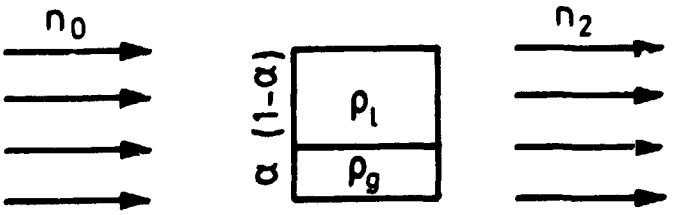

Fig. 3.3. Parallel distribution.

Figs. 3.2 and 3.3 show two extreme cases where the liquid and gas phases are distributed in series and parallel in relation to the direction of the incident γ-ray beam. The mean void fractions α are supposed to be equal in both cases.

By using the absorption law the values of n_1 and n_2 are given by the following expressions:

$$n_1 = n_0 \, e^{-\alpha D_o \sigma \rho_g} \, e^{-(1-\alpha) D_o \sigma \rho_\ell} \tag{3.12}$$

$$n_2 = n_0 \alpha e^{-D_o \sigma \rho_g} + n_0 (1-\alpha) \, e^{-D_o \sigma \rho_\ell}, \tag{3.13}$$

where

n_0 = virgin γ-intensity,
n_1 = measured γ-intensity in case 1, and
n_2 = measured γ-intensity in case 2.

Normally, the mean void fraction is calculated from Eq. (3.12) assuming this flow distribution to be the one most commonly occurring. The mean void fraction is then given by the following expression in terms of the count rates n_1, n_g, and n:

$$\alpha = \ln \frac{n_1}{n_\ell} \Big/ \ln \frac{n_g}{n_\ell} \, . \tag{3.14}$$

If the two phases are distributed as shown in Fig. 3.3 and the measured count rate n_2 is put into Eq. (3.14), one gets a value α_m, which differs from the real value α.

In order to see how the error $\Delta\alpha = \alpha_m - \alpha$ depends on the mean void fraction α, pressure p, cross-section of absorption σ, and channel width D_0, some typical examples are plotted in Figs. 3.4, 3.5, and 3.6.

$\sigma = 0.196$ cm^2/g is the cross-section of water at a photon energy of 0.06 Mev, and $\sigma = 0.0896$ cm^2/g is the cross-section at a photon energy of 0.6 Mev.

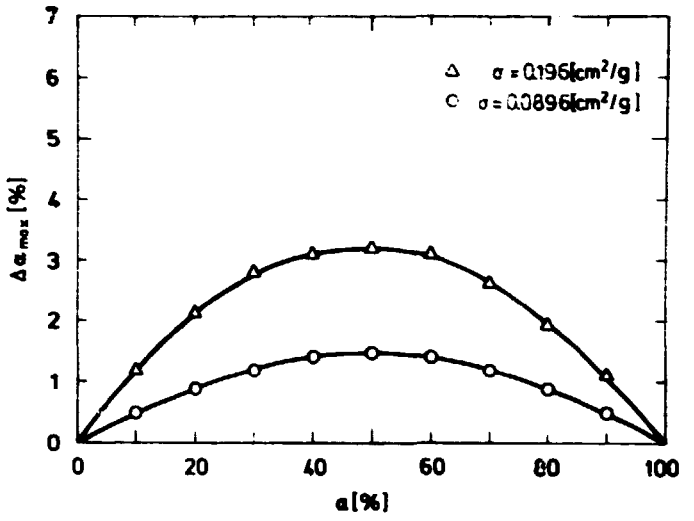

Fig. 3.4. Error Δα versus α, showing the dependence on flow distribution at photon energies of 0.06 Mev (σ = 0.196 cm^2/g) and 0.6 Mev (σ = 0.0896 cm^2/g). P = 1 bar and D = 1.36cm

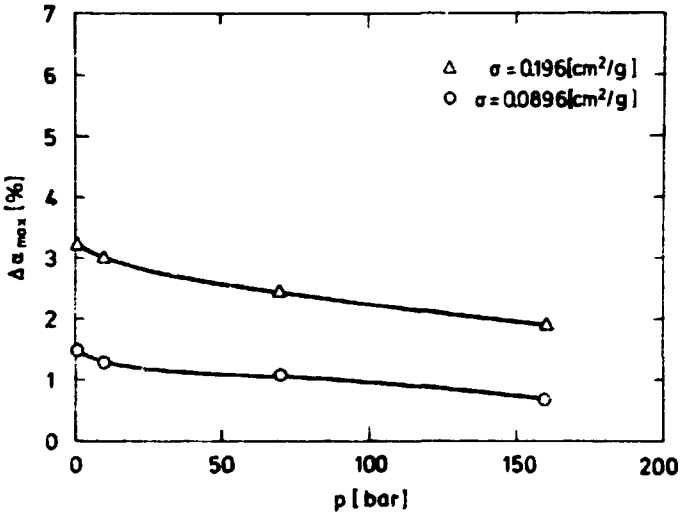

Fig. 3.5. Error $\Delta\alpha_{max}$ versus pressure p. (D = 1,36cm).

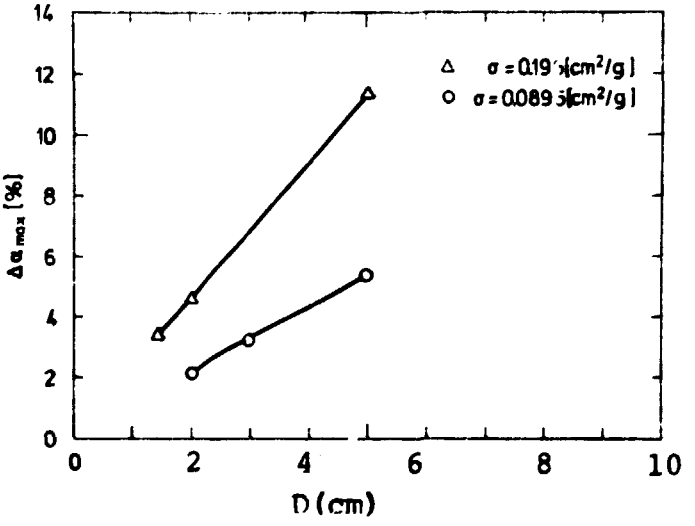

Fig. 3.6. Error $\Delta\alpha_{max}$ versus the channel width D. P = 1 bar.

The plot in Fig. 3.4 shows that the maximum error $\Delta\alpha_{max}$ occurs for $\alpha = 0.5$ and for the greatest value of σ.

Fig. 3.5 shows that the error $\Delta\alpha_{max}$ decreases when the pressure increases, and this is caused by the decreasing difference $\rho_\ell - \rho_g$ produced as the pressure increases.

In Fig. 3.6, $\Delta\alpha_{max}$ is plotted versus the channel width D_0 and the error $\Delta\alpha_{max}$ increases as D_0 increases.

The conclusion of this analysis is that the contrast ratio given as

$$\frac{n_g}{n_\ell} = e^{D_0\sigma(\rho_\ell-\rho_g)} \tag{3.15}$$

must be chosen rather close to unity, corresponding to a small value of the argument $D_0\sigma(\rho_\ell-\rho_g)$.

Typical values of the contrast ratio are

$$1.06 \leq \frac{n_g}{n_\ell} \leq 1.15.$$

3.1.2.3. Systematic errors caused by fluctuations in the void fraction. In all two phase-flows the void fraction commonly fluctuates. This is the case for bubble flow or droplet flow with large bubbles or droplets. At a given cross-section of the flow channel the void fraction generally can be described by the following expression:

$$\alpha_g(t) = \bar{\alpha}_g + \alpha_g'(t) \ , \tag{3.16}$$

where α_g' is a time-dependent residual term with zero mean and variance given by

$$\overline{\alpha_2'^2} = \frac{1}{T}\int_0^T \alpha_g'(t)^2 \, dt. \tag{3.17}$$

The true mean void fraction $\overline{\alpha_g}$ is given by

$$\overline{\alpha_g} = \frac{1}{T} \int_0^T \alpha(t)\, dt \,, \tag{3.18}$$

where $\alpha(t)$ can be approximated by

$$\alpha(t) = \frac{\Sigma_i \Delta d_i(t)}{D_0} \,. \tag{3.19}$$

The measured mean void fraction,

$$\overline{\alpha_m} = \frac{1}{T} \int_0^T \alpha_g(t)\, dt \tag{3.20}$$

is estimated from the static model

$$\overline{\alpha_m} = \ln \frac{n}{n_\ell} \Big/ \ln \frac{n_g}{n_\ell} \,. \tag{3.21}$$

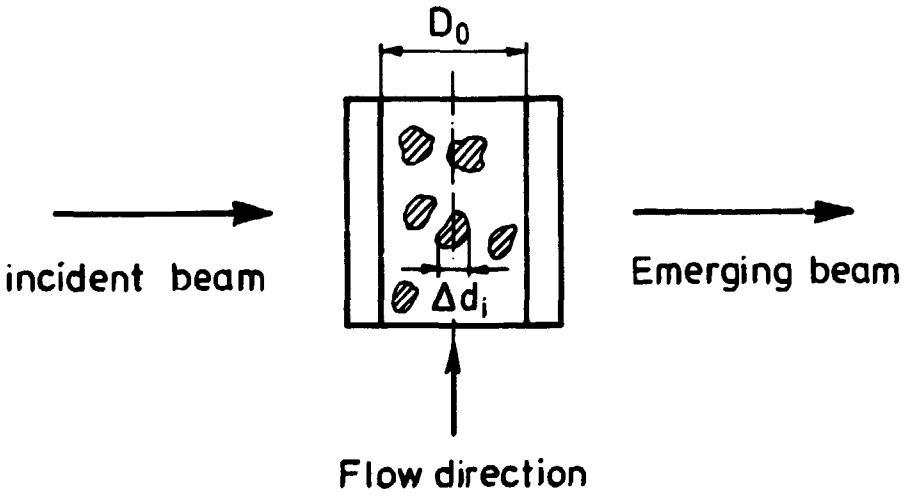

Fig. 3.7

Harms and Forrest (1971) and Barret (1974) obtain the following compact expression for the error caused by fluctuating voids:

$$\Delta\alpha = \overline{\alpha_m} - \overline{\alpha_g} \propto \frac{\overline{\lambda \alpha_g'^2}}{2} \,, \tag{3.22}$$

where $\lambda = \mu_\ell D_0 = \sigma \rho_\ell D_0$.

This expression shows that the static model gives an experimental value exceeding the actual averaged void $\overline{\alpha_g}$.

Suppose $\overline{\alpha_g'^2} \leq 0.25$, then

$$\Delta\alpha \leq \frac{\lambda \cdot 0.25}{2} \approx 0.125 \ln \frac{n_g}{n_\ell}$$

and it is therefore important to keep λ small.

In the case of nitrogen two-phase flow in a heated glass tube (D_o = 13.6 mm), or water two-phase flow in a heated steel tube (D_o = 14.0 mm) the maximum error becomes

nitrogen $\quad \frac{n_g}{n_\ell} \simeq 1.14 \Rightarrow \Delta\alpha \leq 0.017$, and

water $\quad \frac{n_g}{n_\ell} \simeq 1.06 \Rightarrow \Delta\alpha \leq 0.007$.

3.1.2.4. Dead-time estimate of the electronic counting system.

In order to avoid correcting for dead time of the electronic equipment, its value must be very small. The following gives a method of estimating the dead time for a given system.

The actual or corrected count rate is defined as follows:

$$i = \frac{n}{1 - \tau n}, \qquad (3.23)$$

where

- i = actual count rate (corrected),
- n = measured count rate (uncorrected), and
- τ = dead time of counting system.

For a given system, τ is fixed and here the error depends on the count rate n expressed as

$$\frac{i-n}{i} = \tau n \; ; \qquad (3.24)$$

this proves that the relative error is negligible at low count rates.

When it is necessary to use a high count rate, it is very important to know the value of τ.

τ can be measured by the two-absorber method as follows:
Let

$$\frac{i_1}{i_0} = e^{-D_1 \sigma \rho}, \text{ and } \frac{i_2}{i_0} = e^{-D_2 \sigma \rho}, \qquad (3.25)$$

where

i_0 = actual count rate, no absorber,
i_1, i_2 = actual count rate, absorber 1 and 2,
n_1, n_2 = measured count rate, absorber 1 and 2,
σ = cross section of absorption,
ρ = density, and
D_1, D_2 = thickness of absorber 1 and 2.

Solving (3.25) for τ gives:

$$\tau = \frac{n_2 k - n_1}{n_1 n_2 (k-1)} \qquad (3.26)$$

where $k = e^{(D_2 - D_1)\sigma\rho}$.

The count rates n_1 and n_2 are measured by means of two slabs of steel as absorber and an Am-241 γ-source.

The result is as follows, (For the typical experimental set-up):

n_1	n_2	D_1	D_2	σ	ρ
cps	cps	cm	cm	cm^2/g	g/cm^3
35,435	22,943	0.077	0.129	1.20	7.86

These values are put into Eq. (3.26) and the dead time of the system becomes

$$\tau = 4 \times 10^{-6} \text{ sec.}$$

The uncorrected void fraction α_{unc} may be written as

$$\alpha_{unc} = \ln \frac{n}{n_\ell} \Big/ \ln \frac{n_g}{n_\ell} \,, \tag{3.27}$$

and the corrected void fraction α_c is

$$\alpha_c = \ln \frac{n(1-\tau n_\ell)}{n_\ell(1-\tau n)} \Big/ \ln \frac{n_g(1-\tau n_\ell)}{n_\ell(1-\tau n_g)} \,. \tag{3.28}$$

Table 3.1.

		α_c		
n(cps)	α_{unc}	τ = 4 μs	τ = 10 μs	τ = 20 μs
31040	0.000	0.000	0.000	0.000
32000	0.230	0.229	0.225	0.208
33000	0.463	0.461	0.455	0.431
33500	0.577	0.574	0.569	0.544
34500	0.799	0.798	0.794	0.777
35427	1.000	1.000	1.000	1.000

n_ℓ and n_g are assumed to be 31040 and 35427.

The conclusion of the example in the table above must be that if $\tau \leq 4$ μs the max error $\Delta\alpha = \alpha_{unc} - \alpha_c < 0.005$ is negligible and it is unnecessary to use the more complicated expression (3.28).

If the dead time τ is smaller, then it is possible to use the system at high count rates, and this is very important if it is necessary to limit a single counting period.

Every count has to give a number N well above 500,000 and the reason for this is that the photons from a γ-source are Poisson distributed.

This leads to a deviation of N of magnitude $\sqrt{N}$. As the contrast ratio $\frac{n_g}{n_\ell}$ must be rather small, as shown above, it becomes necessary to demand a very small value of $\frac{\sqrt{N}}{N}$.

3.1.2.5. Layout of equipment for void fraction measurement. The equipment for the void fraction measurement consists basically of a γ-source placed at one side of the flow channel, and a NaI detector placed on the opposite side. Before entering the flow channel the beam of γ-rays passes through a collimator, which produces a beam of γ-rays covering the whole diameter of the flow channel. The emerging beam is measured by the NaI crystal of diameter about two times that of the channel.

Two different systems have been designed: one using a 100 mC Am-241 γ-source, and another a 1 mC Cs-137 γ-source.

The first system utilizes Am-241 because this isotope has a well-defined energy peak at 0.06 Mev, and the photons of this peak therefore function as a monoenergetic beam. Further, an energy of 0.06 Mev leads to a suitable contrast ratio $\frac{n_g}{n_\ell}$ near 1.10, when one wants to measure the void fraction in a two-phase flow of nitrogen taking place in a heated glass tube. Fig. 3.8 shows the mechanical arrangement.

Fig. 3.8. Void fraction measuring system using Am-241.

When it is necessary to measure the mean void fraction in a two-phase flow of water within a heated steel tube, it is not possible to use Am-241 as γ-source because of the high coefficient of γ-absorption in steel at 0.06 Mev. Therefore a second system has been designed employing a Cs-137 γ-source which has a single peak at 0.60 Mev. The drawback of using a source at a higher energy is that the contrast ratio is reduced. The shielding of the source for health physical reasons also demands a rather heavy shielding of lead. This system is shown in Fig. 3.9.

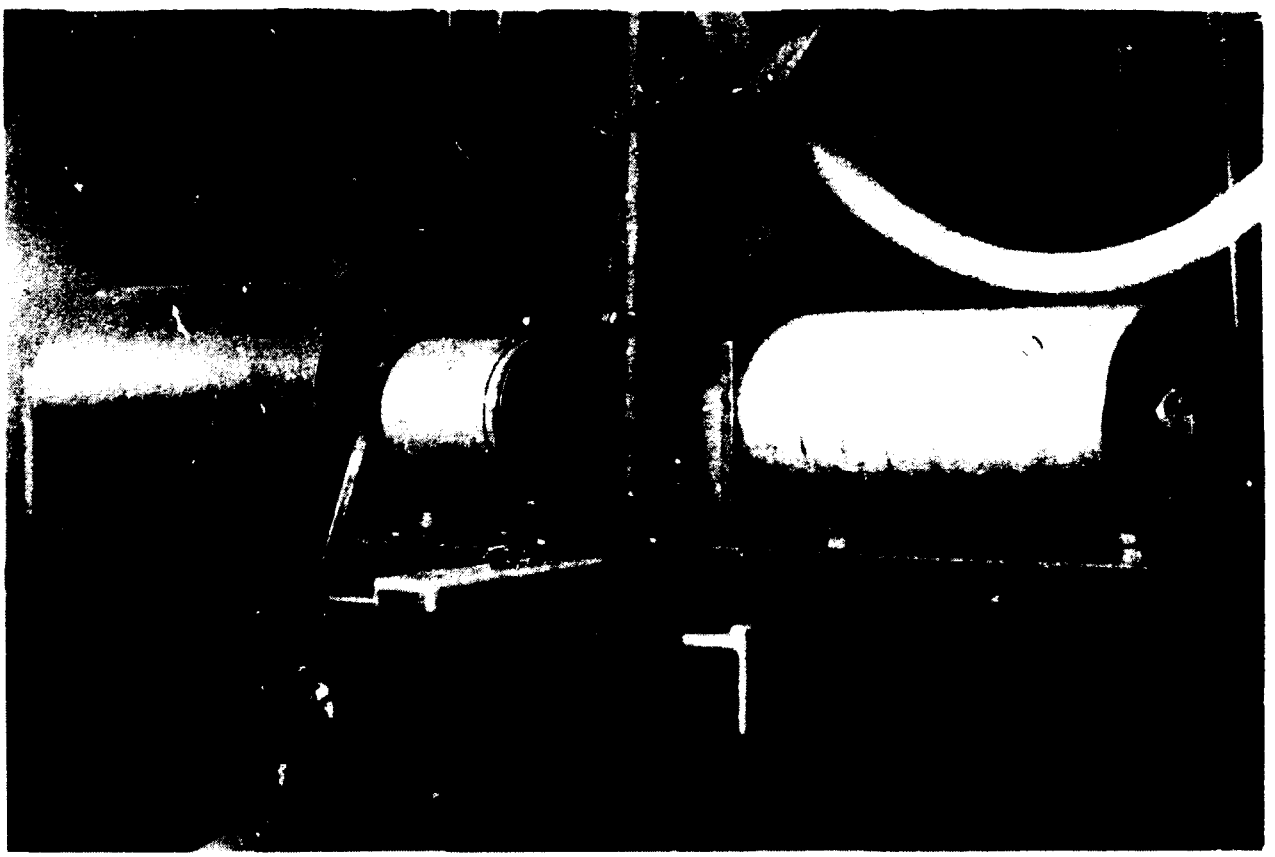

Fig. 3.9. Void fraction measuring system using Cs-137.

The diagram in Fig. 3.10 shows how the electronic system is connected to the detector.

The two oscilloscope photos in Figs. 3.11 and 3.12 show the output signals from the amplifier and analyzer.

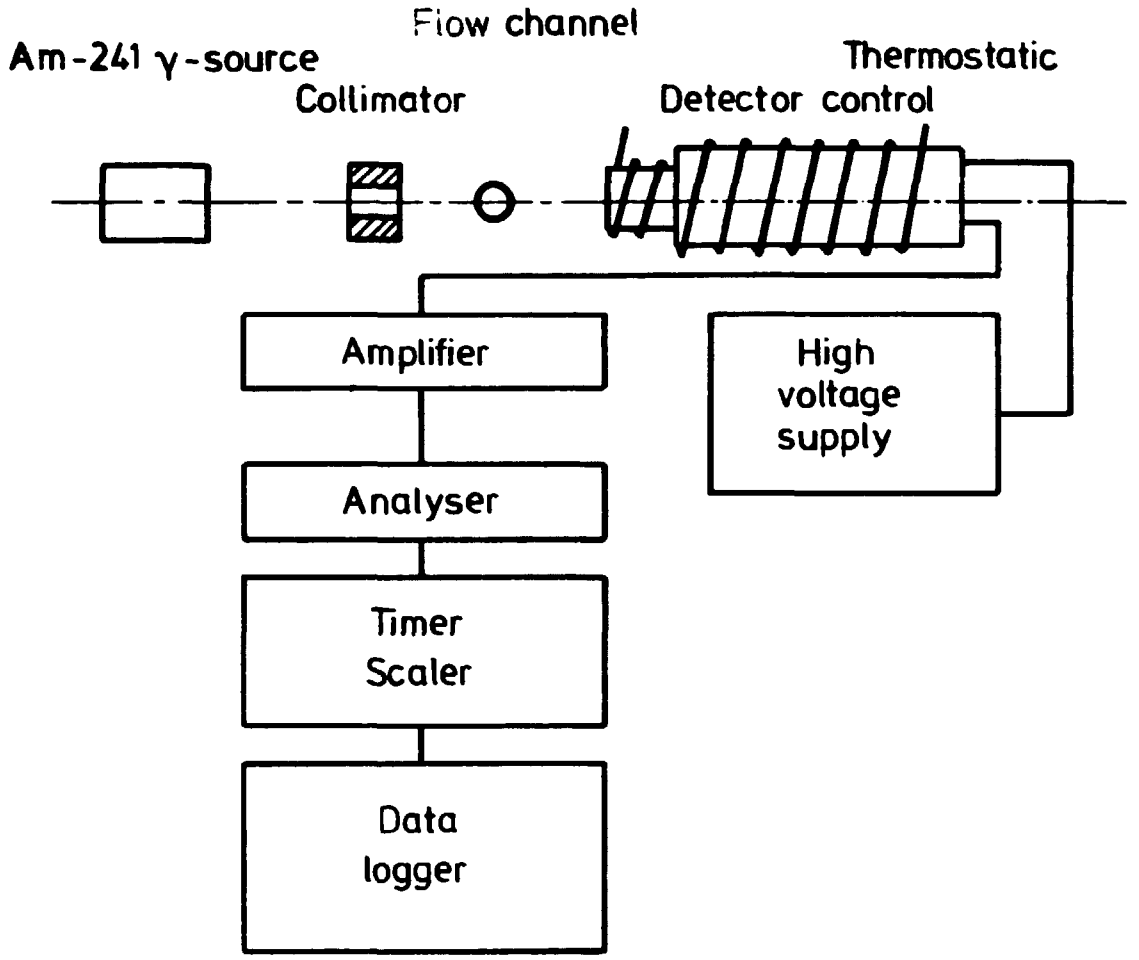

Fig. 3.10. System layout.

The longest period of dead time in the electronic system is in the amplifier and, as seen in Fig. 3.11, the dead time is of 4.0 μs magnitude. This agrees well with the result achieved by the two-absorber method given in Sec. 3.1.2.4.

It has been necessary to keep the temperature of the detector constant in order to avoid drift in the highly precise and stable counter system.

2 Volt/div.

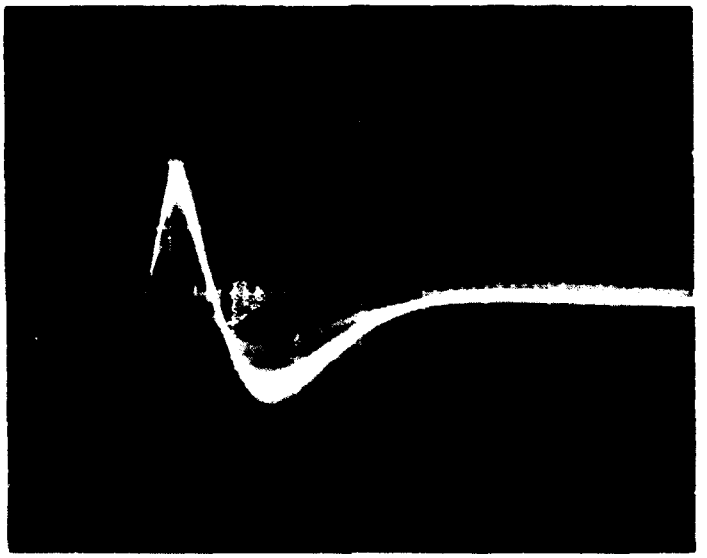

0.06 Mev peak
0.023 " "
Am 241

1 μsec/div.

Fig. 3.11. Bipolar output amplifier.

1 Volt/div.

1 μsec/div.

Fig. 3.12. Output analyzer.

The thermostatic control system is able to keep the temperature within a limit of $\pm$ 0.1°C which is enough to keep the error on the count rate less than 1 0/00.

If the detector is operated in a place where a strong magnetic field is present which is common in the case of electrically heated steel tubes, it is necessary to place a rather thick-walled iron tube around the detector tube. This is especially true in shielding the photo multiplier tube against the field. This is in addition to the built-in mu-metal magnetic shield, which, although possessing a high shield-factor, saturates at relatively low magnetic field values.

3.1.2.6. Calibration results. In order to test the void fraction measuring equipment some calibration tests have been performed. The inverse annular film boiling test facility, using liquid nitrogen as coolant, consists of a glass tube heated by an annular flow of water. Accordingly, the calibration tests are performed by means of the same sort of flow channel. As the test section is made of glass, Am-241 is employed as γ-source.

In order to verify the applicability of the method for void measurement of steam-water flows taking place in a steel tube, a second calibration test has been performed with Cs-137 as γ-source. The wall thickness of the steel tube used is 1.0 mm.

In both calibration tests perspex rods and tubes have been used as absorbent material to simulate the liquid phase. The diameters and wall thicknesses of the calibration absorbers were measured accurately to within an error of 0.001 mm. Thus, the real mean void fraction α can be computed as follows:

$$\alpha = \frac{A - A_{perspex}}{A} , \qquad (3.29)$$

where

A = cross-sectional area of filled flow channel, and

$A_{perspex}$ = cross-sectional area of perspex absorber rod or tube.

Tables 3.2 and 3.3 list the calibration results in detail. $\bar{N}$ is the mean value of n counts, and s is the experimental value of the standard deviation calculated according to the formula

$$s = \sqrt{\frac{\Sigma (N_i - \bar{N})^2}{n-1}} \cdot \qquad (3.30)$$

Generally n is limited to six. The value of s has to be near the theoretical value $\sqrt{\bar{N}}$ because the photons from a γ-source are Poisson distributed.

α is the known void fraction given by Eq. (3.29) α_{mo} is the measured void fraction calculated by the linear correlation

$$\alpha_{mo} = \frac{N - N_\ell}{N_g - N_\ell} \qquad (3.31)$$

$\alpha_{m\ell}$ is the measured void fraction calculated by the correlation

$$\alpha_{m\ell} = \ln \frac{N}{N_\ell} \Big/ \ln \frac{N_g}{N_\ell} \qquad (3.32)$$

These two correlations are identical with the exact results obtained for slab geometry. However, they are approximations to more complex solutions which can be derived for tubular geometry.

The solutions for tubular geometry are difficult to use because it is impossible to express in a simple form α explicitly as a function of N, N_g and N_ℓ.

In the case of small diameter of the flow channel as here, experimental results show that the application of Eg. (3.32) gives results within the error limits of the electronic equipment.

In the case of a test section made of glass and Am-241 as γ-source, the actual contrast ratio is

$$\left(\frac{n_g}{n_\ell}\right)_{\text{Am-241}} = 1.141;$$

in the case where the test section is a steel tube and Cs-137 is the γ-source, the contrast ratio becomes

$$\left(\frac{n_g}{n_\ell}\right)_{Cs\text{-}137} = 1.053$$

In both cases the diameter of the flow channels are identical, and as expected the contrast ratio becomes rather small in the case of a steel test section due to the higher energy of a Cs-137 γ-source compared with an Am-241 γ-source.

Fig. 3.13 shows a plot of measured count rate n versus the known void fraction α. It appears that this plot results in a nearly linear correlation between α and n.

In Figs. 3.14 and 3.15 the measured void fraction $\alpha_{m\ell}$ is plotted against the known void fraction α. It appears that the known value α and the measured value calculated according to Eq. (3.32) are in good agreement.

Consequently, this equation is used for evaluating the void fraction when $\bar{N}, \bar{N}_g$ and $\bar{N}_\ell$ are measured.

The results from the two different cases of calibration measurements indicate that the measured mean void fraction is independent of void distribution.

Fig. 3.16 shows a plot of the measured void fraction α_{ml} versus different orientations of a half-moon-shaped absorber rod. As mentioned before the conclusion of the result shown must be that the method is flow-regime independent within the error limits of the electronic equipment and the experimental method.

Table 3.2. Calibration Results AM-241

Perspex absorber	diameter mm	α	$\bar{N}$	s	$\alpha_{mo} = \frac{n-n_\ell}{n_g-n_\ell}$	$\alpha_{ml} = \frac{\ln n/n_\ell}{\ln ng/n_\ell}$
rod S13	13.066	0.000	620 789	405	0.000	0.000
rod S12	12.054	0.149	632 813	680	0.137	0.145
rod S11	11.003	0.291	645 094	799	0.277	0.290
rod S10	9.918	0.424	656 296	496	0.404	0.420
rod S9	9.035	0.522	664 504	395	0.498	0.514
rod S8	7.940	0.631	674 404	540	0.611	0.626
rod S7	7.019	0.711	681 373	183	0.690	0.704
rod S6	6.055	0.785	688 780	1 396	0.774	0.786
rod S5	5.028	0.852	695 029	511	0.846	0.854
rod S4	4.002	0.902	694 580	750	0.897	0.903
rod S3	2.968	0.948				
rod S2	2.053	0.975				
rods S3 + S2	10.141	0.924	701 880	675	0.924	0.928
tube R10,6	6.070	0.613	673 270	669	0.598	0.613
	10.058					
tube R10,7	7.038	0.698	682 241	242	0.700	0.714
empty	0.000	1.000	708 545	659	1.000	1.000

Table 3.3 Calibration Results Cs-137

Perspex absorber	diameter mm	α	$\bar{N}$	s	$\alpha_{m0} = \frac{n-n_\ell}{n_g-n_\ell}$	$\alpha_{m1} = \frac{\ln n'/n_\ell}{\ln n_g/n_\ell}$
rod S13	13.066	0.000	209 707	405	0.000	0.000
rod S12	12.054	0.149	211 269	481	0.141	0.144
rod S11	11.003	0.291	212 722	499	0.273	0.278
rod S10	9.918	0.424	213 964	326	0.384	0.391
rod S9	9.035	0.522	215 322	282	0.508	0.514
rod S8	7.940	0.631	216 714	472	0.633	0.639
rod S6	6.055	0.785	218 355	504	0.782	0.786
rod S4	4.002	0.902	219 661	960	0.900	0.902
tube R10, 6	10.141 6.070	0.613	216 158	290	0.583	0.589
tube R10, 7	10.058 7.038	0.698	217 235	711	0.681	0.686
empty	0.000	1.000	220 768	266	1.000	1.000

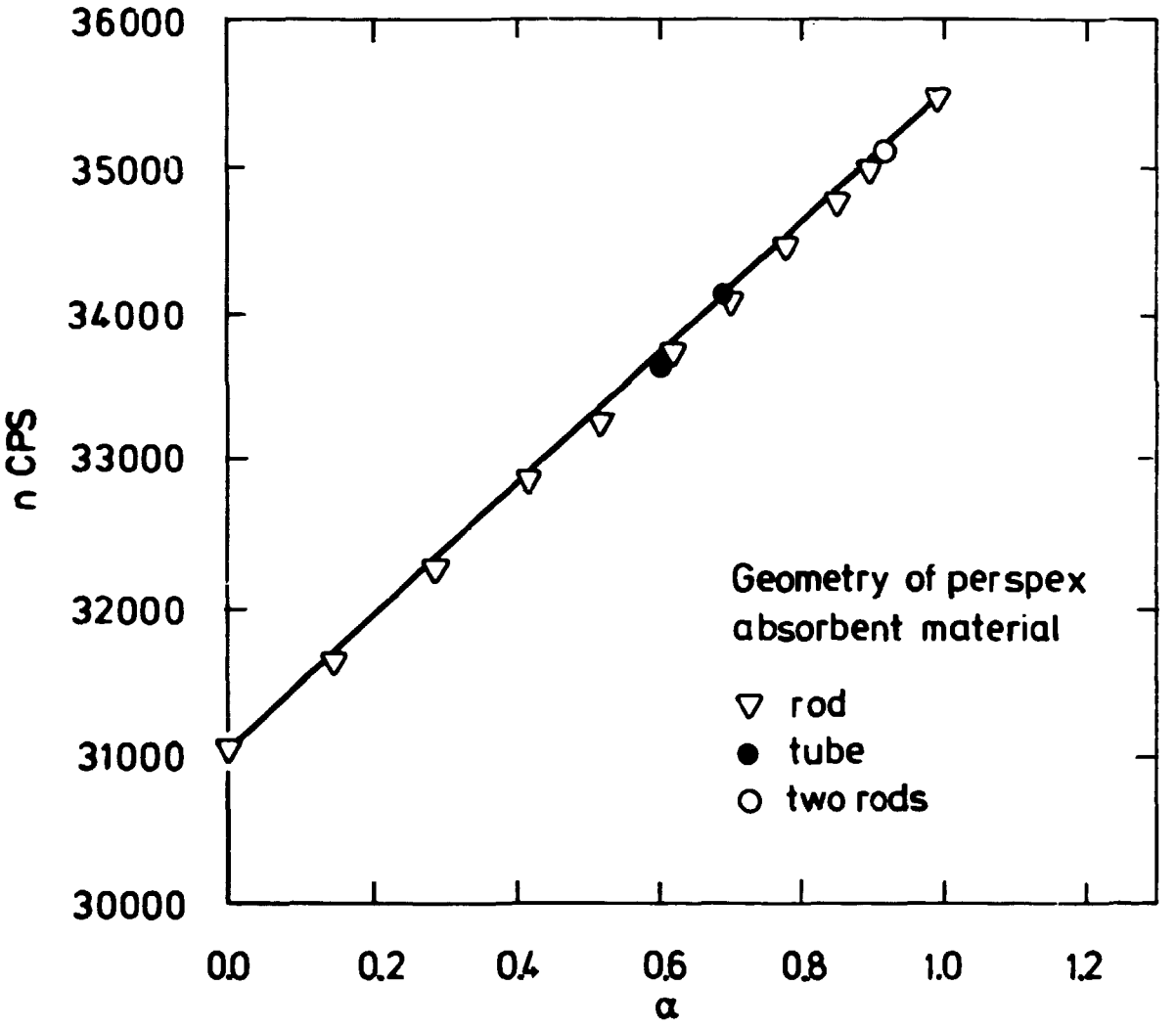

Fig. 3.13. Measured count rate n versus the known void fraction α. The γ-source is Am-241 and the test section is made of glass.

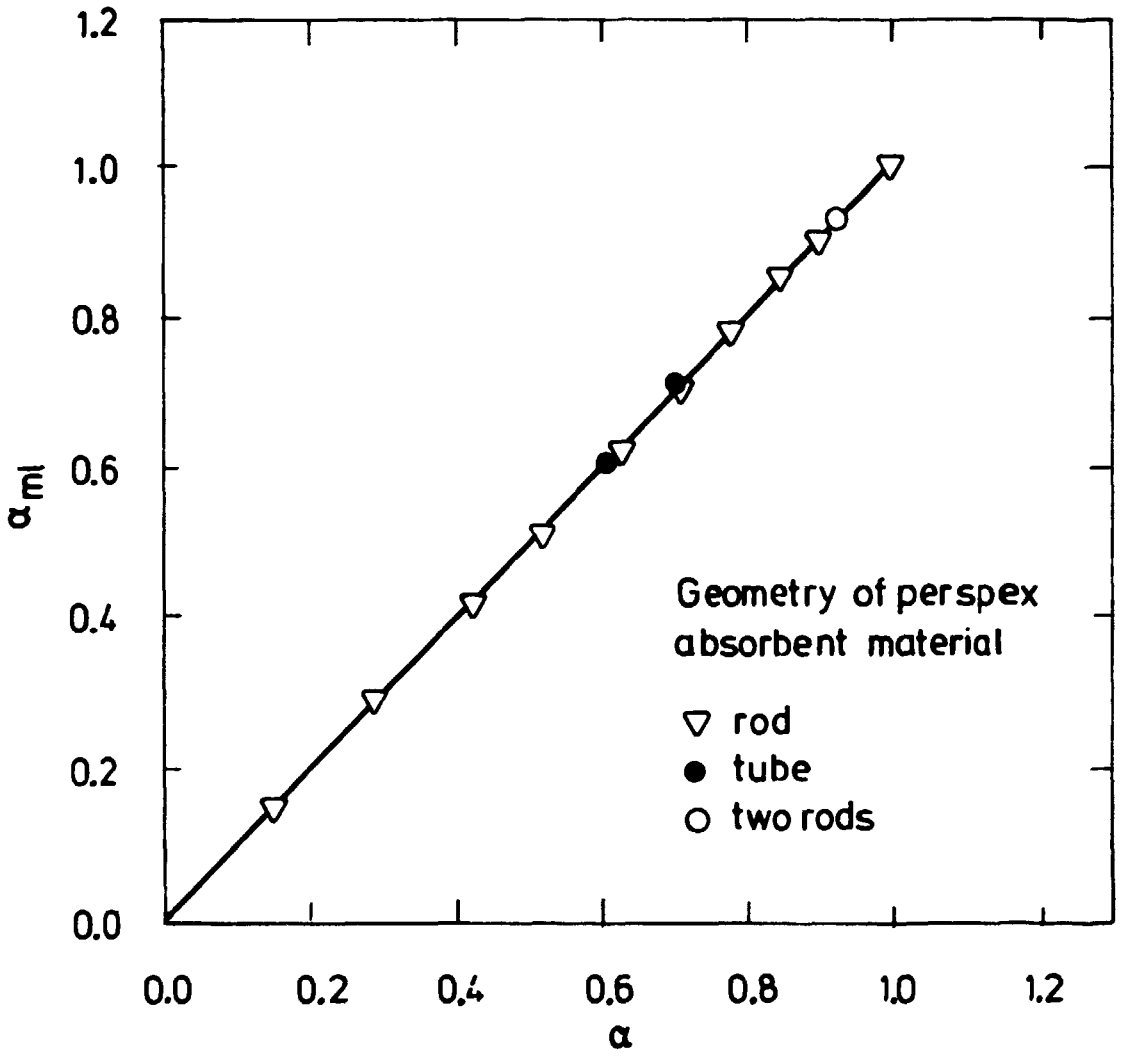

Fig. 3.14. Measured void fraction α_{ml} versus known void fraction α. Glass test section and Am-241 used as γ-source.

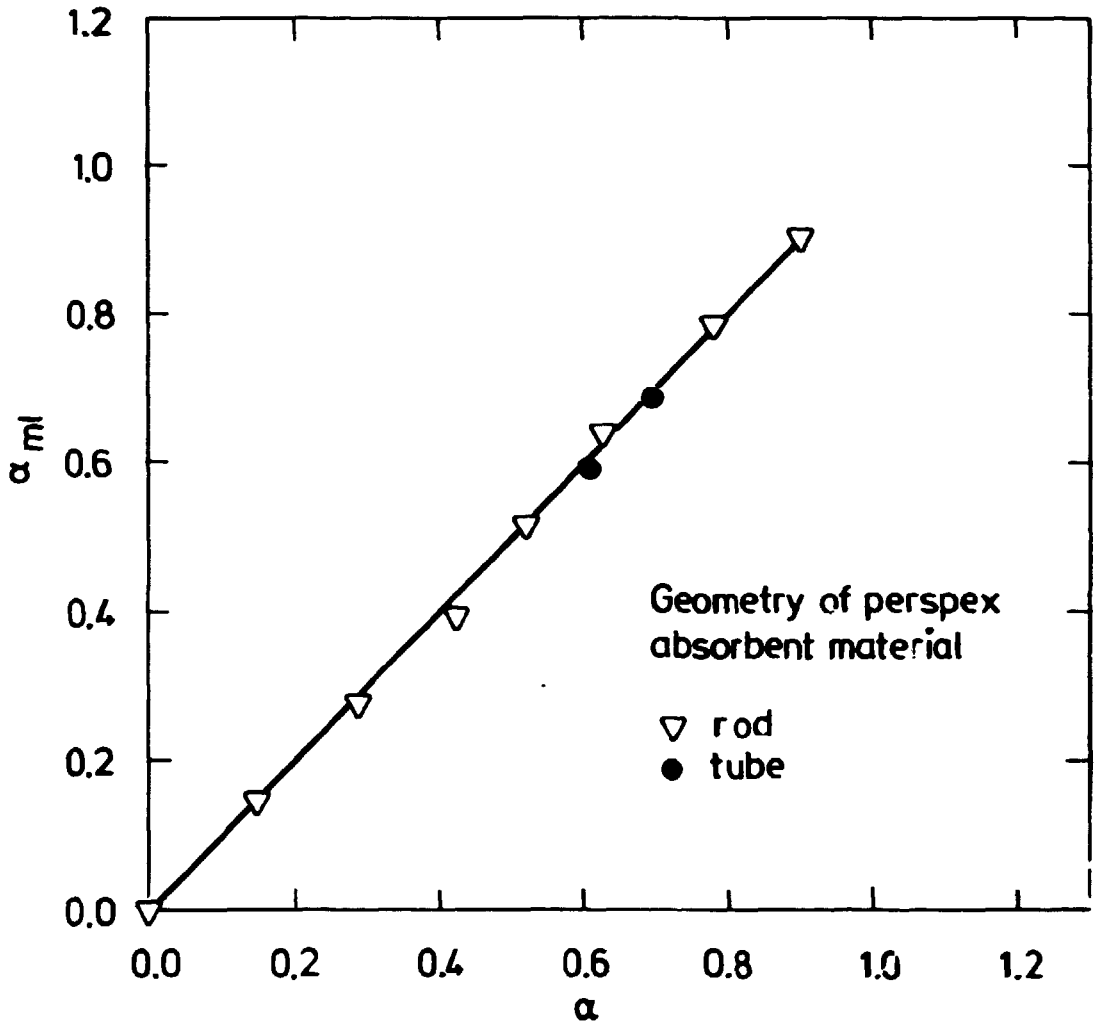

Fig. 3.15. Measured void fraction α_{ml} versus the known void fraction α. Steel test section and Cs-137 used as γ-source.

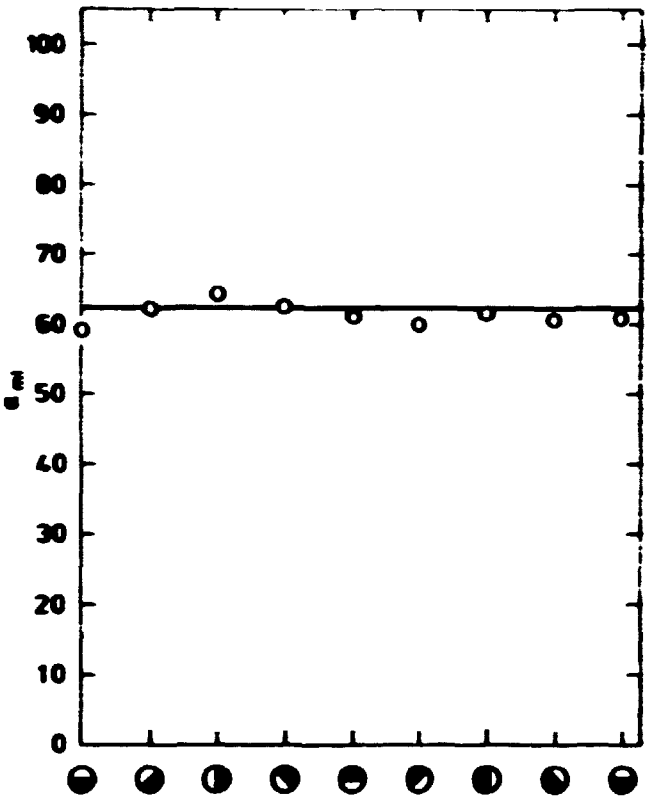

Fig. 3.16. Measured void fraction α_{ml} versus different orientations of a half-moon-shaped absorber rod. The direction of the beam of γ-rays is from the bottom to the top of this paper.

3.2. Experimental facilities

This section describes the experimental facility installed in the Section of Experimental Heat Transfer (SEHT).

Two different test sections have been constructed. The first consists of a glass tube heated by a flow of water. This test section is used for an investigation of a stationary flow of inverse annular film and dispersed droplet flow using liquid nitrogen as coolant.

The second test section consists of an electrically heated steel tube, made for studying the inside reflood of a hot tube by water.

3.2.1. Test section using liquid nitrogen as coolant

In order to become acquainted with the nature of the flow regimes consisting of inverse annular film boiling and the change to dispersed droplet flow, a test section has been constructed, where a visually observable flow can be established.

The test section consists of a glass tube heated by an annular flow of water. As the flow has to be diabatic, and as the wall temperature must be above the minimum film boiling temperature, it is natural to seek a coolant medium among the cryogenic liquids. Further, it is important to use a liquid with a low boiling point in order to be able to neglect wall heat transfer by radiation. If this transfer is negligible, the measured total heat transfer is then equal to the convective heat transfer.

Liquid nitrogen is selected as coolant because it has a low boiling point, - 196°C, and small heat of vapourization, 198 kJ/kg at 1 bar. The Leidenfrost temperature is on the order of -160°C.

The low heat of vapourization limits the need to add heat to the test section. This fact is very important as the flow is heated through the wall of a glass tube, and glass is a poor heat conductor.

The condition for negligible heat transfer by radiation is fulfilled for inner wall temperatures up to 20°C.

If the wall temperature is 20°C and the liquid temperature -196°C, the maximum heat flux by radiation becomes:

$$\max Q''_{rad} \simeq 5.775 \times 10^{-8} \ (T_w^4 - T_{sat}^4) \simeq 400[W/m^2] = 0.04[W/cm^2]$$

and a typical total heat flux is near 2.0 [W/cm^2]. Further advantages are that liquid nitrogen is relatively low priced, easily obtainable, and environmentally harmless. Physical properties of liquid and gaseous nitrogen are compared with water-steam data in Table 3.4.

Table 3.4. Physical properties of nitrogen gas and liquid compared to water-steam data.

		Nitrogen N_2	Water H_2O
p	bar	1	1
T_{sat}	^oC	-196	100
ρ_ℓ	kg/m^3	807	958
ρ_g	kg/m^3	4.61	0.598
ν_ℓ	m^2/s	1.94×10^{-7}	2.91×10^{-7}
ν_g	m^2/s	1.15×10^{-6}	2.01×10^{-5}
k_ℓ	W/m^oC	0.137	0.682
k_g	W/m^oC	7.38×10^{-3}	24.8×10^{-3}
$h_{\ell g}$	J/kg	1.98×10^5	22.6×10^5
c_{pg}	J/kg^oC	1160	2028
$c_{p\ell}$	J/kg^oC	1955	4216
σ	N/m	8.85×10^{-3}	58.8×10^{-3}

The test section, which consists of a glass tube heated by an annular flow of water, is shown in Fig. 3.17.

The water flow keeps the inner wall of the flow channel at a temperature above that of minimum film boiling. This makes it possible to simulate the phenomena just above the quench front during Emergency Core Cooling (ECC) after a LOCA.

During ECC the quench front travels upwards, mainly due to heat conduction in the walls of the hot fuel cladding. As the quench front is not stationary, it is very difficult to measure the void fraction and heat transfer in the post dry-out region.

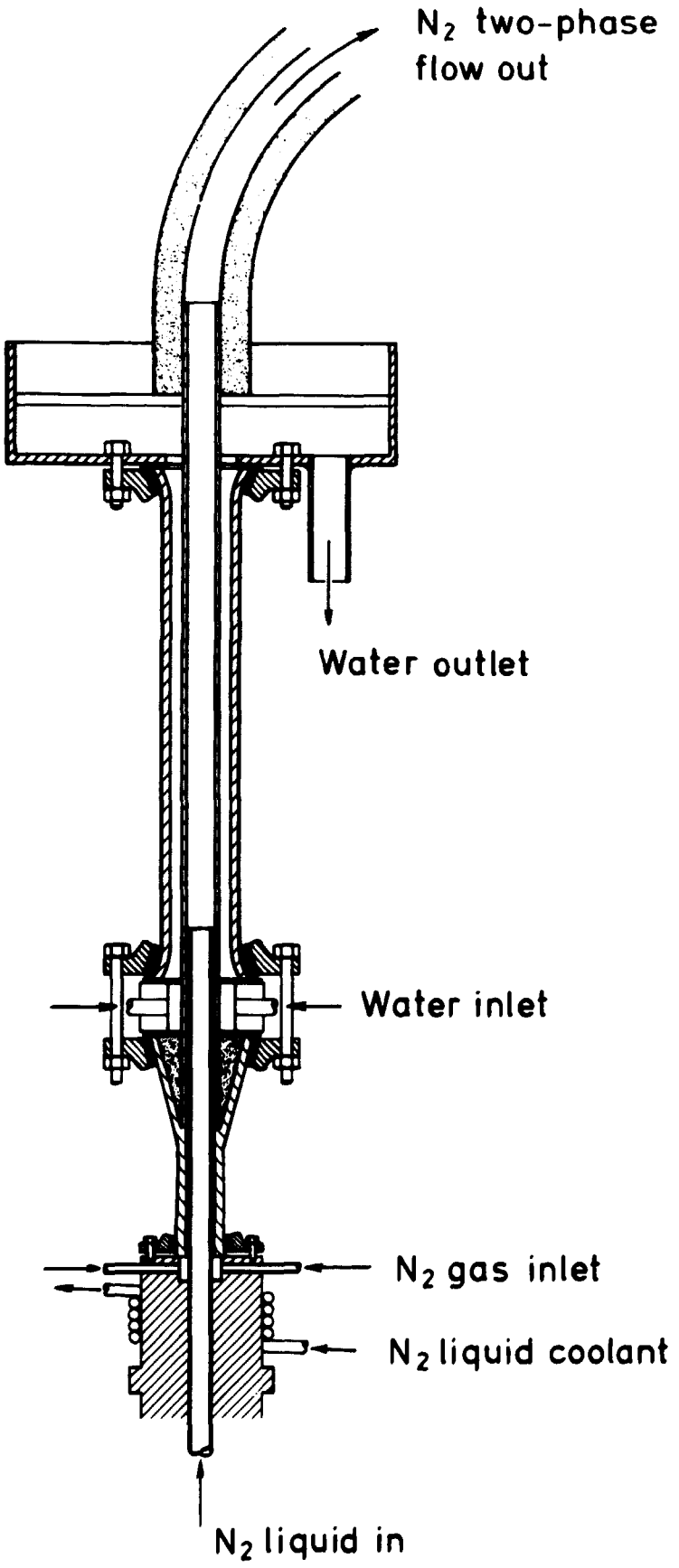

Fig. 3.17. Test section using liquid nitrogen as coolant.

This experimental facility, however, is designed in a way such that the flow regimes above quench front level is in a stationary state.

As it appears in Fig. 3.17, the temperature gradient in the wall at the simulated quench front level is avoided. This is accomplished by supplying the inlet flow of liquid nitrogen through a perspex tube, which is isolated from the glass tube by a thin annular gap.

The inlet flow of liquid nitrogen is supplied from a Dewar flask just below the inlet region of the test section. The inlet region is cooled by a system using liquid nitrogen as coolant. This system suppresses boiling in the flow before the inlet.

If the Dewar flask is depressurized two to three hours before the measuring takes place, it is possible to conduct experiments with subcooled liquid nitrogen. In this case the flow into the test section is established by pressing helium into the Dewar flask. Nitrogen gas condenses at the surface of subcooled liquid nitrogen, and therefore it cannot be used to establish the inlet flow.

The flow of heating water is supplied from a reservoir placed at a level much higher than the test section. This keeps the water free of bubbles, which is necessary to measure the void fraction in the two-phase flow of nitrogen.

The water level in the reservoir is kept very constant in order to have a steady water flow rate through the heating annulus.

Fig. 3.18 shows how the test section is instrumented. The void fraction is determined by γ-ray absorption at two different levels measured from the inlet.

The inlet and outlet flow of liquid nitrogen $\dot{m}_{LN2in}$ and $\dot{m}_{LN2out}$ is measured by tension weigh cells as explained in Section 3.1.1.

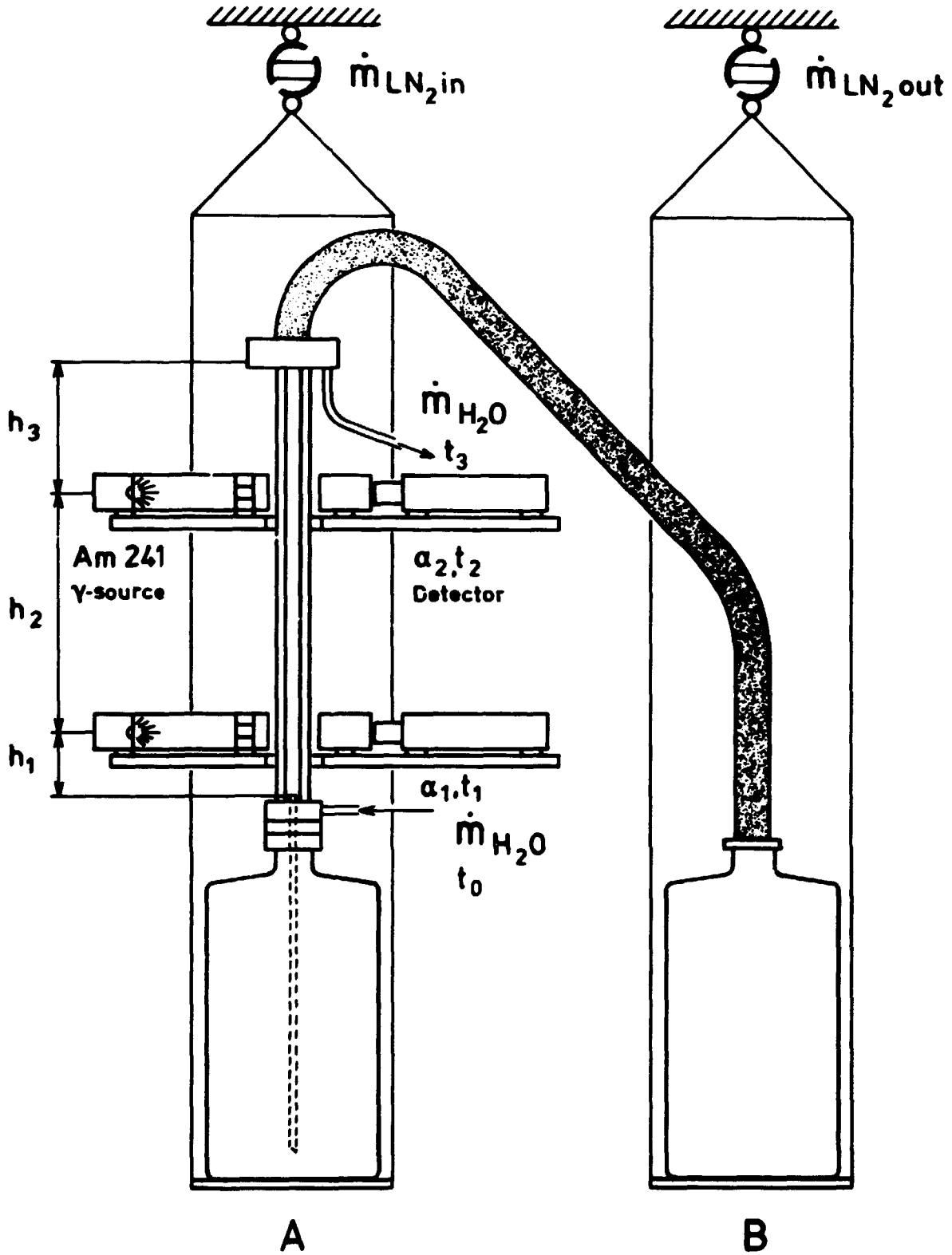

Fig. 3.18. Nitrogen test section with instruments for measuring void fraction and flow rate.

The heat added by the water flow is calculated on the basis of measurements of water flow rate $\dot{m}_{H2O}$, and the inlet and outlet temperature of the water.

In order to measure the heat transfer separately in the parts of the test section where the flow regime consists of inverse annular flow and where there is dispersed droplet flow, the heating water stream has been divided into two loops.

Table 3.5. Geometry of Nitrogen Test Section.

	mm
One water loop version:	
Total heated length	740
Two water loops version:	
Lower heated length	250
Upper heated length	475
Total heated length	725
Both versions:	
Diameter of flow channel	13.6
Wall thickness of glass tube	1.25
Hydraulic diameter of heating water annulus	9.7
Inner diameter of annulus	16.1
Outer diameter of annulus	25.8

The temperature of the heating water is kept at room temperature leading to a very small error caused by heat loss to the surroundings.

3.2.2. Steel tube test section using water as coolant

After a LOCA the fuel elements are reflooded by water; in order to study this preliminary work has been carried out. A test section consisting of an electrically heated tube has been constructed for this purpose.

Despite the different methods that have been tried, it has turned out to be impossible to establish a steady-state situation in the region of dry out, as is possible in the glass test section. Because of axial heat conduction in the wall of the heated steel tube and the higher level of wall temperature, an inlet construction of the type used for the nitrogen experiments has turned out to be inoperative. A quench front always starts to move upwards.

The final lay-out of the water reflood test section is as shown in Fig. 3.19. The heating power is supplied by a 40 kW AC rotating transformer power supply, connected to the test section by two silver coated clamps.

If the tube is quenched slowly it is possible to measure the void fraction at two positions as indicated in Fig. 3.19.

At the outlet of the test section steam and water are moved apart by a steam separator. This device is rather efficient, and an equivalent type has been tested by Andersen (1967).

Table 3.6. Geometry of Water Test Section

	mm
Heated length	1200
Diameter of flow channel	14
Wall thickness	1

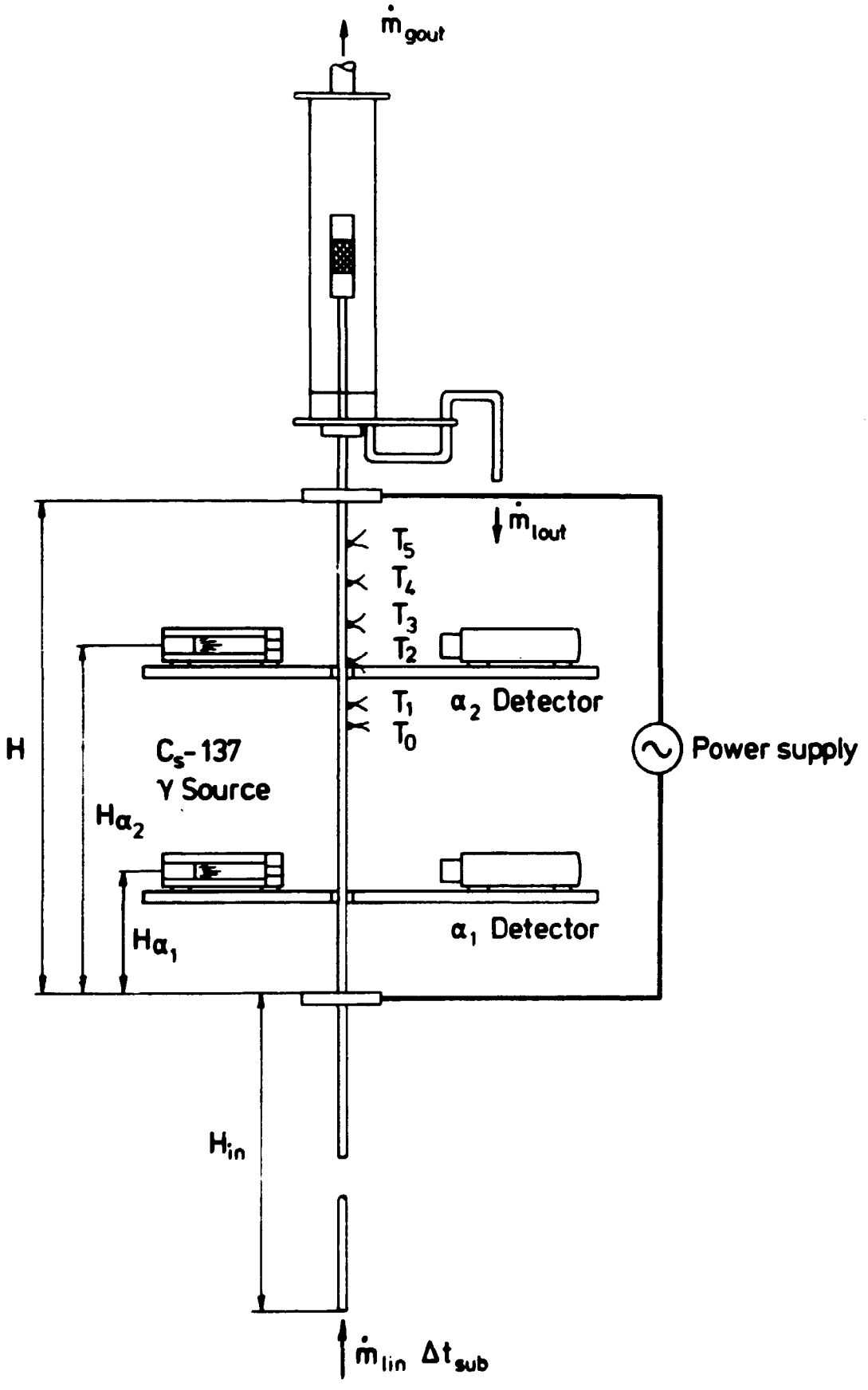

Fig. 3.19. Test section for reflood experiments using water as coolant.

The inlet flow of water is supplied through a flexible tube coming from a container. This container is hung in a weighing cell, which measures the inlet flow rate. The outlet flow of water from the steam separator is collected in another container, and here again the flow is measured by a tension weigh cell.

Thermocouples attached to the wall of the heated part of the test section measure the wall temperatures. In this way, it is possible to measure the position of the quench front. The moment a quench front passes a thermocouple, the wall temperature falls from a high value to one near 100°C.

3.3. Experimental procedures

The nitrogen test section constructed of glass tubing (Figs. 3.17 and 3.18) has been used for several different series of experiments.

The axial void distribution has been measured at varying values of inlet flow rate and inlet subcooling. Simultaneously, the mean heat flux and thermodynamic quality at the inlet and outlet are measured.

In a special series of experiments the heat fluxes to the flow consisting of inverse annular film flow and dispersed droplet flow are measured separately. At last, a series of high-speed flash photos were taken.

The water test section (Fig. 3.19) consisting of a heated steel tube, has been used for a few preliminary flooding experiments, where the void fraction is measured at different positions related to the quench front.

All experimental data are measured by a Solartron Data Acquisiton System controlled by a PDP11/05 computer.

If an experimental result is computed as a compound of more than one measurement, the statistical law of accumulation is used to estimate the deviation of the computed result. In this computation, we take an experimentally estimated standard deviation of the single measured values. During a measuring period, each value is logged about 4-6 times, and this makes it possible for the computer to calculate both the mean and standard deviation.

3.3.1. Void measurements in the nitrogen test section

The measurements of the void fraction at different axial positions are performed by two detector systems. Both detectors are placed at specified positions and the void fractions are found keeping the inlet mass flux and inlet subcooling constant.

Due to the relatively small reservoir of liquid nitrogen (max. 40 kg) the void measurements are conducted as follows: When the two detectors are fixed at given positions above the inlet of the test section, the void fractions are measured after varying the inlet mass flux through a range from 10 to 120 kg/m^2s. This procedure is repeated for the saturated inlet and two different values of inlet subcooling.

After a measurement series of this type the detectors are moved to new positions and the above procedure is repeated.

Before the start of a series of void measurements the two detector channels must be calibrated. The count rates for an empty and filled flow channel are measured in order to be able to calculate the values of the contrast ratios necessary in computating the resulting void fraction.

All the measured data are presented in Appendix D. At each measurement the void fraction α is given as the mean value of 4-6 individual measurements, and the standard deviation s is estimated from the measurement data. A typical standard deviation on α is in the range of 1 to 2% void fraction.

3.3.2. Measurement of heat flux in the nitrogen test section

The heat added to the flow of nitrogen in the flow channel is equal to the heat delivered by the water in the water loop. Heat loss in the surroundings is assumed to be very near zero, because the water in the loop is close to the temperature of the surrounding room.

Then the heat flux is found by measuring the flow rate of water and the temperature drop along the annulus. In case two water loops are present, these quantities are measured for each giving the heat flux in the lower and upper parts of the flow channel.

In order to find the correct mean temperature of the outlet flow, the temperature is measured by a thermocouple in a small mixing cup mounted at the outlet of the test section.

A typical error in the temperature measurements is $\pm$ 0.1°C, and the temperature difference between inlet and outlet is about 5.0°C. This leads to a reasonably good estimate of the heat flux, and it appears from the results presented in Section 3.4 that the scattering of the different measurements is rather small.

In order to estimate the mean inner wall temperature of the flow channel, the following equations are used, when the heating power is known and the flow of water in the annulus is laminar:

The Nusselt Number for laminar flow in an annulus is taken from Knudsen and Katz (1958):

$$Nu = 1.02\ Pr^{0.5} Re^{0.45} \left(\frac{d_2}{d_1}\right)^{0.8} \left(\frac{d_h}{H}\right)^{0.4} Gr^{0.05} \qquad (3.33)$$

where

$d_h = d_2 - d_1$ = hydraulic diameter of the annulus

d_2 = outer diameter of the annulus

d_1 = inner diameter of the annulus

H = heated length

Pr = Prandtl's number

Re = Reynold's number

Gr = Grashof's number

The mean wall temperature T_{wo} along the heated length H at the outside of the flow channel is given by

$$T_{wo} = T_m - \frac{Q\, d_h}{k\, Nu\, A_h}\,, \qquad (3.34)$$

where

T_m = mean temperature of water
Q = power added to the nitrogen flow by the water
k = thermal conductivity of water
$A_h = \pi d_1 H$ = heat transfer area

The mean temperature T_w at the inner side of the flow channel then becomes:

$$T_w = T_{wo} - \frac{Q}{H\, \pi\, 2\, k_{glass}} \ln \frac{d_1}{d_0}\,, \qquad (3.35)$$

where k_{glass} = thermal conductivity of glass,
d_0 = diameter of flow channel

3.4. Experimental results

A summary of the experiments is given in Table 3.7. The type of test section, system parameters, subcooling and wall temperature are given with the actual deviations, and the type of measurements carried out are listed.

In the experiments with run numbers 301-358 heat transfer measurements have been performed for the lower and upper part of the flow channel, where the flow patterns mainly are inverse annular film flow and dispersed droplet flow.

A complete list of the measured data is tabulated in Appendix D.

Table 3.7. Summary of the experiments

System Parameters							Experiments	
Run No.	Test Section	System Press. bar	Mass Flux kg/m^2s	Heated Length m	Inlet Subcooling ^oC	Wall Temperature ^oC	Void Measurements	Heat Transfer Measurements
1- 63	N_2 -glass	1	10-110	0.740	0.2 ± 0.4	-4.5 ± 4.7	x	x
64- 89	N_2 -glass	1	10- 90	0.740	4.2 ± 0.4	-5.7 ± 4.8	x	x
90-131	N_2- glass	1	10- 70	0.740	5.9 ± 0.6	-7.0 ± 3.8	x	x
301-322	N_2- glass	1	12-135	0.250+0.475	-0.4 ± 0.2	-2.1 ± 2.9		x
323-332	N_2- glass	1	11- 60	0.250+0.475	5.0 ± 0.6	-1.3 ± 2.5		x
333-344	N_2- glass	1	10- 70	0.250+0.475	6.5 ± 0.5	-2.4 ± 3.9		x
345-358	N_2- glass	1	9- 75	0.250+0.475	8.9 ± 0.7	-2.1 ± 4.7		x
-	H_2O-steel	1	28.5-30.6	1.200	6,13,and 33	650 ± 50	x	

3.4.1. Axial Void Fraction Distribution

All measurements of the mean void fraction are plotted in Figs. 3.20-3.29. Here the mean void fraction α is plotted versus the mass flux. Each plot gives the result for one axial position of the detector and one to three different values of the inlet subcooling.

Curves estimated by least-squares fits have been plotted through the measured points in order to be able to read the value of the void fraction at mass fluxes, where the void has not been measured.

All the curves in Figs. 3.20-3.29 show a decrease from a relatively high void fraction to a lower one as the mass flux increases.

Measurements at positions near the inlet give relatively small values of the void fraction compared with measurements performed at a higher level. Near the outlet of the test section the measured values of α is close to 100%. Increasing the inlet subcooling causes a decrease in the void fraction, which clearly appears from the results obtained at a short distance from the inlet.

In Figs. 3.30-3.35 the void measurement data are replotted in order to show the axial void fraction distribution for mass fluxes from 10 to 80 kg/m^2s.

At an elevation of about 250 mm the void fraction has increased to a value of 80%-90% corresponding to a change in flow pattern from inverse annular flow to dispersed droplet flow. This interpretation is in agreement with the visual observations (see the photos in Figs. 3.47-3.49). The plots showing the axial void profile at $G = 50$ kg/m^2s and $G = 70$ kg/m^2s have been compared with the computed profiles using the computer code RISQUE-N2. The results of this comparison between experimental data are presented in Section 4.2.8 together with the calculations.

3.4.2. Heat Transfer Measurements

Coincident with measurements of mean void fraction the heat flux is estimated by measuring the heat added to the nitrogen two-phase flow. However, the heat flux found in this way is the mean flux for the total heated length of the flow channel.

In Figs. 3.36-3.38 the measured heat flux q" is plotted versus the mass flux G. The first of these figures shows the result for saturated inlet and the two other the results for increasing values of the inlet subcooling.

The heat flux measurements presented in the Figs. 3.36-3.38 are mean values for both inverse annular flow and dispersed droplet flow. The heat flux increases when the mass flux is increased. The dependence on the inlet subcooling is very small and not as significant as in the case of the void fraction, which has a clearly dependence of the inlet subcooling.

The measured values of inlet and outlet thermodynamic quality x are plotted versus the mass flux G in Figs. 3.39, 3.40, and 3.41. As is showing in the figures, the outlet quality is rather sensitive to an increase of the mass flux; the flow is a typical low quality flow, at higher flow rates. At very small mass fluxes $G \leq 10$ kg/m^{2}s, where the measured thermodynamic quality is greater than 100%, it is still possible to observe droplets in the flow. This observation shows that the flow is not in thermodynamic equilibrium, and the gas phase is superheated.

In order to become acquainted with the axial distribution of the heat flux, measurements of mean heat flux have been performed in two parts of the flow channel consisting of the inverse annular region, 0-250 mm, and the dispersed droplet flow region, 250-725 mm.

The results are plotted versus the mass flux in Fig. 3.42. The heat flux to the inverse film flow depends only slightly on the mass flux. An explanation of this could be that the relatively small velocity of both the gas and liquid phases

does not cause any significant heat transfer by forced convection.

The heat transfer to the dispersed droplet flow is more strongly mass flux dependent. There is a physical cause for this, as in this high void region the velocities of the gas phase increase very fast.

Table 2.1 in Section 2.3.3 gives a summary of different inverse annular film boiling heat transfer correlations. In the following H_1, H_2, H_3 and H_4 symbolize the four tabulated coefficients of heat transfer.

In the Figs. 3.43-3.46 the measured coefficients of heat transfer H_m are compared with each of the coefficients given by H_1, H_2, H_3, and H_4. In the computation of H_3 the void fraction α is equal to zero and the effect of subcooling F_{sub} is chosen to be unity. The constant c_1 in the expression for H_4 is 0.33. All physical properties of nitrogen are at saturation temperature and at 1 bar.

The correlation H_2 proposed by Berenson (1961) gives the best fit to the measured data. The three correlations H_2, H_3, and H_4 are all in fairly good agreement with the measured data obtained for mass fluxes from 10 to 100 kg/m^{2}s. The correlation H_3 proposed by Rathmann and Kortakorpi (1979) predicts the measured data very well, but as can be seen the value of α must be equal to zero. If α is increased then the approach to the measured values becomes too small. For $\alpha = 0$ and $F_{sub} = 1$ the correlations H_2 and H_3 are nearly equal. The correlation H_1 proposed by Bromley gives a value, that is too small.

3.4.3. Photos of Inverse Annular and Dispersed Flow

The nitrogen test section made of glass tubing is very suitable for visual observation of the flow patterns.

A series of high-speed flash photos has been taken using a Strobotac flash unit and a 6 x 6 camera equipped with special optics.

Some of the results are shown in the Figs. 3.47, 3.48, and 3.49. The flow channel is in the middle of each photo and the axial position is indicated on the ruler at the left. The scale is very nearly 1:1.

Near the inlet the flow pattern consists of a dense liquid core surrounded by a stable film of gas near the wall of the heated tube. This liquid core becomes more distinct when the flow rate or the inlet subcooling is increased. The surface of the liquid core has a wavy configuration, sometimes disturbed by a large wave or bubble. This disturbance occurs more frequently near the change to dispersed droplet flow.

The photo in the middle shows the change from inverse annular flow to dispersed droplet flow. Some of the droplets have a rather large diameter even at a high axial elevation. However there are also many small droplets, which are seen only with difficulty in the photos. The shapes of the droplets are very irregular and some droplets are breaking into two or some are colliding.

The visual observations give reason to conclude that inverse annular film boiling is a pattern that can occur in a tube with wall temperature above the minimum film boiling temperature. At void fractions above 80% at atmospheric pressure the inverse annular flow changes to dispersed droplet flow.

3.5. Results Obtained during Reflood with Water

The reflood experiments performed in the steel test section consist of measurements of the void fraction at different axial positions relative to the position of the quench front.

As shown in Fig. 3.19 two void detectors are placed at two elevations, $H_{\alpha 1}$ = 300 mm and $H_{\alpha 2}$ = 840 mm, measured from the bottom of the heated part of the flow channel. The total heated length is H = 1200 mm. The position of the quench front during the measurement of the void fraction is indicated

by thermocouples T_0, T_1, T_2, T_3, T_4, and T_5 mounted at known axial positions. One measurement of the void fraction takes 80 seconds.

If the quench front velocity is sufficiently small, the quench front travels a distance corresponding to the interval between two thermocouples during the void measuring period. The accuracy in the estimate of the distance between the quench front and the position of a void detector, H_{qf} is given by the counting time, distances between the thermocouples, and the velocity of the quench front. In the present measurements the error on H_{qf} is on the order of 100 mm.

In Fig. 3.50 the void fraction α is plotted versus the elevation above the quench front, H_{qf}. Before the reflooding is started the wall temperature is about 650°C.

The measurements of void obtained for elevations above the quench front, $H_{qf} \geq 0$, are all greater than 80%. In this case the only possible flow pattern is dispersed droplet flow. Below the position of the quench front, $H_{qf} \leq 0$, the void measurements give values in the range of 50% to 80%. Thus the flow regime below the quench front must be annular flow. In other words, there is no inverse annular film flow present due to the high void in the wetted region.

The experimental results described above are only preliminary. In future investigations it could be interesting to study how the flow pattern during the reflood is influenced by the wall temperature in the dry region, heat flux, mass flux, and inlet subcooling. As described in Section 2.1. and as shown in Fig. 2.1., in the flow regimes occuring during the reflooding phase the annular film flow or inverse annular flow can be dominant. The measurement method for such an investigation has been demonstrated. However, the experimental results could undoubtedly be improved by using three void detectors instead of two and a more intense Cs-137 γ-source of actual intensity 1 mC, and smaller distances between the thermocouples.

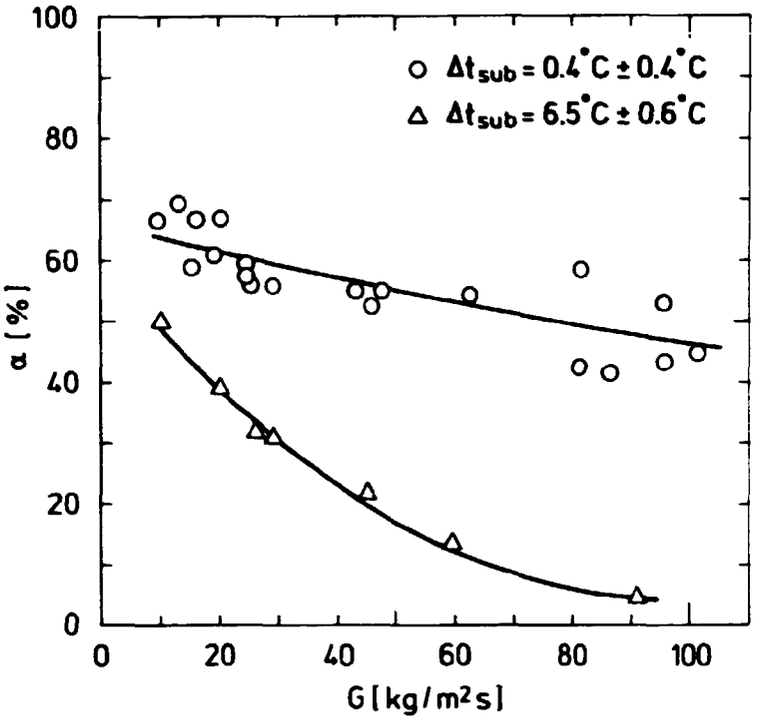

Fig. 3.20. Mean void fraction α versus mass flux G, measured 45 mm above the inlet.

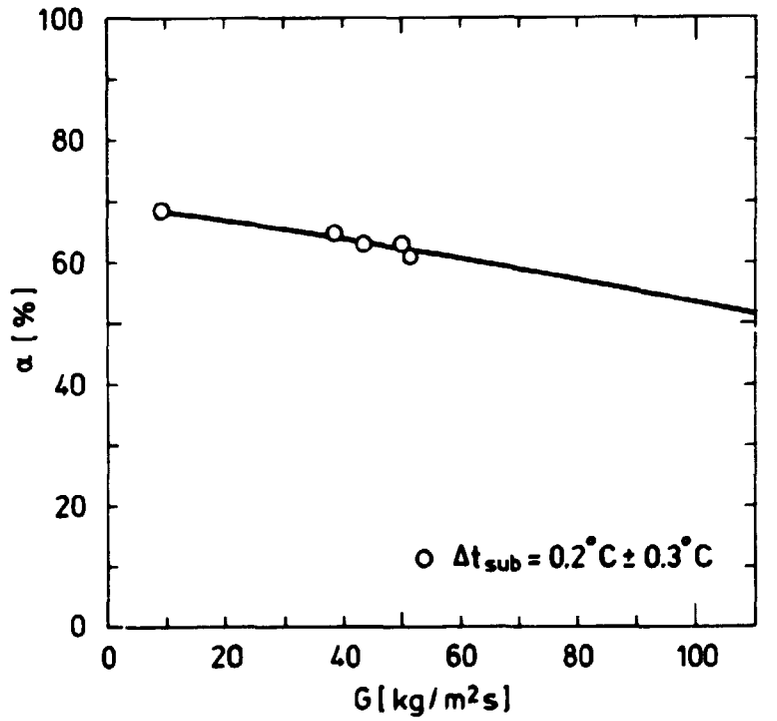

Fig. 3.21. Mean void fraction α versus mass flux G, measured 50 mm above the inlet.

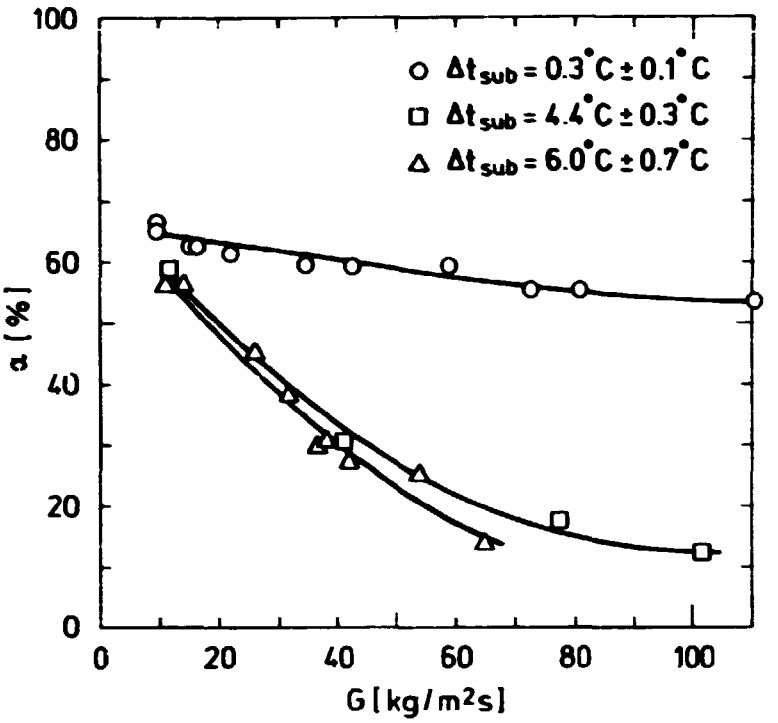

Fig. 3.22. Mean void fraction α versus mass flux G, measured 60 mm above the inlet.

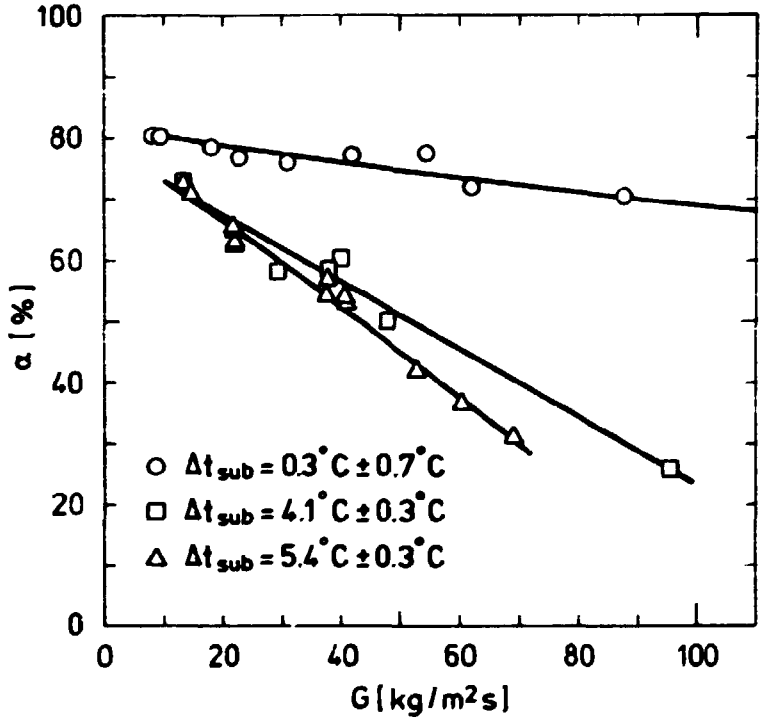

Fig. 3.23. Mean void fraction α versus mass flux G, measured 100 mm above the inlet.

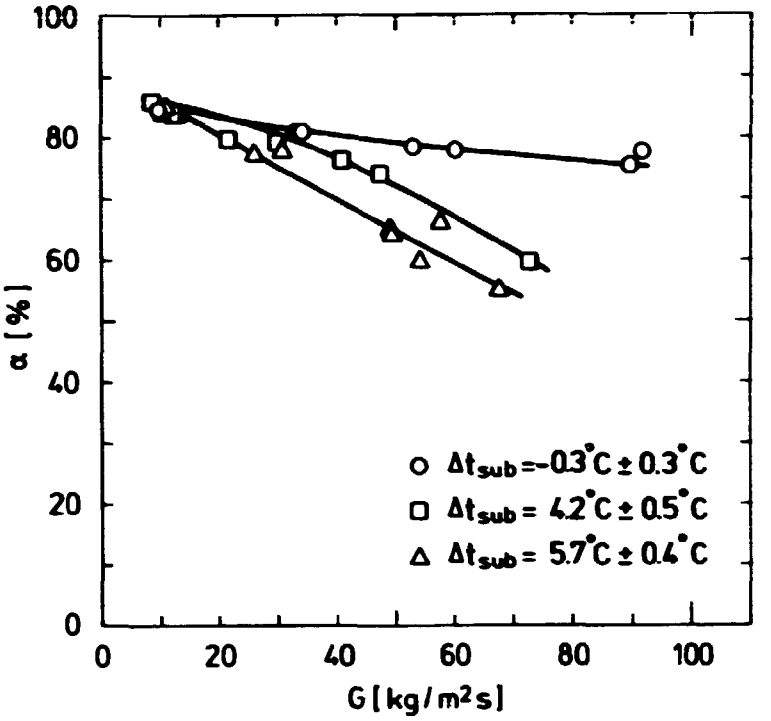

Fig. 3.24. Mean void fraction α versus mass flux G, measured 160 mm above the inlet.

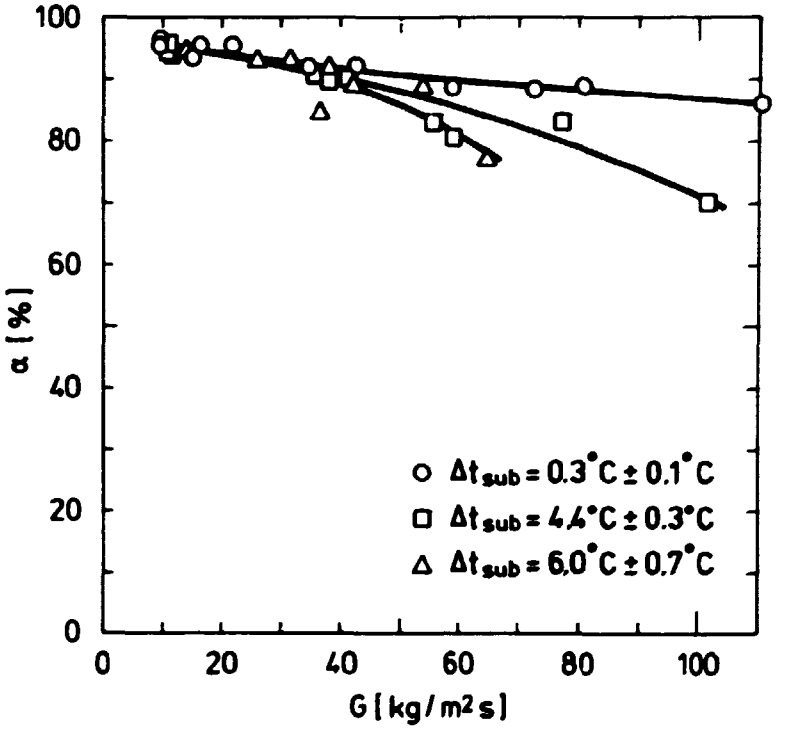

Fig. 3.25. Mean void fraction α versus mass flux G, measured 230 mm above the inlet.

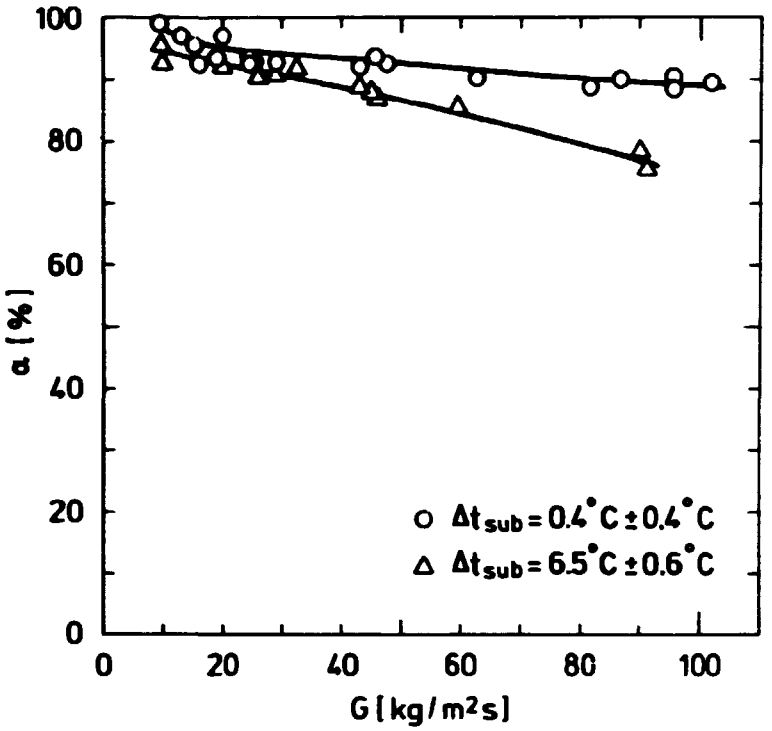

Fig. 3.26. Mean void fraction α versus mass flux G, measured 310 mm above the inlet.

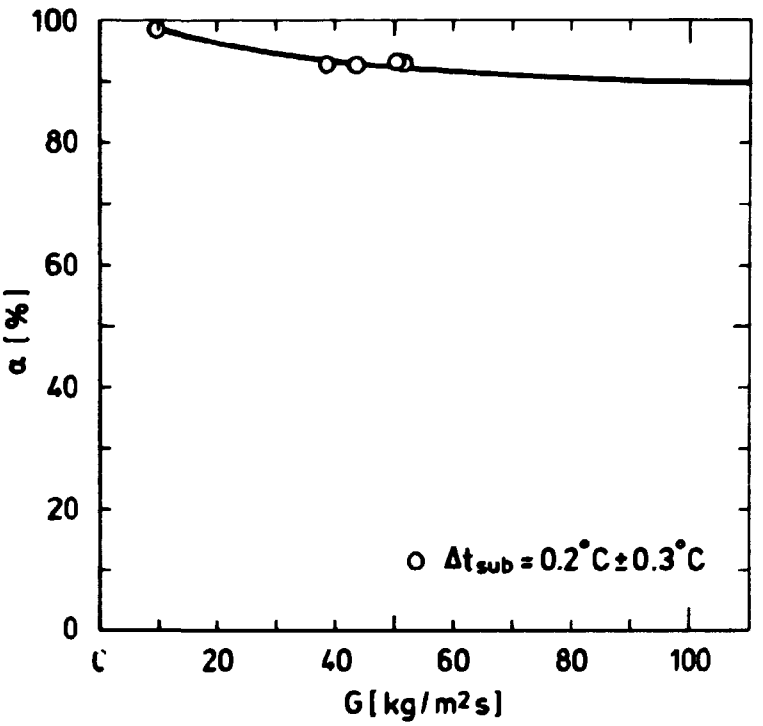

Fig. 3.27. Mean void fraction α versus mass flux G, measured 315 mm above the inlet.

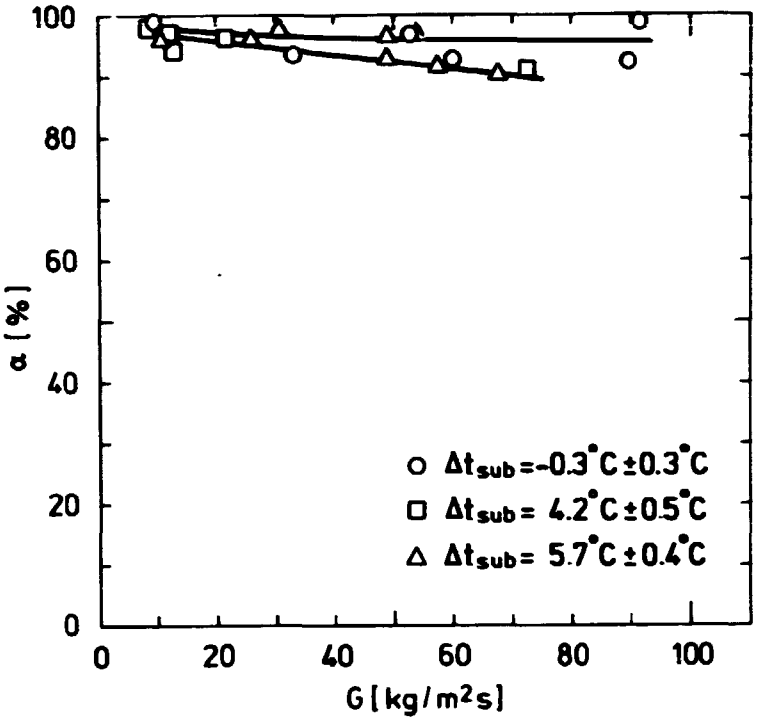

Fig. 3.28. Mean void fraction α versus mass flux G, measured 470 mm above the inlet.

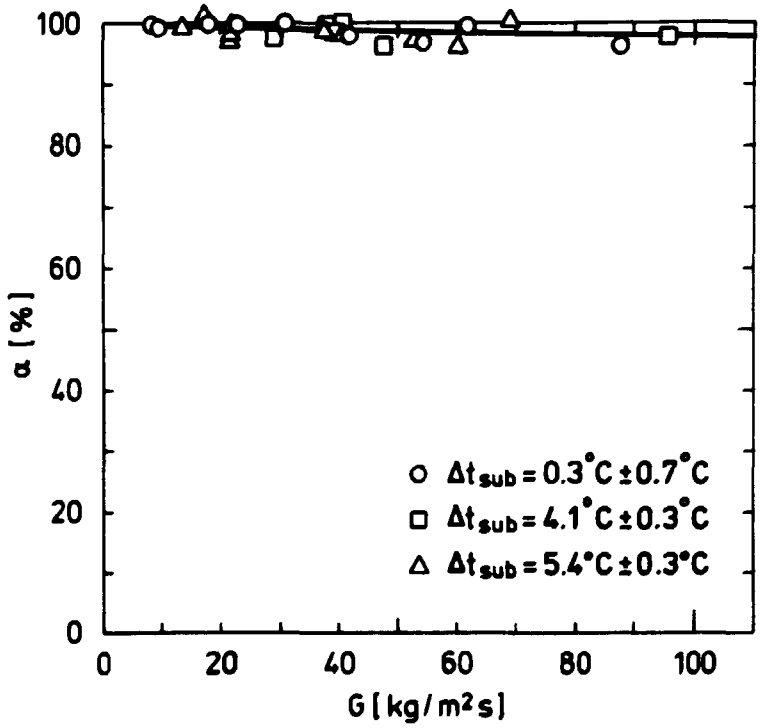

Fig. 3.29. Mean void fraction α versus mass flux G, measured 600 mm above the inlet.

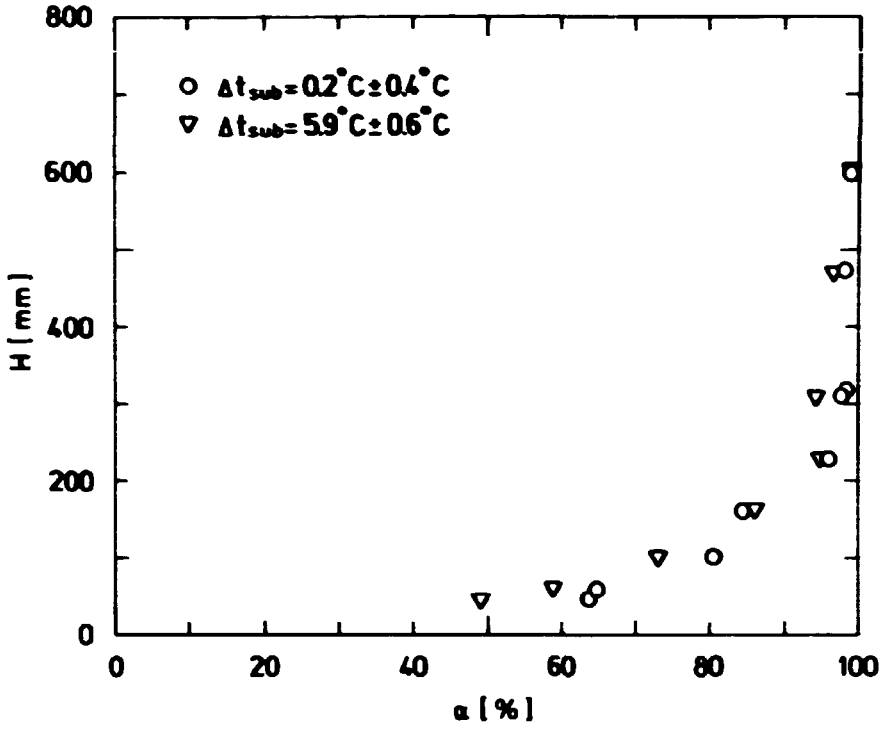

Fig. 3.30. Axial void profile. G = 10 kg/m^{2}s.

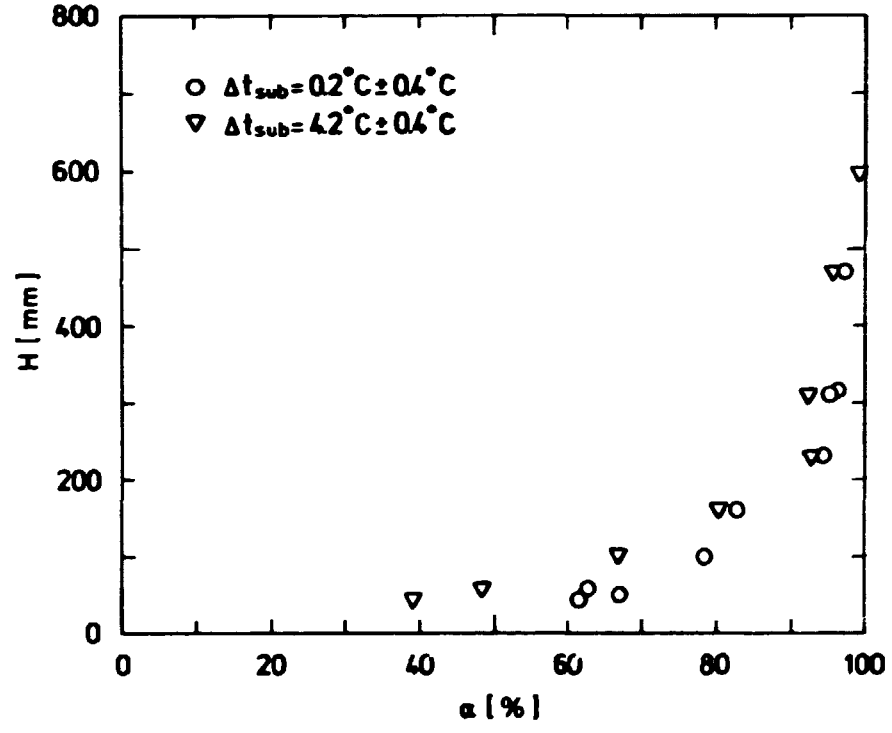

Fig. 3.31. Axial void profile. G = 20 kg/m^{2}s.

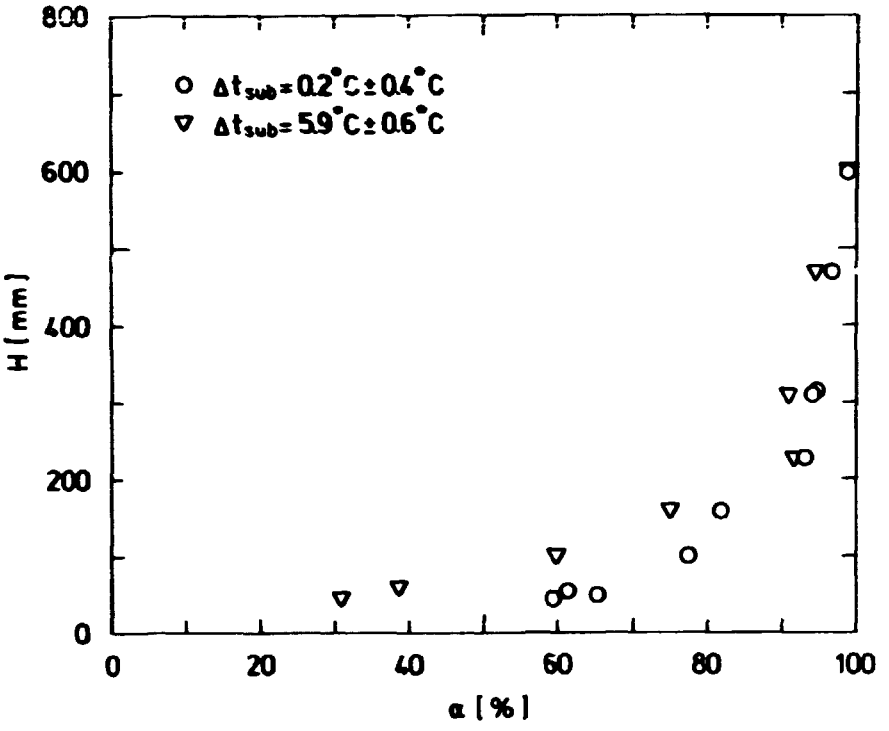

Fig. 3.32. Axial void profile. G = 30 kg/m^{2}s.

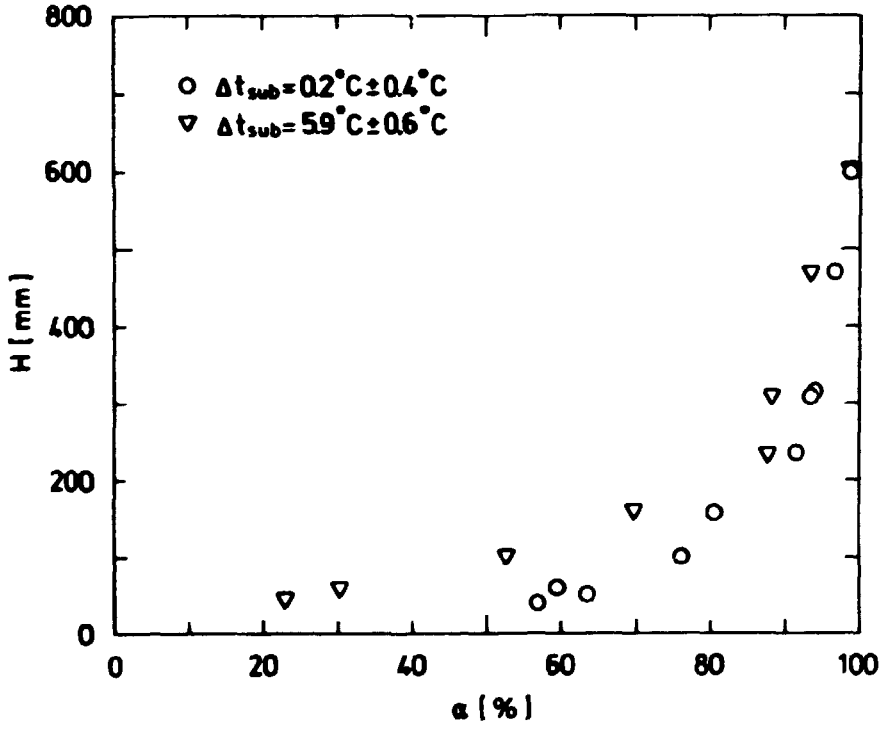

Fig. 3.33. Axial void profile. G = 40 kg/m^{2}s.

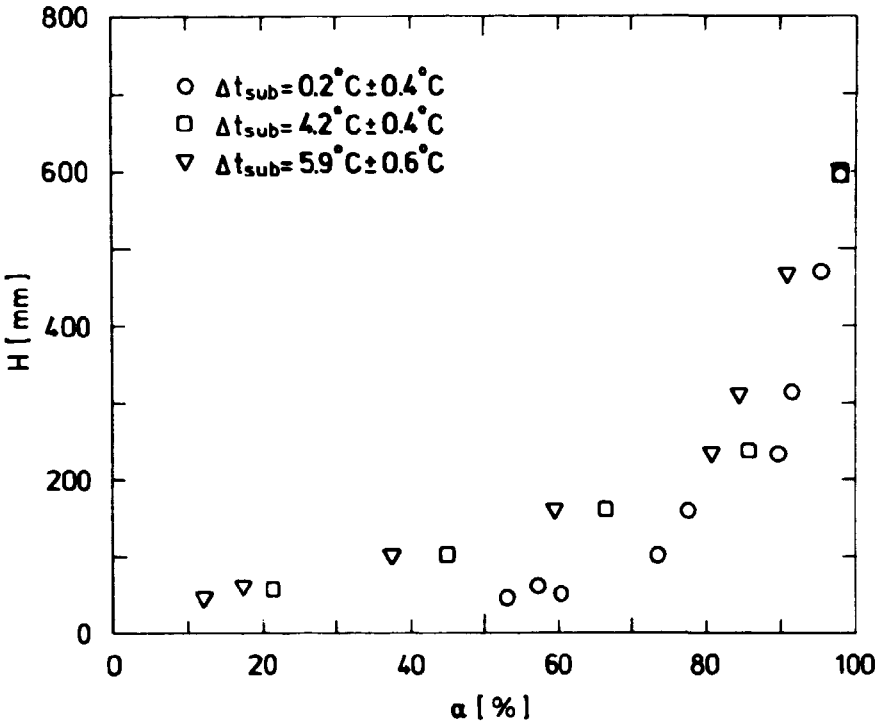

Fig. 3.34. Axial void profile. G = 60 kg/m^{2}s.

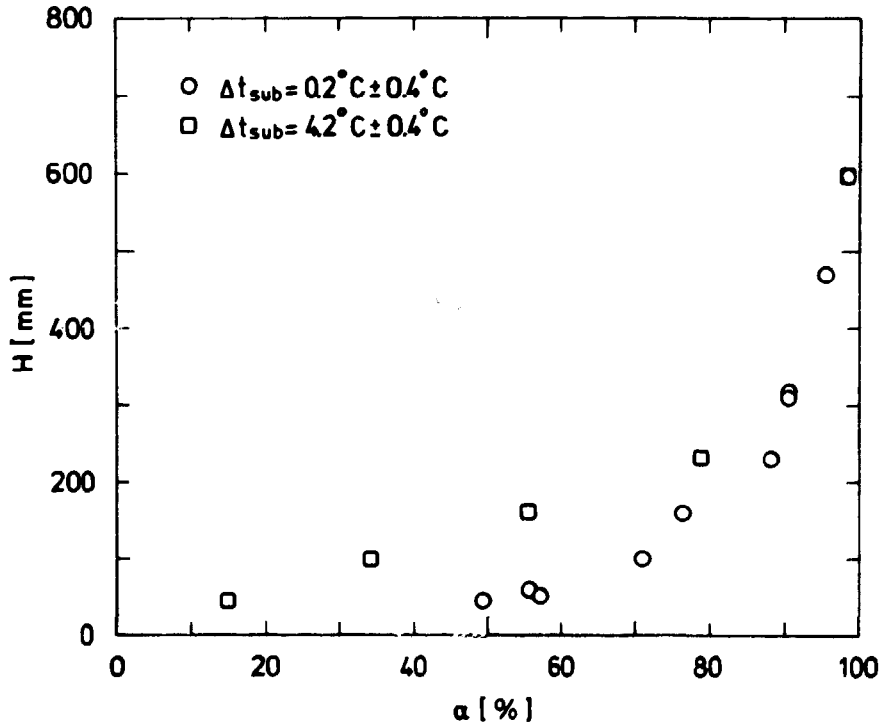

Fig. 3.35. Axial void profile. G = 80 kg/m^{2}s.

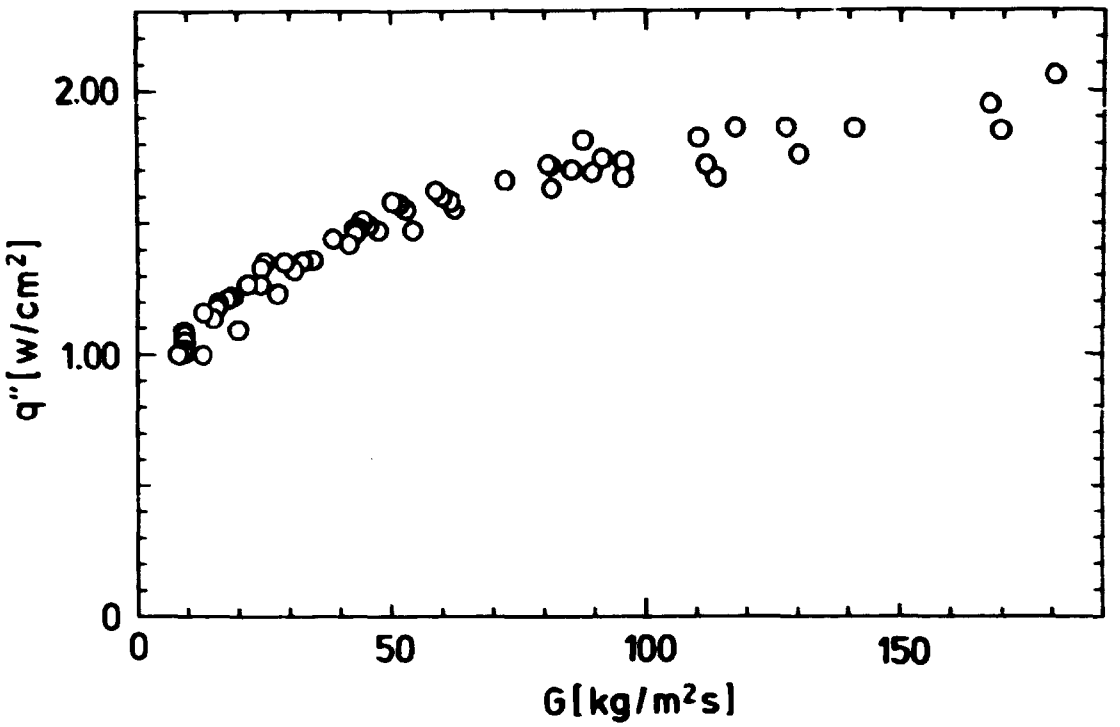

Fig. 3.36. Measured mean heat flux q" versus mass flux G. q" is measured as an average for the total length H = 740 mm of the test section. Subcooling of the inlet flow is $\Delta\bar{t}_{sub} = 0.2^{o}C \pm 0.4^{o}C$ corresponding to saturated inlet. The wall temperature is $\bar{t}_{w} = -5^{o}C$.

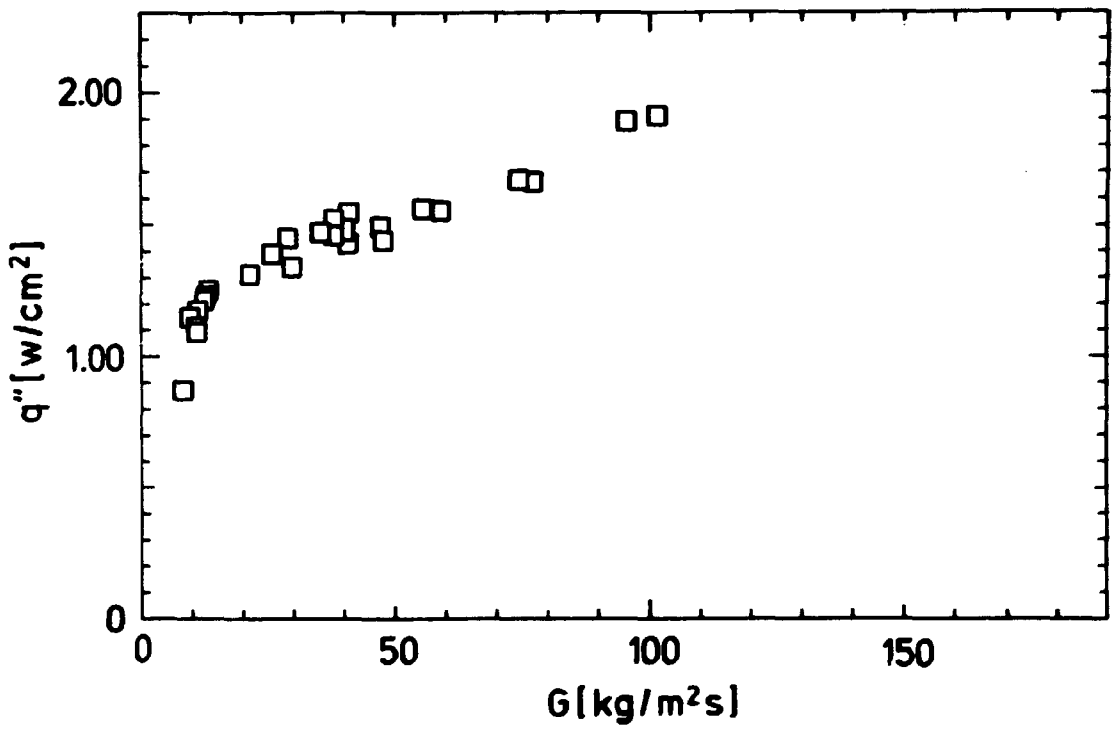

Fig. 3.37. Measured mean heat flux q" versus mass flux G. q" is measured as an average for the total length H = 740 mm of the test section. Subcooling of the inlet flow is $\Delta\bar{t}_{sub} = 4.2^{o}C \pm 0.4^{o}C$. The wall temperature is $\bar{t}_{w} = -6^{o}C$.

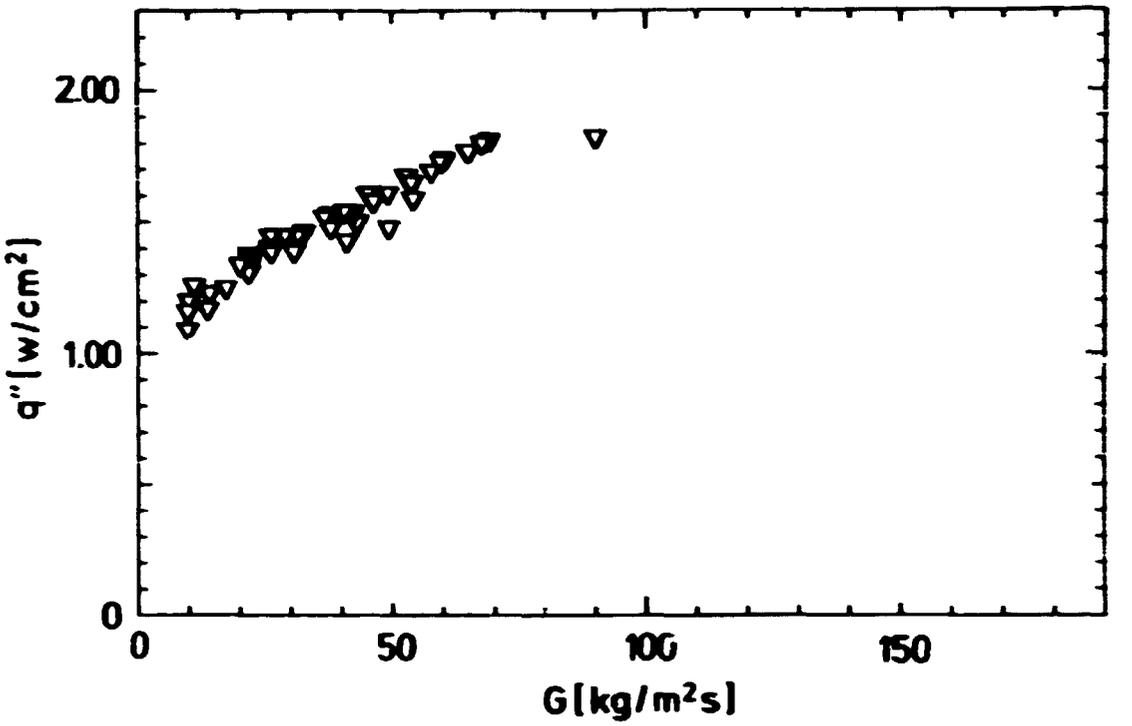

Fig. 3.38. Measured mean heat flux q" versus mass flux G. q" is measured as an average for the total length H = 740 mm of the test section. Subcooling of the inlet flow is $\Delta\bar{t}_{sub} = 5.9^{o}C \pm 0.6^{o}C$. The wall temperature is $\bar{t}_{w} \simeq -7.0^{o}C$.

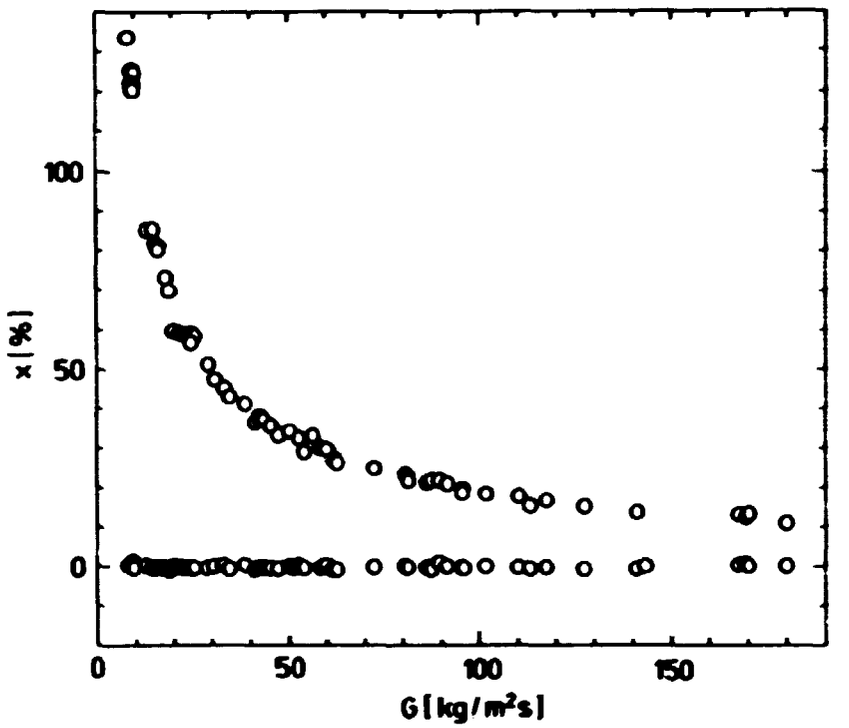

Fig. 3.39. Measured inlet and outlet thermodynamic quality X versus mass flux G. The heated length is H = 740 mm and the subcooling of the inlet flow is $0.2\ ^{o}C \pm 0.4\ ^{o}C$ corresponding to saturated inlet and X = 0.0% at the inlet.

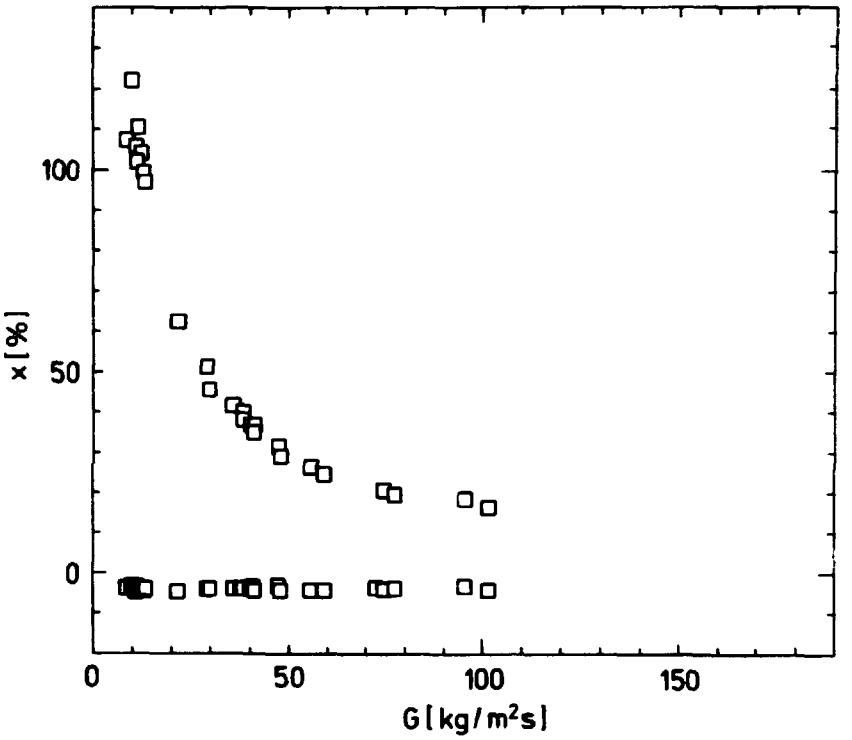

Fig. 3.40. Measured inlet and outlet thermodynamic quality X versus mass flux G. The heated length is H = 740 mm and the subcooling of the inlet flow is 4.2 °C ± 0.4 °C.

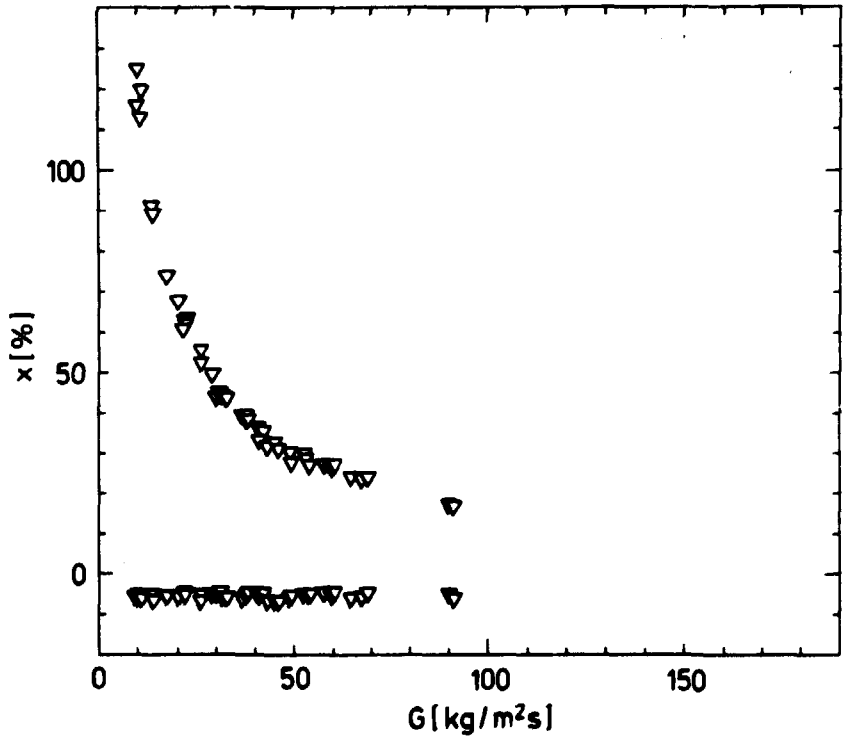

Fig. 3.41. Measured inlet and outlet thermodynamic quality X versus mass flux G. The heated length is H = 740 mm and the subcooling of the inlet flow is 5.9 °C ± 0.6 °C.

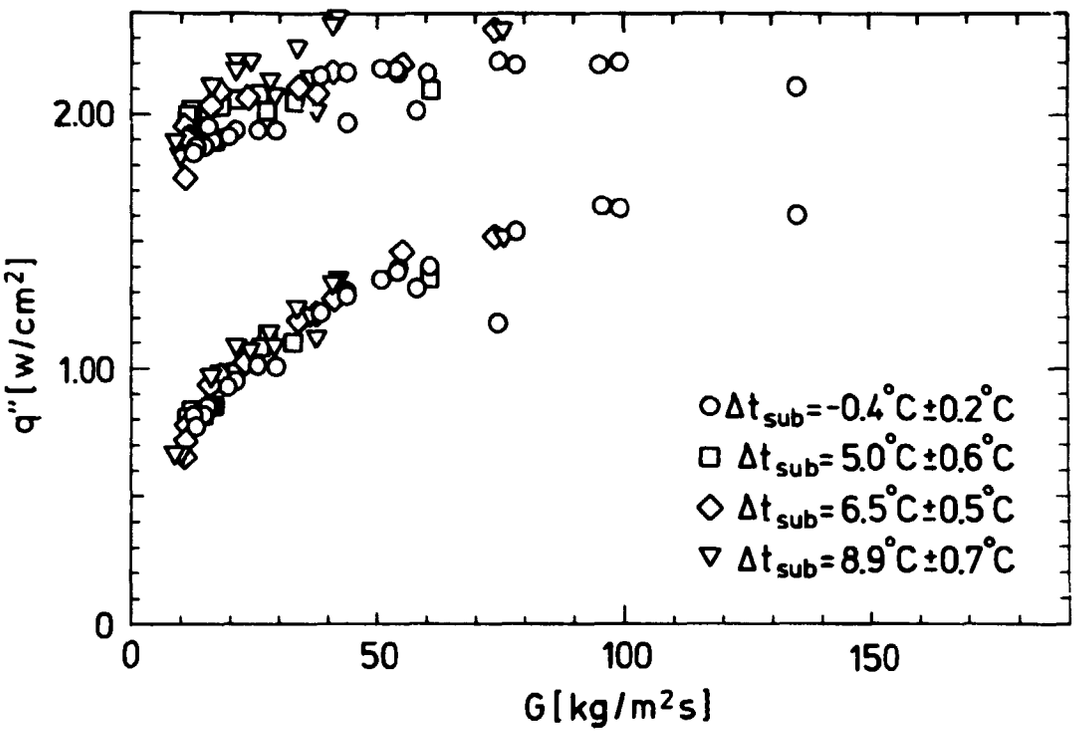

Fig. 3.42. Measured heat flux q" versus mass flux G. The results near 2 W/cm^2 are measured in the lower part of the test section, 0-250 mm, where the flow pattern is mainly inverse annular flow. The results, which vary from 0.65-1.65 W/cm^2, are measured in the upper part of the test section, 250-725 mm, where the dominant flow regime is dispersed droplet flow. Mean wall temperature in the lower part of the flow channel is $\bar{t}_{w\ 0-250} \approx -12^{o}C$ and in the upper part $\bar{t}_{w\ 250-725} \approx 3^{o}C$.

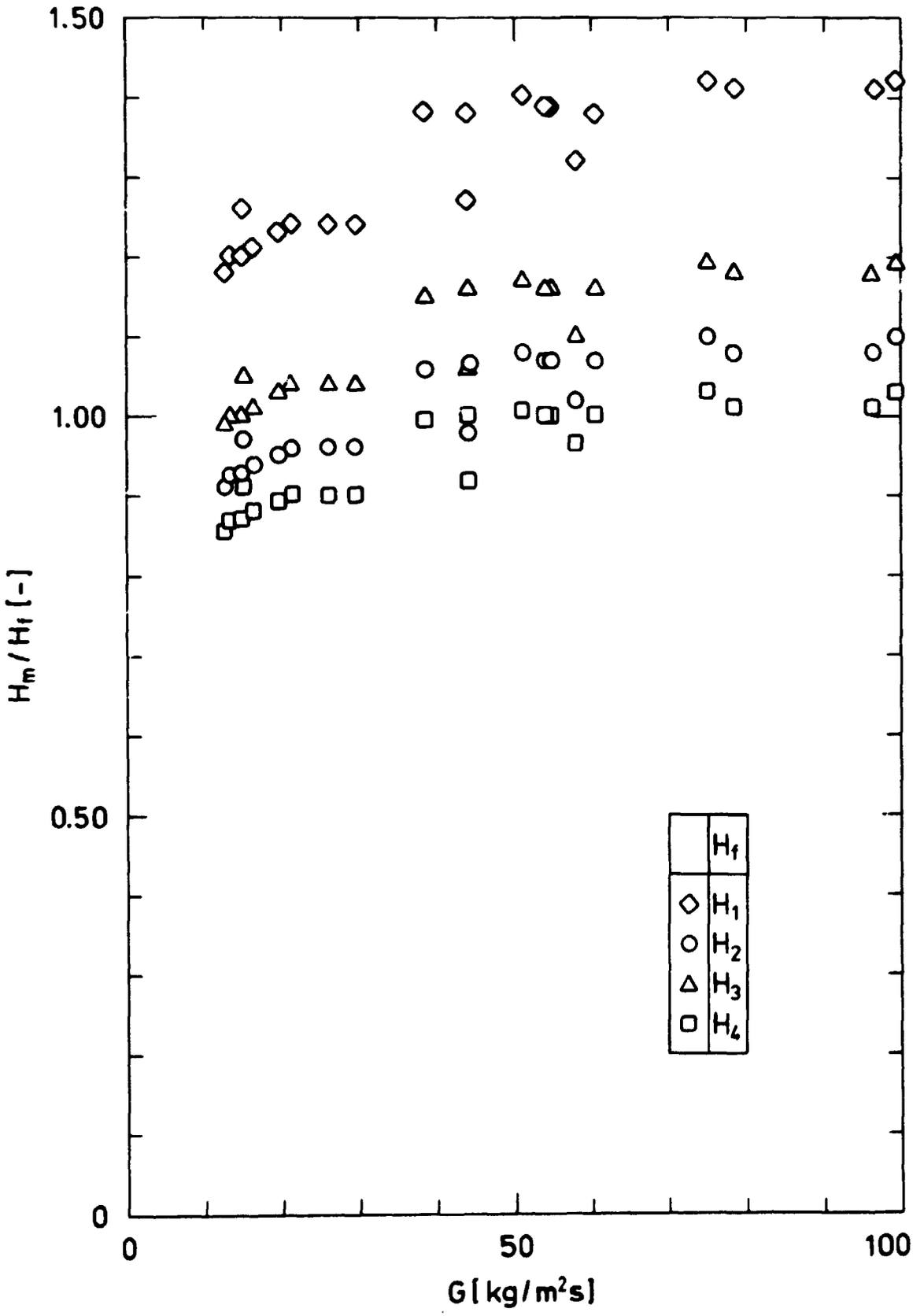

Fig. 3.43. The ratio H_m/H_f versus mass flux G. H_m is the measured coefficient of heat transfer. H_f is a calculated value using different correlations for inverse annular film flow. $\bar{t}_w \simeq -12^oC$. $\Delta\bar{t}_{sub} = -0.4^oC \pm 0.2^oC$.

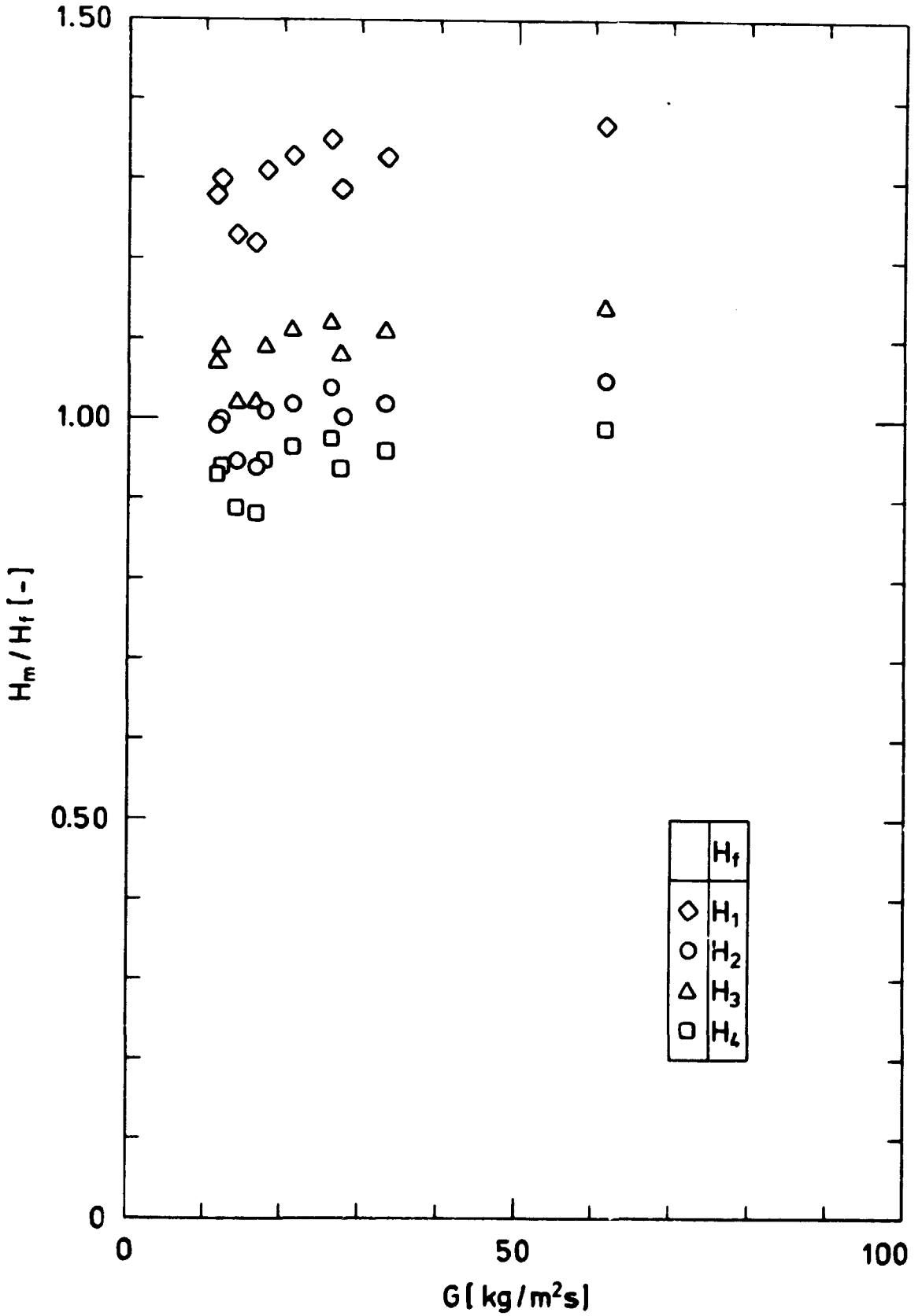

Fig. 3.44. The ratio H_m/H_f versus mass flux G
$\bar{t}_w$ = - 12 °C. $\Delta\bar{t}_{sub}$ = 5.0 °C ± 0.6 °C.

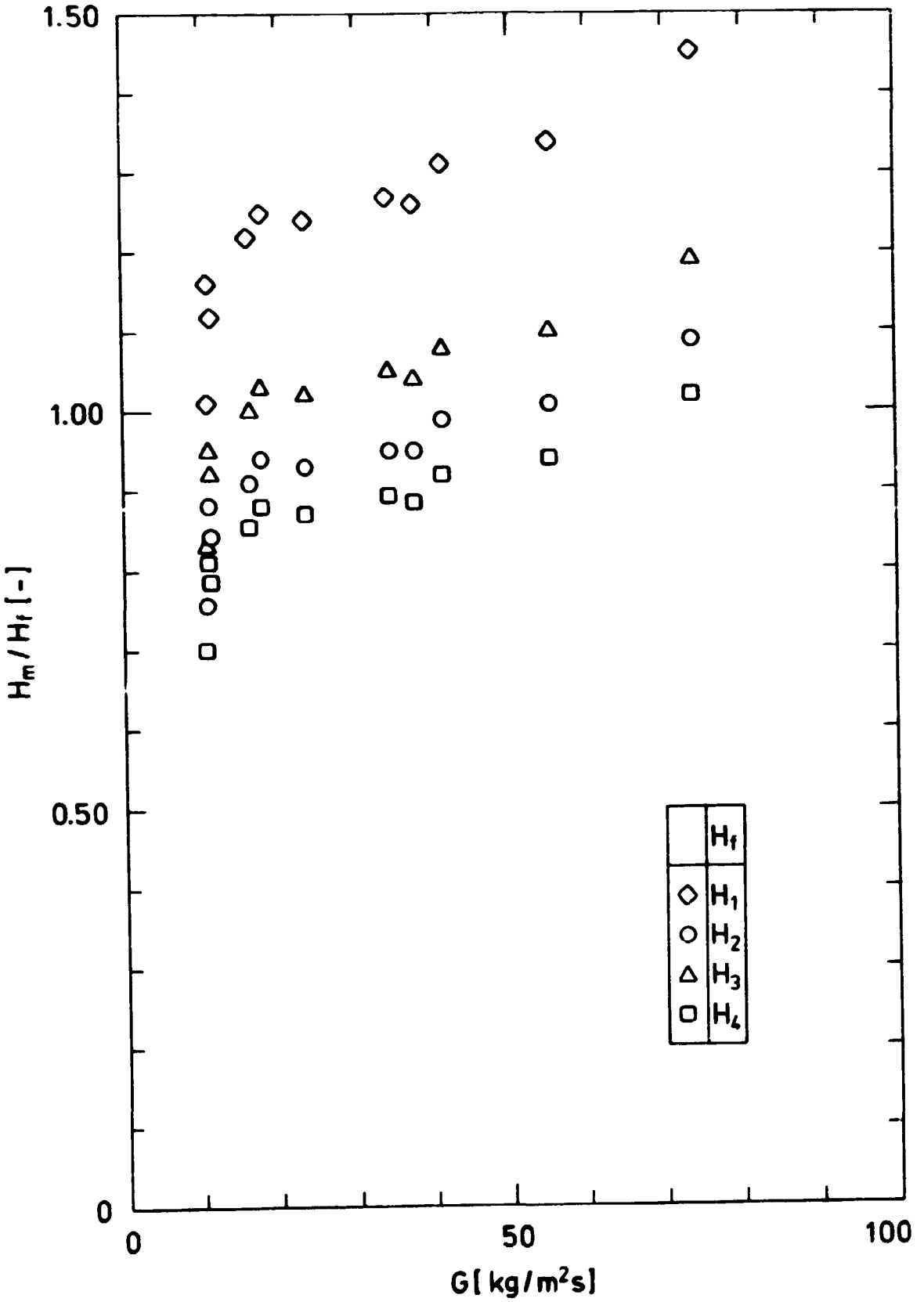

Fig. 3.45. The ratio H_m/H_f versus mass flux G.
$\bar{t}_w = -12^oC$. $\Delta t_{sub} = 6.5^oC \pm 0.5^oC$.

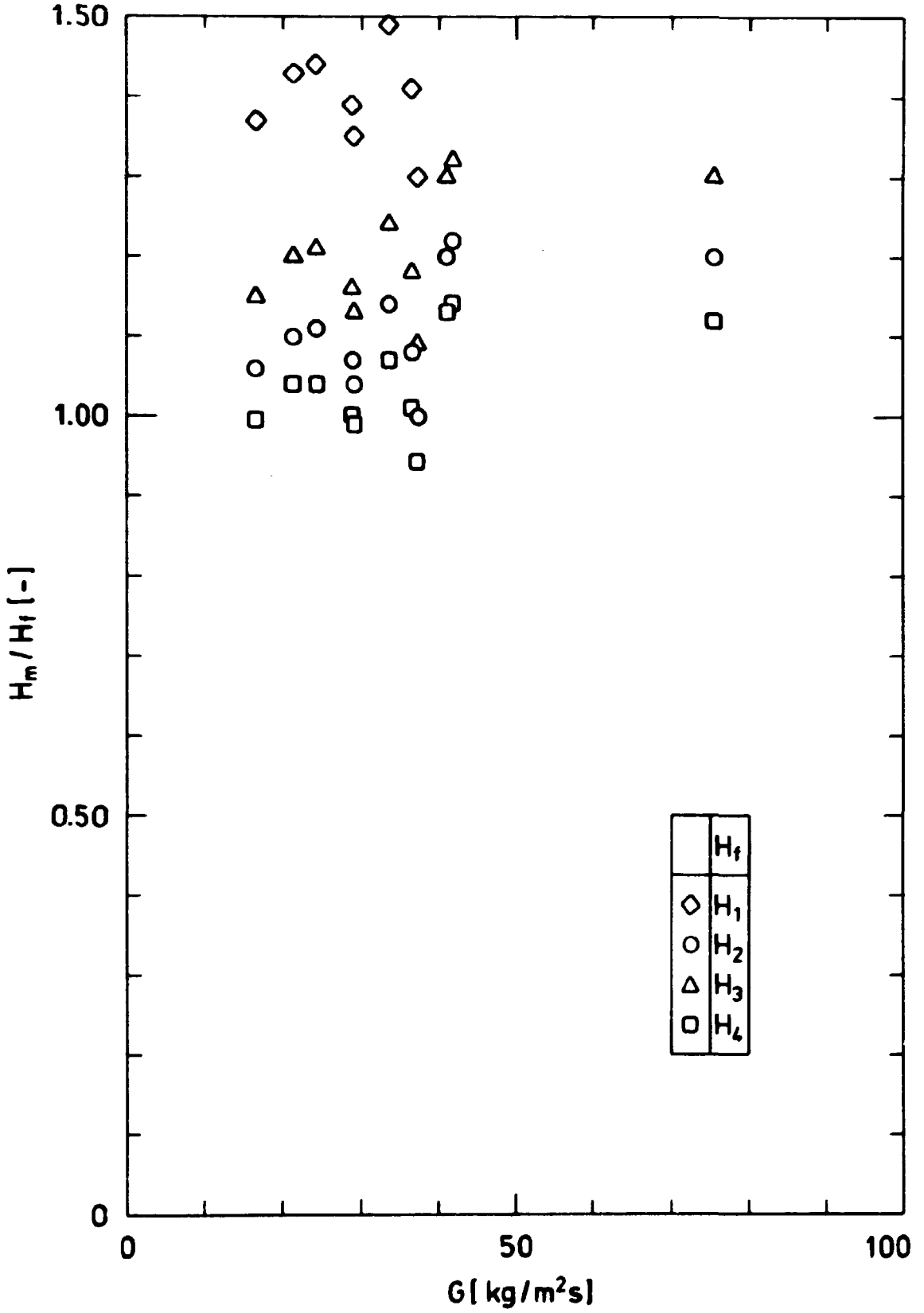

Fig. 3.46. The ratio H_m/H_f versus mass flux G.
$\bar{t}_w$ = - 12 °C. Δt_{sub} = 8.9 °C ± 0.7 °C.

Fig. 3.47. Inverse annular film boiling and change to dispersed droplet flow. G = 29.5 kg/m^{2}s and Δt_{sub} = 3.4^{o}C.

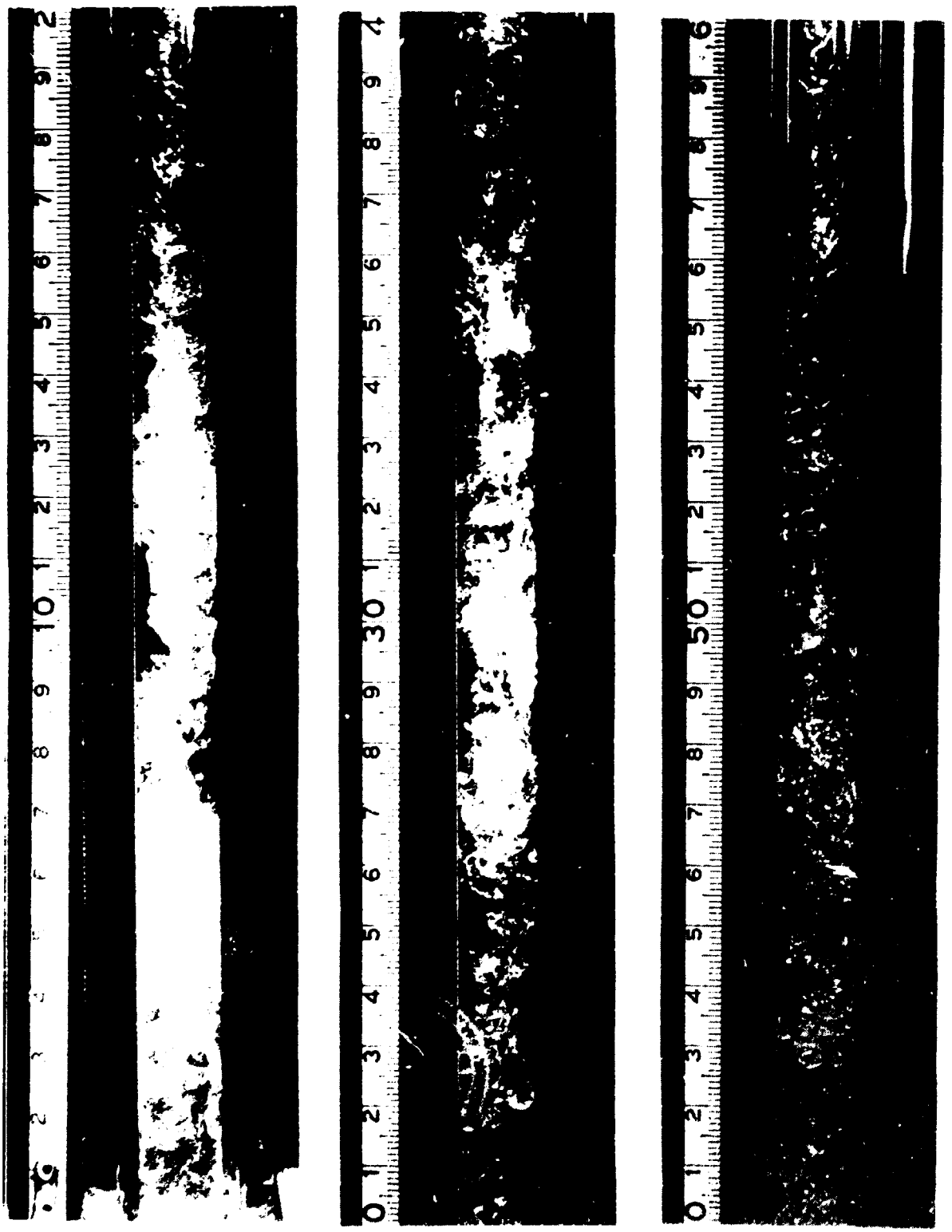

Fig. 3.48. Inverse annular film boiling and change to dispersed droplet flow. G = 60.1 kg/m^{2}s and Δt_{sub} = 3.7°C.

Fig. 3.49. Inverse annular film boiling and change to dispersed droplet flow. G = 70.0 kg/m^{2}s and Δt_{sub} = 8.0°C.

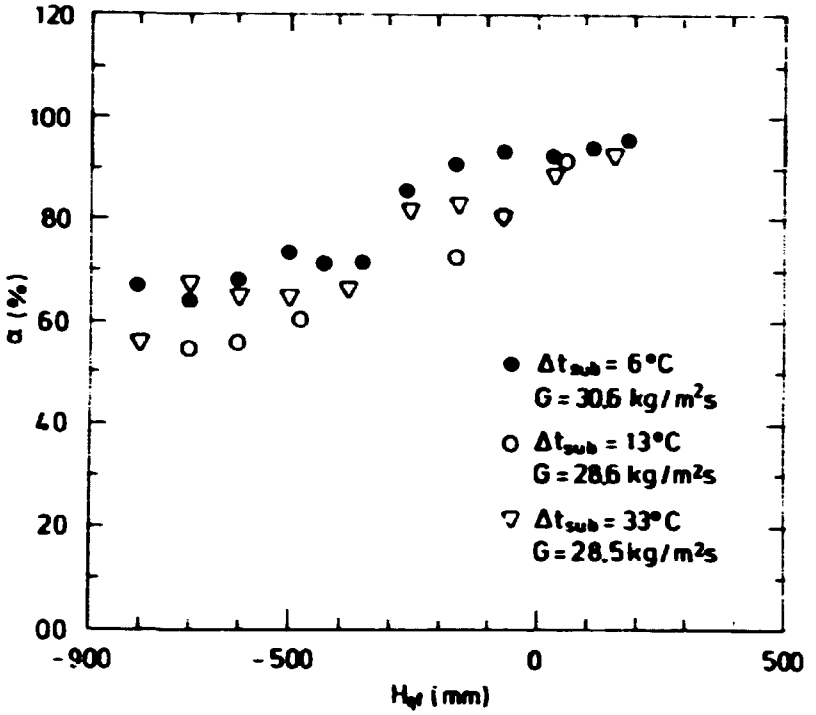

Fig. 3.50. The void fraction α versus elevation above the quench front, H_{qf}. Reflood of heated steel tube using subcooled water as coolant. Wall temperature before reflood 650°C ± 50°C.

4. COMPARISON BETWEEN EXPERIMENTAL DATA AND CALCULATIONS MADE WITH THE COMPUTER CODE RISQUE-N2

This section presents an investigation of the performance of the computer code RISQUE-N2, a modified version of the RISQUE-T code.

The calculations are compared with experimental data from inverse annular boiling experiments with nitrogen.

4.1. Description of the code

The original computer code RISQUE-T developed by Eget and Andersen (1977) was designed to model a transient one-dimensional steam-water two-phase flow.

The model used in RISQUE-T is a one-dimensional two-fluid model. This model is in unchanged form used in the modified version, RISQUE-N2. In the two-fluid model each phase is described by conservation equations for mass, momentum, and energy leading to a system of six equations. The numerical method used to solve these equations is an extended form of the Turner finite difference scheme (Turner (1972)).

The six equations are solved for the following dependent variables:

Gas mass flow rate	$m_g = \alpha \rho_g V_g A$
Liquid mass flow rate	$m_\ell = \alpha \rho_\ell V_\ell A$
Void fraction	α
Pressure	P
Enthalpy of gas	$\Delta h_g = h_g - h_{g,sat}$
Enthalpy of liquid	$\Delta h_\ell = h_\ell - h_{\ell,sat}$

The conservation equations are described in a general form in Appendix A.

Closure of the system of conservation equations requires expressions for the physical properties of both the liquid and gas phases. Further, a set of constitutive equations for the following quantities are required.

The interactions of the fluids with the walls are described by

- wall friction	F_{wg}, $F_{w\ell}$
- wall heat transfer	Q_{wg}, $Q_{w\ell}$
- wall mass transfer	Γ_w,

and the transfers of mass, momentum, and heat across the interface are described by

- interfacial mass transfer Γ_i
- interfacial momentum transfer F
- interfacial heat transfer Q_{ig}, $Q_{i\ell}$

The differences between the new version RISQUE-N2 compared to RISQUE-T are in the choice of constitutive equations. The physical properties of water and steam are replaced by a newly developed set of routines for the physical properties of nitrogen, liquid, and gas.

These routines are described in Appendix C and in a report by Ottosen and Mannov (1980) where the routines are used to tabulate the physical properties of nitrogen. The fitted expressions have been compared with experimental data, and show a maximum error of 1%.

4.2. Constitutive equations for inverse annular film boiling and dispersed droplet flow

The original constitutive equations for friction, heat, and mass transfer as used in RISQUE-T depend in a rather simple way on the actual flow regime. The expressions appearing in the gas equations vanish for $\alpha \to 0$ and those in the liquid equations vanish for $\alpha \to 1$.

To model inverse annular film boiling and dispersed droplet flow it was necessary to introduce a revised set of transfer equations. These new correlations are valid only for the inverse annular film boiling and dispersed droplet flow regimes, and therefore the present RISQUE-N2 is applicable only to calculations in these regimes.

If RISQUE-N2 were to be equipped with the appropriate constitutive equations the code could of course be used for calculations in other flow regimes.

4.2.1. Wall friction

Wall friction is expressed in the same form as is used in RISQUE-T and becomes

$$F_{wg} = F'_{wg}\, m_g \text{ , and} \tag{4.1}$$

$$F_{w\ell} = 0. \tag{4.2}$$

The liquid wall friction is set to zero as the wall is dry in case of inverse annular film boiling and dispersed droplet flow.

The single-phase friction factor F'_{wg} is calculated as follows:

$$F'_{wg} = f_g \frac{|V_g|}{2D_h A} \text{ , and} \tag{4.3}$$

$$f_g = \max \begin{cases} f_{g,lam} \\ f_{g,turb} \end{cases}, \tag{4.4}$$

where the laminar frictions factor is defined by

$$f_{g,lam} = \frac{64}{Re_g}, \tag{4.5}$$

and the turbulent friction factor is given implicitly by the Moody-Colebrook equation (Streeter (1966)).

Thus

$$\frac{1}{\sqrt{f_{g'turb}}} = -\,0.86 \ln\left(\frac{\varepsilon/D_h}{3.7} + \frac{2.51}{Re^*_g \sqrt{f_{g'turb}}}\right), \tag{4.6}$$

$$\text{where } Re^*_g = \begin{cases} 2000 \text{ for } Re_g \leq 2000 \\ Re_g \text{ for } Re_g > 2000 \end{cases}, \tag{4.7}$$

$$\text{and} \quad Re_g = \frac{|V_g|\, D_h\, \rho_g}{\mu_g}. \tag{4.8}$$

4.2.2. Wall heat transfer

The rate of heat transfer from wall to gas and liquid can be written in the following general forms:

$$Q_{wg} = \alpha Q_{wg}" \ (T_w - T_g) \ , \qquad \text{and} \tag{4.9}$$

$$Q_{wl} = (1-\alpha) \ Q_{wl}" (T_w - T_l) \ , \tag{4.10}$$

or in terms of the dependent variables Δh_g and Δh_l,

$$Q_{wg} = \alpha Q_{wg}" (\Delta T_w - \frac{1}{c_{pg}} \Delta h_g) \ , \text{ and} \tag{4.11}$$

$$Q_{wl} = (1-\alpha) \ Q_{wl}" (\Delta T_w - \frac{1}{c_{pl}} \Delta h_l) \ , \tag{4.12}$$

where $\Delta T_w = T_w - T_{sat}$. (4.13)

In the case of inverse annular film boiling and dispersed droplet flow, when the wall is dry and the wall temperature is above the minimum film boiling temperature, the heat transfer coefficients $Q_{wg}"$ and $Q_{wl}"$ are computed as follows:

Let $Q_w" = Q_{wg}" = Q_{wl}"$, where

$$Q_w" = Nu_w \frac{P_{heat}}{A} \frac{k_g}{D_h} \ . \tag{4.14}$$

For inverse annular flow the Nusselt number Nu_w is computed from the correlation given by Berenson (1961) and for dispersed droplet flow from a correlation proposed by Munthe Andersen (1976).

In order to get a continuous transition from the inverse annular flow regime to the droplet flow regime the Nusselt number in the code is computed as follows:

$$Nu_w = \min \begin{Bmatrix} Nu_{ia} \\ Nu_d \end{Bmatrix} \ . \tag{4.15}$$

Inverse annular film boiling,

$$Nu_{ia} = 0.425 \left(\frac{k_g^3 (\rho_\ell - \rho_g)\ g\ h_{\ell g}^*}{\nu_g\ L\ (T_w - T_{sat})} \right)^{\frac{1}{4}} \frac{D_h}{k_g} , \tag{4.16}$$

where $L = \sqrt{\frac{\sigma \ell}{g(\rho_\ell - \rho_g)}}$ and $h_{\ell g}^* = h_{\ell g} + 0.5\ c_{pg}\ (T_w - T_{sat})$. (4.17)

Dispersed droplet flow,

$$Nu_d = 2x - 1 + \frac{(Nu_{g,s} + 1)^2}{Nu_{g,s} + 1 + 2x} , \tag{4.18}$$

where the single-phase gas Nusselt number is given by

$$Nu_{g,s} = \max \begin{Bmatrix} 4.36 \\ 0.023\ Re_g^{0.8}\ Pr_g^{0.4} \end{Bmatrix} \tag{4.19}$$

and the droplet concentration parameter is defined by

$$x = \frac{D_h}{2d} \sqrt{\frac{(1-\alpha)\ 6\ Nu_{dr} (h_{\ell g} + h_g - h_{g,sat})}{h_{\ell g}}} , \tag{4.20}$$

where

$$Nu_{dr} = 2 + 0.75\ Re_d^{0.5} , \text{ and} \tag{4.21}$$

$$Re_d = \frac{\rho_g\ d\ |V_g - V_\ell|}{\mu_g} . \tag{4.22}$$

This droplet flow correlation fulfills the single-phase condition

$$Nu_d \to Nu_{g,s} \text{ for } \alpha \to 1.0 .$$

4.2.3. Wall mass transfer

As described previously, the heat transfer from wall to liquid is given by

$$Q_{w\ell} = (1-\alpha)\ Q_{w\ell}''\ (\Delta T_w - \frac{1}{c_{p\ell}}\ \Delta h_\ell)\ . \tag{4.23}$$

It is now supposed that part of this heat flux leads directly to evaporation; thus, the wall mass transfer can be written as follows:

$$\Gamma_w = \Gamma_{w0} + \Gamma_w'\ \Delta h_\ell\ , \tag{4.24}$$

where

$$\Gamma_{w0} = \alpha(1-\alpha)\ \Gamma_{w00}\ , \tag{4.25}$$

and

$$\Gamma_w' = \alpha(1-\alpha)\ \Gamma_w''\ \Delta h_\ell\ . \tag{4.26}$$

Suppose $\Gamma_w = \alpha(1-\alpha)\ \frac{Q_{w\ell}}{h_{\ell g}}$; then Γ_{w00} and Γ_w'' are defined by

$$\Gamma_{w00} = (1-\alpha)\ Q_{w\ell}''\ \frac{\Delta T_w}{h_{\ell g}}\ , \tag{4.27}$$

and $$\Gamma_w'' = -(1-\alpha)\ Q_{w\ell}''\ \frac{1}{c_{p\ell} h_{\ell g}}\ . \tag{4.28}$$

This model for the wall mass transfer has been chosen because it gives a relatively high rate of transfer at small values of the void fraction, where there is a possibility that the liquid will come very near to the hot wall leading to an evaporation. In the cases of $\alpha \to 0$ and $\alpha \to 1$, the wall mass transfer is assumed to vanish, corresponding to the formulation above.

The deduced Γ_w is of the form

$$\Gamma_w \simeq \alpha(1-\alpha)^2\ . \tag{4.29}$$

This leads to the following dependence on the void fraction:

$\alpha(1-\alpha)^2$	α
0.000	0.0
0.081	0.1
0.128	0.2
0.147	0.3
0.144	0.4
0.125	0.5
0.084	0.6
0.063	0.7
0.032	0.8
0.009	0.9
0.000	1.0

4.2.4. Interfacial momentum transfer

The interfacial momentum transfer is defined as

$$F = F_{stat} + F_{dyn} \tag{4.30}$$

Where the computed F_{stat} is given by Andersen (1975) as

$$F_{stat} = \alpha(1-\alpha)\ F_{stat}''\ (V_g - V_\ell)\ , \tag{4.31}$$

where

$$F_{stat}'' = \frac{3}{4}\frac{1}{d}\ \bar{\rho}\ C_d\ |V_g - V_\ell|\ . \tag{4.32}$$

The drag coefficient is taken from Munthe Andersen (1973) and becomes

$$C_d = \begin{cases} \dfrac{24}{\bar{Re}_d} & \text{for } \bar{Re}_d \leq 0.71 \\ 0.4 + 25.4\ \bar{Re}_d^{-0.8} & \text{for } \bar{Re}_d > 0.71 \end{cases}\ , \tag{4.33}$$

where

$$\bar{Re}_d = \frac{d\,\bar{\rho}\,|V_g - V_\ell|}{\bar{\mu}} \quad . \tag{4.34}$$

The dynamic contribution to the interfacial momentum transfer is taken from Drew et al. (1978) as

$$F_{dyn} = K\left(\frac{D_\ell V_g}{Dt} - \frac{D_g V_\ell}{Dt}\right) , \qquad \text{where} \tag{4.35}$$

$$K = k\,\alpha(1-\alpha)\,\bar{\rho} , \tag{4.36}$$

$$\frac{D_\ell V_g}{Dt} = \frac{\partial V_g}{\partial t} + U_\ell \frac{\partial V_g}{\partial x} , \qquad \text{and} \tag{4.37}$$

$$\frac{D_g V_\ell}{Dt} = \frac{\partial V_\ell}{\partial t} + U_g \frac{\partial V_\ell}{\partial x} . \tag{4.38}$$

The values of k, U_ℓ, and U_g are unspecified but can be changed during test runs with the program.

For the resulting calculations the values of these parameters are set as follows:

$$k = 1,\ U_\ell = V_\ell, \text{ and } U_g = V_g .$$

The introduction of the correlation for the added mass effect, F_{dyn} as suggested by Drew et al. (1978) and Andersen et al. (1976), limits the relative acceleration of the phases, and thus eliminates instabilities of the solution scheme.

4.2.5. Interfacial mass transfer

The interfacial mass transfer rate is defined as

$$\Gamma_i = \alpha(1-\alpha)\,\Gamma_i''\,\Delta h_\ell , \tag{4.39}$$

where

$$\Gamma_i'' = \begin{cases} 1000 \dfrac{1}{c_{p\ell}^2} \Delta h_\ell & \text{if } \Delta h_\ell \geq 0.0 \\ 0.0 & \text{if } \Delta h_\ell < 0.0 \ . \end{cases} \tag{4.40}$$

This model is valid only for evaporation and does not include condensation.

4.2.6. Interfacial heat transfer

The interface-to-gas heat transfer is computed as proposed in RISQUE-T

$$Q_{ig} = -\alpha(1-\alpha)\ Q_{ig}''\ \Delta h_g \ , \tag{4.41}$$

where

$$Q_{ig}'' = 6\ Nu_d \frac{k_g}{d^2\ c_{pg}} \ . \tag{4.42}$$

For dispersed droplets of diameter d the following correlation for the Nusselt number is used:

$$Nu_d = 3.2 + 0.75\ Re_d^{0.5}\ Pr_g^{0.33} \ , \tag{4.43}$$

where

$$Re_d = \frac{|V_g - V_\ell|\ d\ \rho_g}{\mu_g} \ . \tag{4.44}$$

In order to satisfy the energy equation for the interface the following equation can be written:

$$(\Gamma_w + \Gamma_i)\ h_{\ell g} + Q_{ig} + Q_{i\ell} = 0 \ . \tag{4.45}$$

The interface-to-liquid heat transfer is then found by solving this equation, and it becomes

$$Q_{i\ell} = -\left[h_{\ell g}(\Gamma_w + \Gamma_i) + Q_{ig}\right] \ . \tag{4.46}$$

4.2.7. Boundary conditions and input parameters

In order to solve the two-phase equations it is necessary to specify some boundary conditions.

The following inlet and outlet boundary conditions are required to simulate the experiments.

Inlet boundary conditions:

Inlet mass flow $m_{in} = m_{gin} + m_{\ell in}$

Inlet void fraction α_{in}

Inlet enthalpy of gas liquid Δh_{gin} and $\Delta h_{\ell in}$

Inlet relative velocity V_{rin}

Outlet boundary condition:

Pressure p_{out}

The values of m_{in}, α_{in}, $\Delta h_{\ell in}$, and p_{out} are experimental parameters and therefore known before the calculation is performed.

The only unknown boundary conditions are the gas enthalphy and relative velocity. The values of these two quantities are chosen as follows:

$$\Delta h_{gin} = 0.0 \text{ J/kg} \quad \text{and} \quad V_{rin} = 0.2 \text{ m/s} .$$

The vaporization starts at the inlet of the test section. Consequently, the superheating of the gas phase has a value close to zero.

The mean droplet diameter used in the correlation for interfacial momentum transfer and interfacial heat transfer is chosen to be 1 mm. These correlations are used both for inverse annular film boiling and dispersed droplet flow, whereas the correlation for wall heat transfer given by Eq. (4.14) is flow-regime dependent. In order to account for the small droplets occuring in the flow regime of dispersed droplet flow, the droplet diam-

eter used in the droplet concentration parameter, Eq. (4.20), is set so as to represent the smaller value, 0.3 mm.

The temperature of the inner wall of the flow channel is chosen to be $-4.3^{o}C$, which matches the conditions of the experiments. The geometry of the test section is as follows:

Length $H = 0.740$ m
Diameter $D_h = 0.0136$ m

For practical reasons it was impossible to measure the void fraction directly at the inlet. The first position for void measurement was at a distance of 45 mm from the inlet.

Consequently, the calculations are performed in a way such that the inlet boundary conditions α_{in} are chosen equal to the value measured at the level of 45 mm. Thus, the total length of the flow channel used for the calculations becomes $H = 0.695$ m.

The following cases have been computed:

Run No.	G kg/m^2s	Δt_{sub} ^{o}C	p_{out} N/m^2
1	50	0.0	10^5
2	50	5.7	10^5
3	70	0.0	10^5
4	70	5.7	10^5

4.2.8. Discussion of results

Figs. 4.1, 4.2, 4.3, and 4.4 show the calculated results of the wall heat transfer rate compared with measurements.

In order to get the values of the wall heat transfer rates for inverse annular film boiling and dispersed droplet flow, measurements of heat transfer in the lower and upper part of the test section have been made.

The measured mean values are plotted as vertical lines, and the calculated curves are marked RISQUE-N2.

Figs. 4.1 and 4.2 show the results when the inlet flow is at saturation temperature and the mass fluxes are G = 50 and 70 kg/m^2s.

The calculated results are smaller than the measured ones. The modelling of the change from inverse annular flow to dispersed droplet flow is the main reason for this deviation. The calculated transition from inverse annular film boiling heat transfer to dispersed-droplet flow heat transfer takes place too early.

Figs. 4.3 and 4.4 show plots where the inlet is subcooled and $\Delta t_{sub} = 5.7^{o}C$. This leads to improved agreement between computed and measured results. In these cases the change from inverse annular flow to dispersed droplet flow agrees with the experiments.

In all four examples the rates of heat transfer in the dispersed droplet flow regime are smaller than the experiments indicate.

The choice of droplet diameter is important; a smaller droplet diameter leads to a larger rate of heat transfer.

In Figs. 4.5 and 4.6 the computed relative velocity is plotted versus the level above inlet. If the inlet flow is subcooled, as shown in Fig. 6, the relative velocity is nearly constant close to the inlet. Only near the transition from inverse annular flow to dispersed droplet flow, does the relative velocity start to increase.

In Figs. 4.7 and 4.8 the measured axial void profile and the computed profile are compared. Here the agreement between experiment and theory is good, and difficulties arise only in the transition region.

The computed results obtained with the code RISQUE-N2 indicate that it is possible to model a two-phase flow in a heated tube using a one-dimensional model.

However, the modelling of the change from one flow regime to another gives rise to some problems.

Furthermore, the heat transfer correlation used in the flow of dispersed droplet flow must be improved. In order to do this, it is necessary to know the temperature of the gas phase, because the two phases are not in thermodynamic equilibrium. If the heat flux from wall to fluid, superheating of the gas, and the mean void fraction are all known, it would be much easier to make constitutive equations for Q_{wg}, $Q_{w\ell}$ and Q_{ig}. The code RISQUE-N2 could be a very good tool to verify the accuracy of such models.

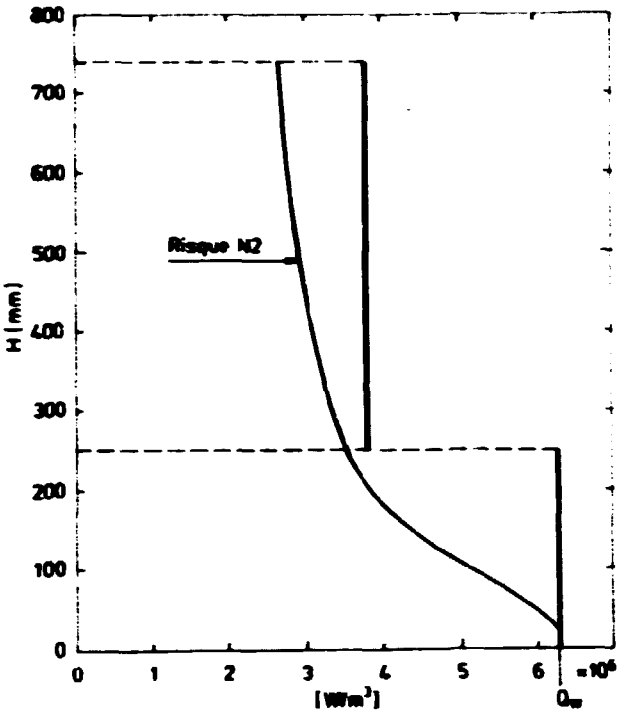

Fig. 4.1. Wall heat transfer rate versus level above inlet at mass flux G = 50 kg/m^{2}s and Δt_{sub} = 0.0°C.

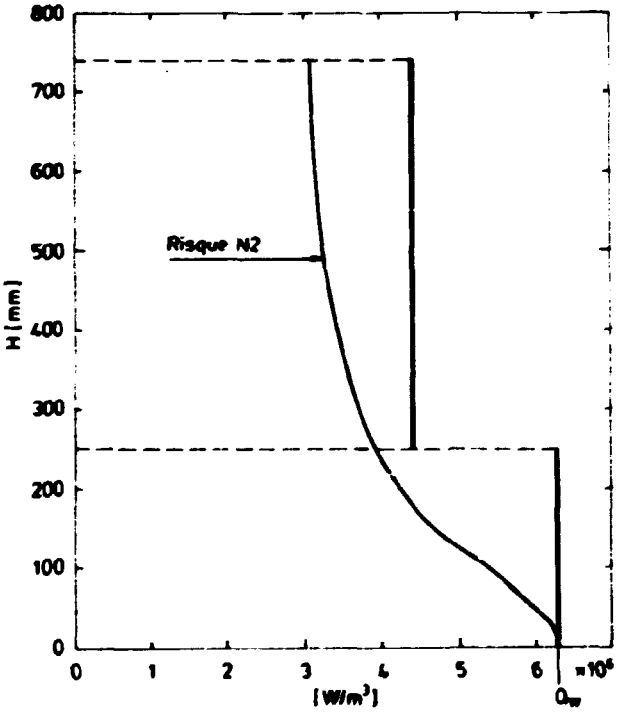

Fig. 4.2. Wall heat transfer rate versus level above inlet at mass flux G = 70 kg/m^{2}s and Δt_{sub} = 0.0°C.

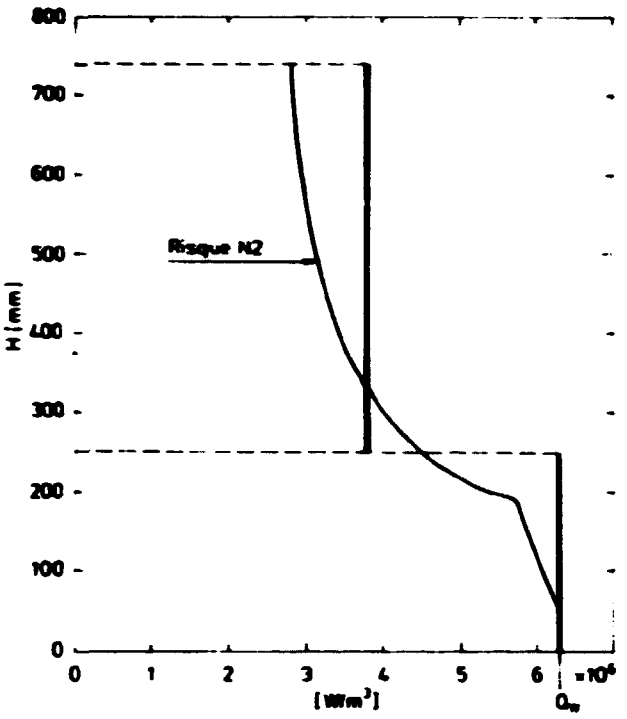

Fig. 4.3. Wall heat transfer rate versus level above inlet at mass flux G = 50 kg/m^{2}s and Δt_{sub} = 5.7°C.

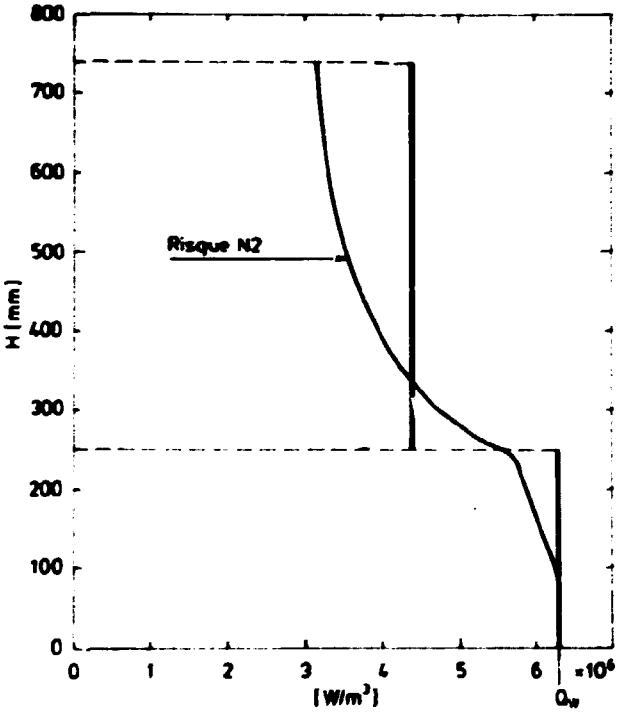

Fig. 4.4. Wall heat transfer rate versus level above inlet at mass flux G = 70 kg/m^{2}s and Δt_{sub} = 5.7°C.

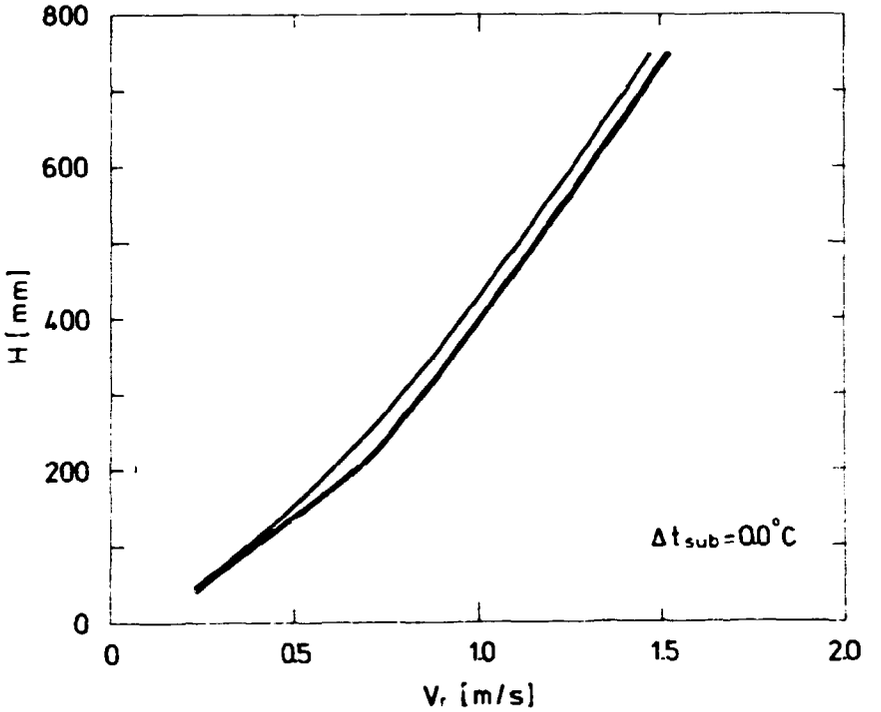

Fig. 4.5. Calculated relative velocity $V_r = V_g - V_\ell$ versus level above inlet.

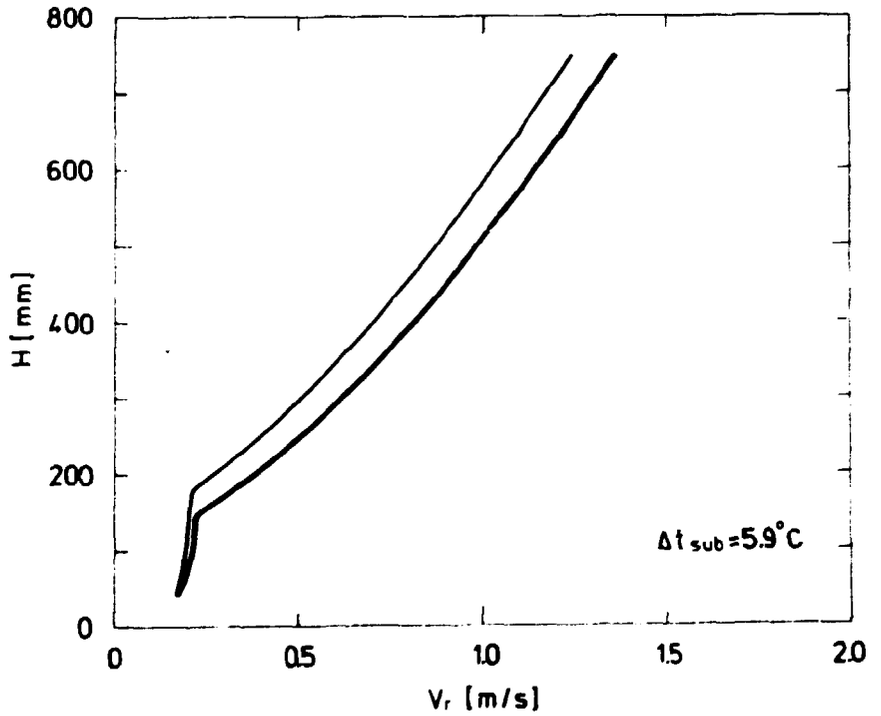

Fig. 4.6. Calculated relative velocity $V_r = V_g - V_\ell$ versus level above inlet.

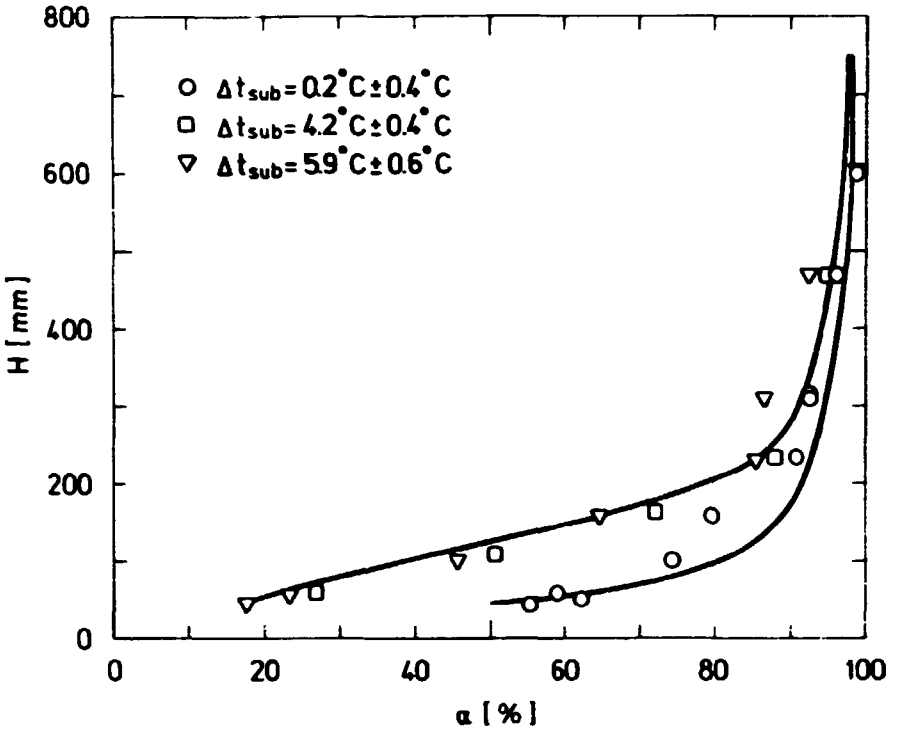

Fig. 4.7. Measured and calculated axial void profile. G = 50 kg/m^{2}s. The curves are calculations made with RISQUE-N2 simulating the measured profiles obtained at an inlet subcooling of Δt_{sub} = 0.2 ^{o}C and Δt_{sub} = 5.9 ^{o}C.

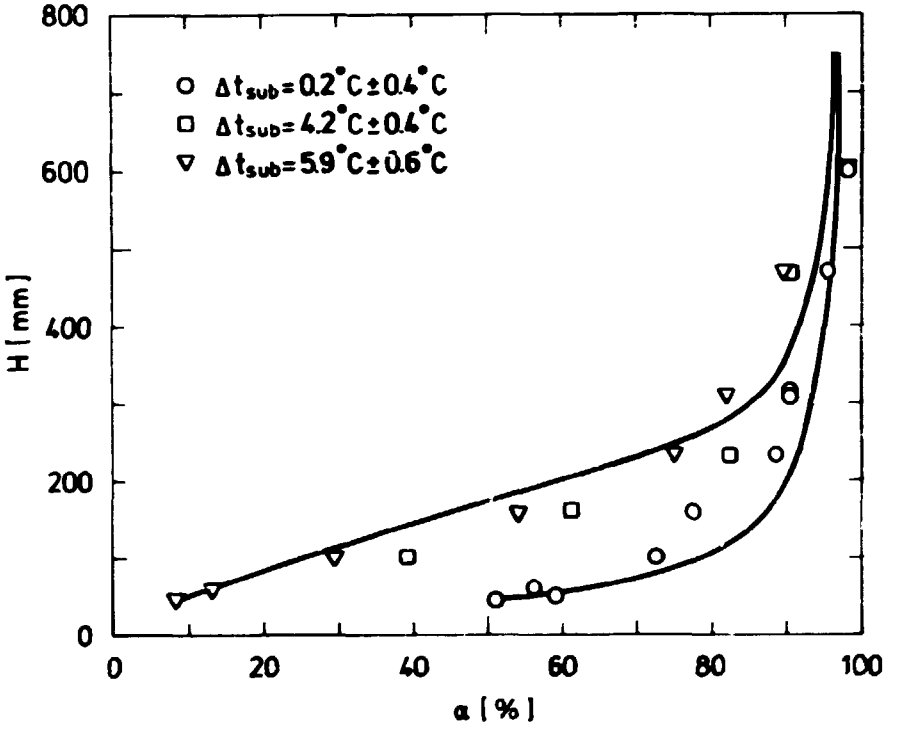

Fig. 4.8. Measured and calculated axial void profile. G = 70 kg/m^{2}s. The curves are calculations made with RISQUE-N2 simulating the measured profiles obtained at an inlet subcooling of Δt_{sub} = o.2 ^{o}C and Δt_{sub} = 5.9 ^{o}C.

5. SUMMARY AND CONCLUSION

An experimental and theoretical investigation of the inverse annular and dispersed droplet flow in a two-phase flow of nitrogen gas-liquid was performed.

An experimental technique has been developed making it possible to study a stationary flow consisting of inverse annular film flow and the change to dispersed droplet flow in a heated glass tube using liquid nitrogen as flow medium.

Equipment to measure voids using the γ-ray absorption method has been developed. It consists of electronic instruments and a detector system that have proved their applicability both at calibration tests and at measurements of axial void fraction distribution in the two-phase flow under investigation.

It has been possible to perform measurements of heat flux and thermodynamic quality with reasonably good accuracy, due to use of a special method of flow rate measurements using tension weighing cells combined with accurate measurements of temperature.

The heat transfer for inverse annular and dispersed droplet flow has been measured separately. A comparison has been performed between measured coefficients of heat transfer and different known correlations. Some of the correlations fit the data very well which is interesting because the original correlations have not been compared with data obtained in a forced flow.

The glass test section gives possibilities of visual and photographic observations of the actual flow patterns.

The visual observations show an inverse annular flow pattern consisting of a dense core of liquid flowing in the middle of the flow channel isolated from the wall by a thin film of gas.

The glass test section has shown good properties in all respects, and it is recommended that such a facility be used in investigations of other diabatic two-phase flows.

A test section for investigation of inside reflood with water of a single heated steel tube has been constructed. Measurements of void during the reflood indicate that the dominant flow regime below the quench front is annular film flow. As a consequence of this the flow regime in the post dry-out region becomes dispersed droplet flow. However, the conclusion of this observation must be a recommendation of more experiments in order to investigate how the type of flow regime is controlled with respect to different parameters such as heat flux, wall temperature, mass flux, and inlet subcooling.

Experimental data from the nitrogen experiments have been compared to calculations with the one-dimensional, six equation computer code RISQUE-N2. The calculated axial void profiles are in good agreement with the measured ones. The computed rates of heat transfer agree fairly well with measurements. However, the modelling of the change from inverse annular film to dispersed droplet flow gives rise to some deviation and could undoubtly have been improved. The main problem with a six-equation scheme is to be able to model the interfacial transfers of mass, momentum, and heat. Therefore, measurements of the superheating of the gas, droplet sizes and relative velocities would be of great advantage for further developments of such models. The glass test section gives many possibilities of making new and more detailed investigations in order to achieve a better understanding of the flow patterns important in the nuclear safety analysis.

ADKNOWLEDGEMENTS

I wish to express my appreciation to Frank W. Cortzen for helpful discussions as well as his assistance in developing electronic equipment. In addition, I wish to express my gratitude to the entire staff of the Section of Experimental Heat Transfer (SEHT) for their invaluable help in the experimental work.

NOMENCLATURE

Main Symbols

A	m^2	flow area
C_d		drag coefficient
c_p	J/kgK	specific heat capacity at constant pressure
d	m	droplet diameter
D_o	m	diameter
D_h	m	hydraulic diameter
F	N/m^3	interfacial frictional force density
F_{sub}		effect of subcooling
F_{wg}	N/m^3	gas frictional force density due to wall friction
$F_{w\ell}$	N,m^3	liquid frictional force density due to wall friction
f_g		wall friction coefficient
f_g		wall friction factor
$f_{g,lam}$		friction factor for laminar flow
$f_{g,turb}$		friction factor for turbulent flow
g	m/s^2	acceleration of gravity
G	kg/m^2s	mass flux
Gr		Grashof's number
H	m	total length of flow channel
H_{qf}	mm	level above quench the front
h,H	J/kg	specific enthalpy
h,H	W/m^2K	coefficient of heat transfer
Δh	J/kg	specific enthalpy above saturation
$h_{\ell g}$	J/kg	latent heat of vaporization

i	cps	count rate
k	W/mK	thermal conductivity
K,k		coefficients in Eqs. (4.35) and (4.36)
m	kg/s	mass flow rate
n	cps	count rate
N		number of counts
Nu		Nusselt number
Nu_{dr}		Nusselt number used in Eq. (4.20)
$Nu_{g,s}$		Nusselt number for single phase gas
Nu_{ia}		Nusselt number for inverse annular flow
p	N/m^2	pressure
P_{heat}	m	heated perimeter
Pr		Prandtl number
q"	W/cm^2	heat flux
Q	W/m^2	heat flux
Q	W/m^3	rate of heat transfer
r		coefficient of determination
Re		Reynolds number
s		standard deviation
S	kg/s m^3	sink term
t	s	time
T	K	temperature
T	s	time
U	m/s	velocity
V	m/s	velocity
V_r	m/s	relative velocity
x	m	axial coordinate
x		droplet concentration parameter

x		quality
α		mean void fraction
α_{ml}		measured void fraction using Eq. (3.30)
α_{mo}		measured void fraction using Eq. (3.31)
Γ	$kg/s\ m^3$	mass rate of phase change
δ	m	wall thickness
ϵ	m	roughness height
θ		angle between gravity vector and positive x-axis
μ	cm^{-1}	coefficient of absorption
μ	Ns/m^2	dynamic viscosity
$\bar{\mu}$	Ns/m^2	mean mixture viscosity
τ	s	dead time
ν	m^2/s	kinematic viscosity
ρ	kg/m^3	density
$\bar{\rho}$	kg/m^3	mean mixture density $= \alpha\rho_g + (1-\alpha)\rho_\ell$
σ	N/m	surface tension
σ	cm^2/g	cross-section of absorption

Subscripts

c	corrected	stat	stationary
d	droplet flow	sub	subcooling
dyn	dynamic	unc	uncorrected
g	gas	w	wall
i	interface	wg	wall to gas
ig	interface to gas	wℓ	wall to liquid
iℓ	interface to liquid		
ℓ	liquid		
sat	saturation		
sing	singularity		

REFERENCES

Andersen, P.S. (1967). Steam Separation. Atomic Energy Commission, Section of Experimental Technology. Risø-M-1071, 14 pp. (Internal Report).

Andersen, P.S. (1975). The Treatment of Slip in the Dynamic Subchannel Program including Results for Critical Flow. Risø National Laboratory, NORHAV-D-15. (Internal Report).

Andersen, P.S., Astrup, P., and Rathmann, O. (1976). Characteristics of a One-Dimentional Two-Fluid Model for Two-Phase Flow. A study of Added Mass Effects. Risø National Laboratory. NORHAV-D-017. (Internal Report).

Barrett, P.R. (1974). Systematic Errors in the Discrete Time-Interval Transmission Method for the Estimation of Void Statistics in Boiling Channels. Nucl. Eng. Des. 30, 316-327.

Berenson, P.J. (1961). Film-Boiling Heat Transfer from a Horizontal Surface. J. Heat Transfer, 83, 351-358.

Bromley, A.L. (1950). Heat Transfer in Stable Film Boiling. Chem. Eng. Prog. 46, 221-227.

Drew, D.A., Cheng, L.Y., and Lahey, R.T. (1978). Virtual Mass Effects in Two-Phase Flow. NUREG/CR-0020, 43 pp.

Eget, L. and Andersen, P.S. (1977). The RISQUE-T Computer Programme. Risø National Laboratory. NORHAV-D-035. (Internal Report).

Evangelisti, R. and Lupoli, P. (1969). The Void Fraction in an Annular Channel at Atmospheric Pressure. Int. J. Heat Mass Transfer, 12, 699-711.

Freitas, R.L., Deruaz, R., and Pic, P. (1980). Void Fraction Measurement in a Reflooded Single Tube by a Neutron Scattering Technique. Paper presented at the European Two-Phase Flow Group Meeting, Glasgow, June 3-6. Paper B3.

Groeneveld, D.C. and Young, J.M. (1978). Film Boiling and Rewetting Heat Transfer during Bottom Flooding of a Hot Tube. In: Sixth International Heat Transfer Conference, Toronto, August 7-11, 1978. Vol. 5 (National Research Council of Canada) 89-94.

Hall, P.C. and Ardron, K.H. (1980). An Investigation of the Two-Phase Flow Generated During Bottom Flooding of a Heated

Glass Tube. Paper presented at the European Two-Phase Flow Group Meeting, Glasgow, June 3-6. Paper B5.

Handbook of Chemistry and Physics. (1976). 57th edition, CRC Press, Cleveland, Ohio).

Harms, A.A., Forrest, C.F. (1971). Dynamic Effects in Radiation Diagnosis of Fluctuating Voids. Nuc. Sc. Eng. 46, 408-413.

Hewitt, G.F., Kearsey, H.A., Lacey, P.M.C., and Pulling, D.J. (1965). Burnout and Film Flow in the Evaporation of Water in Tubes. Proc. Inst. Mech. Eng. 180, (part 3C). 206-215.

Ishii, M. (1975). Thermo-Fluid Dynamic Theory of Two-Phase Flow. (Eyrolles, Paris) 248 pp.

Knudsen, J.G. and Katz, D.L. (1958). Fluid Dynamics and Heat Transfer (McGraw-Hill, New York) 576 pp.

Landolt-Börnstein . (1967). Zahlenwerte and Funktionen aus Physik-Chemie-Astronomie-Geophysik und Technik. 6. Auflage. IV Band Technik. 4. Teil Wärmetechnik. (Springer Verlag, Berlin).

Larsen, A.M. (1976) Steam and Water Property Routines Received from the THOR Group at Brookhaven National Laboratory. Risø National Laboratory. NORHAV-D-030. (Internal Report).

Munthe Andersen, J.G. (1973). REMI/HEAT COOL, A Model for Evaluation of Core Heat-Up and Emergency Core Spray Cooling System Performance for Light-Water-Cooled Nuclear Power Reactors. Risø Report No. 296, 86 pp.

Munthe Andersen, J.G. (1976). CORECOOL: A Model for the Temperature Distribution and Two-Phase Flow in a Fuel Element under LOCA Conditions. NEDO-21325, 25 pp.

Munthe Andersen, J.G. (1977). Low-Flow Film Boiling Heat Transfer on Vertical Surfaces. Part I: Theoretical Model. AICHE Symp. Ser. 73, (164), 2-6.

Ottosen, P. and Mannov, G. (1980). Thermal and Mechanical Properties of Nitrogen. Risø-M-223o.

Rathmann, O. and Kortakorpi, J. (1979). "2 x Modified Bromley". An Inverse Annular Film Boiling Correlation including Liquid Subcooling. Risø National laboratory. NORHAV-D-74. (Internal Report).

Rouhani, S.Z. (1962). Void Measurements by the (γ, n) Reaction. Nucl. Sci. Eng. 14, 414-419.

Streeter, V.L. (1966). Fluid Mechanics, 4th ed. (McGraw-Hill,

New York) 705 pp.

Turner, W.J. (1972). A Stable Finite Difference Scheme for Transient Flow in a Boiling Channel. Energ. Nucl. (Milan) 19, 317-324.

Vargaftik, N.B. (1975). Tables on the Thermophysical Properties of Liquids and Gases. 2 ed. (Wiley, New York) 758 pp.

Würtz, J. (1978). An Experimental and Theoretical Investigation of Annular Steam-Water Flow in Tubes and Annuli at 30-90 bar. Risø Report No. 372, 141 pp.

PAPERS PRESENTED AT THE EUROPEAN TWO-PHASE GROUP MEETING

Ottosen, P. (1979). Inverted Annular Film Boiling in Liquid Nitrogen Flow. Paper presented at the European Two-Phase Flow Group Meeting, Ispra, June 5-8. Risø National Laboratory. NORHAV-D-71. (Internal Report).

Ottosen, P. (1980). Comparisons between Experimental Data from the Inverse Annular Film Boiling and the Dispersed Droplet Flow Regimes and Calculations with the Computer Code RISQUE-N2. European Two-Phase Flow Group Meeting, University of Strathclyde, Glasgow, June 3-6. Paper C6.

APPENDIX A

THE TWO-FLUID MODEL

The two-fluid model used in RISQUE-T and in the modified version RISQUE-N2 is based on the formulation of Ishii (1975).

The resulting conservation equations for mass, momentum, and energy are given in one-dimensional form as follows:

Mass conservation

Gas:

$$\frac{\partial}{\partial t}(\alpha\rho_g) + \frac{1}{A}\frac{\partial}{\partial x}(A\ \alpha\ \rho_g\ V_g) = \Gamma_w + \Gamma_i - S_g \qquad (1)$$

Liquid:

$$\frac{\partial}{\partial t}((1-\alpha)\rho_l) + \frac{1}{A}\frac{\partial}{\partial x}(A(1-\alpha)\rho_l V_l) = -(\Gamma_w+\Gamma_i) - S_l \qquad (2)$$

Momentum conservation

Gas:

$$\alpha\rho_g \frac{D_g V_g}{Dt} = -\alpha\frac{\partial p}{\partial x} - F_{wg} - F - \alpha\rho_g\ g\ \cos\theta - \Gamma_w V_g + \Gamma_i (V_i - V_g) - F_{g,sing} \qquad (3)$$

Liquid:

$$(1-\alpha)\rho_l \frac{D_l V_l}{Dt} = -(1-\alpha)\frac{\partial p}{\partial x} - F_{wl} + F - (1-\alpha)\rho_l\ g\ \cos\theta + \Gamma_w V_l - \Gamma_i\ (V_i - V_l) - F_{l,sing} \qquad (4)$$

Energy conservation

Gas:

$$\alpha\rho_g \frac{D_g h_g}{Dt} - \alpha \frac{D_g p}{Dt} = Q_{wg} + Q_{ig} - (\Gamma_w+\Gamma_i)\Delta h_g \qquad (5)$$

Liquid:

$$(1-\alpha)\rho_l \frac{D_l h_l}{Dt} - (1-\alpha) \frac{D_i p}{Dt} = Q_{wl} + Q_{il} + (\Gamma_w+\Gamma_i)\Delta h_l \qquad (6)$$

In the previous equations the substantive derivatives are defined as:

$$\frac{D_g}{Dt} \equiv \frac{\partial}{\partial t} + V_g \frac{\partial}{\partial x}$$

$$\frac{D_l}{Dt} \equiv \frac{\partial}{\partial t} + V_l \frac{\partial}{\partial x}$$

The conservation equations are derived on the assumption that the pressure of the two phases are equal and the quantities shown below are given by constitutive equations.

	Friction	Heat transfer	Momentum transfer	Mass transfer
Wall	F_{wg}, F_{wl}	Q_{wg}, Q_{wl}		Γ_w
Interface		Q_{ig}, Q_{il}	F	Γ_i
Singularities	$F_{g,sing}$, $F_{l,sing}$			
Sink terms				S_g, S_i

As dependent variables it is convenient to use the following set

$$m_g = \alpha \rho_g V_g A$$

$$m_l = (1-\alpha) \rho_l V_l A$$

$$\alpha \tag{7}$$

$$p$$

$$\Delta h_g = h_g - h_{g,sat}$$

$$\Delta h_l = h_l - h_{l,sat}$$

In order to express the conservation equations (1) through (6) in terms of these variables, it is necessary to express $\frac{\partial \rho_g}{\partial t}$ and $\frac{\partial \rho_l}{\partial t}$ in terms of $\frac{\partial p}{\partial t}$ and $\frac{\partial \Delta h}{\partial t}$.

Let

$$\rho_g = (h_g, p),$$

where

$$h_g = \Delta h_g + h_{g,sat} \text{ and } h_{g,sat} = h_{g,sat}(p);$$

then

$$\frac{\partial \rho_g}{\partial t} = \left(\frac{\partial \rho_g}{\partial p}\right)_h \frac{\partial p}{\partial t} + \left(\frac{\partial \rho_g}{\partial h}\right)_p \frac{\partial h_g}{\partial t} \tag{8}$$

$$\frac{\partial h_g}{\partial t} = \frac{\partial \Delta h_g}{\partial t} + \left(\frac{\partial h_g}{\partial p}\right)_{sat} \frac{\partial p}{\partial t} \quad . \tag{9}$$

Combining (8) and (9) gives

$$\frac{\partial \rho_g}{\partial t} = \left(\frac{\partial \rho_g}{\partial p}\right)_h \frac{\partial p}{\partial t} + \left(\frac{\partial \rho_g}{\partial h}\right)_p \left(\frac{\partial h_g}{\partial p}\right)_{sat} \frac{\partial p}{\partial t} + \left(\frac{\partial \rho_g}{\partial h}\right)_p \frac{\partial \Delta h_g}{\partial t} \quad . \tag{10}$$

The same procedure can be followed for $\rho_l = \rho_l(h_l, p)$ and then in terms of the dependent variables the conservation equations become:

Mass conservation

Gas:

$$\frac{1}{A}\frac{\partial m_g}{\partial x} + \rho_g \frac{\partial \alpha}{\partial t} + \alpha\left[\left(\frac{\partial \rho_g}{\partial p}\right)_h + \left(\frac{\partial \rho_g}{\partial h}\right)_p\left(\frac{\partial h_g}{\partial p}\right)_{sat}\right]\frac{\partial p}{\partial t}$$

$$+ \alpha\left(\frac{\partial \rho_g}{\partial h}\right)_p \frac{\partial \Delta h_g}{\partial t} = \Gamma_w + \Gamma_i - S_g \qquad (1a)$$

Liquid:

$$\frac{1}{A}\frac{\partial m_l}{\partial x} - \rho_l \frac{\partial \alpha}{\partial t} + (1-\alpha)\left[\left(\frac{\partial \rho_l}{\partial p}\right)_h + \left(\frac{\partial \rho_l}{\partial h}\right)_p\left(\frac{\partial h_l}{\partial p}\right)_{sat}\right]\frac{\partial p}{\partial t}$$

$$+ (1-\alpha)\left(\frac{\partial \rho_l}{\partial h}\right)_p \frac{\partial \Delta h_l}{\partial t} = -\left(\Gamma_w+\Gamma_i\right) - S_l \qquad (2a)$$

Momentum conservation

Gas:

$$\frac{1}{A}\frac{D_g m_g}{Dt} - \rho_g V_g \frac{D_g \alpha}{Dt} - \alpha V_g\left[\left(\frac{\partial \rho_g}{\partial p}\right)_h + \left(\frac{\partial \rho_g}{\partial h}\right)_p\left(\frac{\partial \rho_g}{\partial p}\right)_{sat}\right]\frac{D_g p}{Dt}$$

$$-\alpha V_g\left(\frac{\partial \rho_g}{\partial h}\right)_p \frac{D_g \Delta h_g}{Dt} = -\alpha\frac{\partial p}{\partial x} - F_{wg} - F - \alpha\rho_g g\cos\theta$$

$$- \Gamma_w V_g + \Gamma_i(V_i - V_g) + \alpha\rho_g V_g^2 \frac{1}{A}\frac{dA}{dx} - F_{g,sing} \qquad (3a)$$

Liquid:

$$\frac{1}{A}\frac{D_l m_l}{Dt} + \rho_l V_l \frac{D_l \alpha}{Dt} - (1-\alpha)V_l\left[\left(\frac{\partial \rho_l}{\partial p}\right)_h + \left(\frac{\partial \rho_l}{\partial h}\right)_p\left(\frac{\partial h_l}{\partial p}\right)_{sat}\right]\frac{D_l p}{Dt}$$

$$-(1-\alpha)V_l\left(\frac{\partial \rho_l}{\partial h}\right)_p \frac{D_l \Delta h_l}{Dt} = -(1-\alpha)\frac{\partial p}{\partial x} - F_{wl} + F - (1-\alpha)\rho_l g\cos\theta$$

$$+ \Gamma_w V_l - \Gamma_i(V_i - V_l) + (1-\alpha)\rho_l V_l^2 \frac{1}{A}\frac{dA}{dx} - F_{l,sing} \qquad (4a)$$

Energy conservation

Gas:

$$\alpha\left[\rho_g\left(\frac{\partial h_g}{\partial p}\right)_{sat} - 1\right]\frac{D_g p}{Dt} + \alpha\rho_g\frac{D_g \Delta h_g}{Dt} = Q_{wg} + Q_{ig} - (\Gamma_w+\Gamma_i)\Delta h_g \tag{5a}$$

Liquid:

$$(1-\alpha)\left[\rho_l\left(\frac{\partial h_l}{\partial p}\right)_{sat} - 1\right]\frac{D_l p}{Dt} + (1-\alpha)\rho_l\frac{D_l \Delta h_l}{Dt} = Q_{wl} + Q_{il} + (\Gamma_w+\Gamma_i)\Delta h_l \tag{6a}$$

If we define the field vector,

$$\underline{Y} = (m_g,\ m_l,\ \alpha,\ p,\ \Delta h_g,\ \Delta h_l)^t,$$

containing the six dependent variables then the six conservation equations (1a) through (6a) may be written as one matrix equation:

$$\underline{\underline{a}}\,\frac{\partial \underline{Y}}{\partial t} + \underline{\underline{b}}\,\frac{\partial \underline{Y}}{\partial x} + \underline{\underline{c}}\,\underline{Y} = \underline{d}\ , \tag{11}$$

where $\underline{\underline{a}}$, $\underline{\underline{b}}$ and $\underline{\underline{c}}$ are sixth-order coefficient matrices and $\underline{d}$ is a column vector with six elements.

The functional dependence of the constitutive equations upon the components of $\underline{Y}$ must be stated before $\underline{\underline{a}}$, $\underline{\underline{b}}$, $\underline{\underline{c}}$, and $\underline{d}$ can be written down explicitly. The elements of $\underline{\underline{a}}$, $\underline{\underline{b}}$, $\underline{\underline{c}}$, and $\underline{d}$ are given in Appendix B.

APPENDIX B

MATRIX COEFFICIENTS

This is an updated version of the elements of the matrices $\underline{\underline{a}}$, $\underline{\underline{b}}$, $\underline{\underline{c}}$ and $\underline{d}$ of Eq. (11) Appendix A. This version is revised from the old version proposed by Eget and Andersen (1977) including unpublished changes proposed by Andersen (1978).

The elements of the matrices are obtained from the conservation equations by introducing the appropriate expressions for constitutive equations.

The constitutive equations are linearized with respect to the dominant dependent variable.

The following definition of the constitutive equations have been used in the list of matrix coefficients:

Friction:

$$F_{wg} = F_{wg}' m_g$$

$$F_{wl} = F_{wl}' m_l$$

$$F_{g,sing} = \left[\frac{\alpha}{A^2 2\bar{\rho}} \frac{S_{sing}}{\Delta x} m_g\right] m_g + \left[\frac{\alpha}{A^2 2\bar{\rho}} \frac{S_{sing}}{\Delta x} (m_l + 2m_g)\right] m_l$$

$$F_{l,sing} = \left[\frac{(1-\alpha)}{A^2 2\bar{\rho}} \frac{S_{sing}}{\Delta x} m_g\right] m_g + \left[\frac{(1-\alpha)}{A^2 2\bar{\rho}} \frac{S_{sing}}{\Delta x} (m_l + 2m_g)\right] m_l$$

Heat transfer:

$$Q_{wg} = \alpha\, Q_{wg}''\, \Delta T_w - \alpha\, Q_{wg}'' \frac{1}{c_{pg}} \Delta h_g$$

$$Q_{wl} = (1-\alpha)\, Q_{wl}''\, \Delta T_w - (1-\alpha)\, Q_{wl}'' \frac{1}{c_{pl}} \Delta h_l$$

$$Q_{ig} = -\alpha(1-\alpha)\ Q_{ig}''\ \Delta h_g$$

$$Q_{il} = -\left[h_{lg}(\Gamma_w+\Gamma_i) + Q_{ig}\right]$$

Momentum transfer:

$$F = F_{stat} + F_{dyn}\ ,\ \text{where}$$

$$F_{stat} = \alpha(1-\alpha)\ F_{stat}''\left(\frac{m_g}{\alpha A\rho_g} - \frac{m_l}{(1-\alpha)A\rho_l}\right)$$

$$F_{dyn} = K\left(\frac{D_l V_g}{Dt} - \frac{D_g V_l}{Dt}\right)\ ,\ \text{where}$$

$$K = k\ \alpha(1-\alpha)\bar{\rho}$$

Mass transfer:

$$\Gamma_w = \Gamma_{wo} + \Gamma_w'\ \Delta h_l = \alpha(1-\alpha)\ \Gamma_{woo} + \alpha(1-\alpha)\ \Gamma_w''\ \Delta h_l$$

$$\Gamma_i = \alpha(1-\alpha)\ \Gamma_i''\ \Delta h_l$$

$$S_g = S_{go} + S_g'p$$

$$S_l = S_{lo} + S_l'p$$

MASS CONSERVATION FOR THE GAS

$$a_{13} = \rho_g$$

$$a_{14} = \alpha\left(\left(\frac{\delta\rho_g}{\delta p}\right)_h + \left(\frac{\delta\rho_g}{\delta h}\right)_p \left(\frac{\delta i_G}{\delta p}\right)_{sat}\right)$$

$$a_{15} = \alpha\left(\frac{\delta\rho_g}{\delta h}\right)_p$$

$$b_{11} = \frac{1}{A}$$

$$c_{14} = S_g'$$

$$c_{16} = c_{16}' + c_{16}'' \qquad \text{where}$$

$$c_{16}' = -\alpha(1-\alpha)\ \Gamma_i''$$

$$c_{16}'' = -\alpha(1-\alpha)\ \Gamma_w''$$

$$d_1 = d_1' + d_1'' \qquad \text{where}$$

$$d_1' = \Gamma_{wo}$$

$$d_1'' = -S_{go}$$

MASS CONSERVATION FOR THE LIQUID

$$a_{23} = -\rho_l$$

$$a_{24} = (1-\alpha)\left(\left(\frac{\delta\rho_l}{\delta p}\right)_h + \left(\frac{\delta\rho_l}{\delta h}\right)_p \left(\frac{\delta h_l}{\delta p}\right)_{sat}\right)$$

$$a_{26} = (1-\alpha)\left(\frac{\delta\rho_l}{\delta h}\right)_p$$

$$b_{22} = \frac{1}{A}$$

$$c_{24} = S_l'$$

$$c_{26} = -c_{16}$$

$$d_2 = -d_1' + d_2' \qquad \text{where}$$

$$d_2' = -S_{l_3}$$

MOMENTUM CONSERVATION FOR THE GAS PHASE

$$a_{31} = \frac{1}{A} + a_{31}' \qquad \text{where}$$

$$a_{31}' = K\,\frac{1}{\alpha A \rho_g}$$

$$a_{32} = -K\,\frac{1}{(1-\alpha)A\rho_l}$$

$$a_{33} = a_{33}' + a_{33}'' \qquad \text{where}$$

$$a_{33}' = -V_g\rho_g$$

$$a_{33}'' = -K\left(\frac{V_g}{\alpha} + \frac{V_l}{(1-\alpha)}\right)$$

$$a_{34} = a_{34}' + a_{34}'' \qquad \text{where}$$

$$a_{34}' = -V_g a_{14}$$

$$a_{34}'' = K\left(-\left(\frac{\delta\rho_g}{\delta p}\right)_h + \left(\frac{\delta\rho_g}{\delta h}\right)_p \left(\frac{\delta h_g}{\delta p}\right)_{sat}\right)\frac{V_g}{\rho_g} + \left(\left(\frac{\delta\rho_l}{\delta p}\right)_h + \left(\frac{\delta\rho_l}{\delta h}\right)_p \left(\frac{\delta h_l}{\delta p}\right)_{sat}\right)\frac{V_l}{\rho_l}$$

$$a_{35} = a_{35}' + a_{35}'' \qquad \text{where}$$

$$a_{35}' = -\alpha V_g \left(\frac{\delta\rho_g}{\delta h}\right)_p$$

$$a_{35}'' = -K \frac{V_g}{\rho_g} \left(\frac{\delta\rho_g}{\delta h}\right)_p$$

$$a_{36} = K \frac{V_l}{\rho_l} \left(\frac{\delta\rho_l}{\delta h}\right)_p$$

$$b_{31} = \frac{1}{A} V_g + b_{31}' \qquad \text{where}$$

$$b_{31}' = a_{31}' U_l$$

$$b_{32} = a_{32} U_g$$

$$b_{33} = a_{33}' V_g + b_{33}' \qquad \text{where}$$

$$b_{33}' = -K \left(\frac{V_g U_l}{\alpha} + \frac{V_l U_g}{(1-\alpha)}\right)$$

$$b_{34} = a_{34}' V_g + \alpha + b_{34}' \qquad \text{where}$$

$$b_{34}' = K\left(-\frac{V_g U_l}{\rho_g}\left(\left(\frac{\delta\rho_g}{\delta p}\right)_h + \left(\frac{\delta\rho_g}{\delta h}\right)_p \left(\frac{\delta h_g}{\delta p}\right)_{sat}\right) + \frac{V_l U_g}{\rho_l}\left(\left(\frac{\delta\rho_l}{\delta p}\right)_h + \left(\frac{\delta\rho_l}{\delta h}\right)_p \left(\frac{\delta h_g}{\delta p}\right)_{sat}\right)\right)$$

$$b_{35} = a_{35}' V_g + a_{35}'' U_l$$

$$b_{36} = a_{36} U_g$$

$$c_{31} = c_{31}' + c_{31}'' + \alpha c_{31}''' \text{ where}$$

$$c_{31}' = F_{wg}' - \frac{dA}{dx}\frac{V_g}{A^2}$$

$$c_{31}'' = (1-\alpha)\frac{F_{stat}''}{A\rho_g} - K\frac{dA}{dx}U_l\frac{1}{\alpha\rho_g A^2}$$

$$c_{31}''' = \frac{S_{sing}}{\Delta x}\frac{m_g}{2\bar{\rho}\cdot A^2}$$

$$c_{32} = c_{32}' + \alpha c_{32}'' \quad \text{where}$$

$$c_{32}' = -\alpha\frac{F_{stat}''}{A\rho_l} + K\frac{dA}{dx}U_g\frac{1}{(1-\alpha)\rho_l A^2}$$

$$c_{32}'' = \frac{S_{sing}}{\Delta x}\frac{(m_g+2m_g)}{2\bar{\rho}\,A^2}$$

$$c_{36} = c_{16}'(V_i - V_g) - c_{16}''V_g$$

$$d_3 = -d_1'V_g - \alpha\rho_g g\cos\theta$$

MOMENTUM CONSERVATION FOR THE LIQUID PHASE

$$a_{41} = -a_{31}'$$

$$a_{42} = \frac{1}{A} - a_{32}$$

$$a_{43} = a_{43}' - a_{33}'' \quad \text{where}$$

$$a_{43}' = \rho_l V_l$$

$$a_{44} = a_{44}' - a_{34}'' \quad \text{where}$$

$$a_{44}' = -V_l a_{24}$$

$$a_{45} = -a_{35}''$$

$$a_{46} = a_{46}' - a_{36} \qquad \text{where}$$

$$a_{46}' = -(1-\alpha)\ V_l \left(\frac{\delta \rho_l}{\delta h}\right)_p$$

$$b_{41} = -b_{31}'$$

$$b_{42} = \frac{1}{A} V_l - b_{32}$$

$$b_{32} = a_{43}'\ V_l - b_{33}'$$

$$b_{44} = a_{44}'\ V_l + (1-\alpha) - b_{34}'$$

$$b_{45} = -a_{35}''\ U_l$$

$$b_{46} = a_{46}'\ V_l - b_{36}$$

$$c_{41} = -c_{31}'' + (1-\alpha)\ c_{31}'''$$

$$c_{42} = c_{42}' - c_{32}' + (1-\alpha) c_{32}'' \qquad \text{where}$$

$$c_{42}' = F_{wl} - \frac{dA}{dx} \frac{V_l}{A^2}$$

$$c_{43} = -\rho_l\ g \cos\theta$$

$$c_{46} = -c_{16}'\ (V_i - V_g) + c_{16}''\ V_l$$

$$d_4 = d_l'\ V_l - \rho_l\ g \cos\theta$$

ENERGY CONSERVATION FOR THE GAS

$$a_{54} = \rho_g \left(\frac{\delta h_g}{\delta p}\right)_{sat} - 1$$

$$a_{55} = \rho_g$$

$$b_{54} = V_g \; a_{54}$$

$$b_{55} = V_g \; a_{55}$$

$$c_{55} = \frac{Q_{wg}"}{cp_g} + (1-\alpha) \; (Q_{ig}" + \Gamma_{woo})$$

$$c_{56} = (1-\alpha) \; (\Gamma_i" - \Gamma_w") \; \Delta h_g$$

$$d_5 = Q_{wg}" \; \Delta T_w$$

ENERGY CONSERVATION FOR THE LIQUID

$$a_{64} = \rho_l \left(\frac{\delta h_l}{\delta p}\right)_{sat} - 1$$

$$a_{66} = \rho_l$$

$$b_{64} = V_l \; a_{64}$$

$$b_{66} = V_l \; a_{66}$$

$$c_{65} = -\alpha Q_{ig}"$$

$$c_{66} = -\alpha[\Gamma_{woo} + (\Gamma_i"+\Gamma_w")(\Delta h_l - h_{lg})] + \frac{Q_{wl}"}{c_{pl}}$$

$$d_6 = Q_{wl} \; \Delta T_w + d_6' \qquad \text{where}$$

$$d_6' = -\alpha \; \Gamma_{woo} \; h_{lg}$$

APPENDIX C

PHYSICAL PROPERTIES OF NITROGEN IN THE GAS AND LIQUID PHASES

The two-fluid computer programme RISQUE-T is originally developed to model a one-dimensional two-phase flow in a water-steam flow.

In order to use the programme to simulate inverse annular film boiling and dispersed droplet flow using nitrogen as coolant, a new set of physical properties has been developed and these are given in the following description (all units are SI):

SATURATION TEMPERATURE $T_{sat}(p_{sat})$

$$T_{sat}(p_{sat}) = -304.494/(\log_{10}(p_{sat}/1.013\cdot10^5) - 3.93352)$$

where

$$0.25\cdot10^5[N/m^2] \leq p_{sat} \leq 10\cdot10^5[N/m^2]$$

This correlation is given in Landolt-Börnstein (1967).

LIQUID SATURATION ENTHALPHY $h_{lsat}(p_{sat})$

$$h_{lsat}(p_{sat}) = A_o + p_{sat}(A_1 + p_{sat}(A_2 + p_{sat}(A_3 + p_{sat}A_4)))$$

where

A_o = -1.448E+05

A_1 = 2.836E-01

A_2 = -6.076E-07

A_3 = 6.687E-13

A_4 = -2.661E-19

and this correlation is valid for

$10^5[N/m^2] \leq p_{sat} \leq 10 \cdot 10^5[N/m^2]$

The correlation is estimated by least-squares fit using data from Vargaftik (1975).

LATENT HEAT OF EVAPORATION $h_{lg}(p_{sat})$

$$h_{lg}(p_{sat}) = A_o + p_{sat}(A_1 + p_{sat}(A_2 + p_{sat}(A_3 + p_{sat}A_4)))$$

where

A_o = 2.112E+05

A_1 = -1.571E-01

A_2 = 3.004E-07

A_3 = -3.358E-13

A_4 = 1.350E-19

and

$10^5[N/m^2] \leq p_{sat} \leq 10 \cdot 10^5[N/m^2]$

The coefficients are estimated by least-squares fit using data from Vargaftik (1975).

SPECIFIC HEAT CAPACITY OF GAS AT CONSTANT PRESSURE $c_{pg}(h_g,p)$

$$c_{pg}(h_g,p) = A_o + h_g(A_1 + h_g(A_2 + h_g A_3))$$

where

A_o = (1.409+p(4.496E-06+p(-1.591E-11+p1.750E-17)))·E+03

A_1 = -7.754E-3 + p(-6.390E-08 + p(2.702E-13-p3.043E-19))

A_2 = (5.170E-05+P(2.594E-10+P(-1.343E-15+p1.569E-21)))·E-03

A_3 = (-1.092E-07+p(-2.520E-13+p(1.891E-18-p2.348E-24)))E-06

This correlation is defined in the following intervals

$h_{gsat}[J/kg] \leq h_g \leq 1.7 \cdot 10^5 [J/kg]$ and

$10^5 [N/m^2] \leq p \leq 6 \cdot 10^5 [N/m^2]$

The coefficients are calculated by a two-step technique using least-squares fit.

First a set of coefficients A_{ip}, i= 0,1,2,3 and p = 1,2,3,4,5 and $6 \cdot 10^5 [N/m^2]$ are found, and secondly expressions of the form $A_i = A_i(p)$, i = 0,1,2,3 are found. The data used are from Vargaftik (1975).

SPECIFIC HEAT CAPACITY OF LIQUID AT CONSTANT PRESSURE $c_{pl}(h_l)$

$c_{pl}(h_l) = A_o + h_l(A_1 + h_l(A_2 + h_l(A_3 + h_l A_4)))$

where A_o = 4.975E+03

A_1 = 7.796E-02

A_2 = 7.368E-07

A_3 = 3.426E-12

A_4 = 5.830E-18

and $-1.4 \cdot 10^5 [J/kg] \leq h_l \leq -0.65 \cdot 10^5 [J/kg]$

As the dependence on pressure is negligible, $c_{pl}(h_l) = c_{pl}(h_l,p)$
The data used are from Vargaftik.

GAS DENSITY $\rho_g\ (h_g,p)$

$$\rho_g(h_g,p) = 1/(A_1+A_2p+A_3/p+h_g(B_1+B_2p+B_3/p))$$

where

$A_1 = -8.668022E-04$

$A_2 = -9.0406019E-10$

$A_3 = -5.7967079$

$B_1 = 7.9632344E-09$

$B_2 = -3.5034356E-15$

$B_3 = 0.28550768$

This expression is defined for

$$h_{gsat}[J/kg] \leq h_g \leq 3.6 \cdot 10^5 [J/kg] \quad \text{and}$$

$$10^5[N/m^2] \leq p \leq 10 \cdot 10^5 [N/m^2]$$

The correlation is estimated by using a similar expression for steam developed at Brookhaven National Laboratory (1976). The coefficients for the case of steam are replaced by new coefficients for nitrogen gas.

LIQUID DENSITY $\rho_l(h_l)$

$$\rho_l(h_l) = A_o + h_l(A_1+h_l(A_2+h_l(A_3+h_lA_4)))$$

where

A_0 = 5.027E+02

A_1 = -1.929E-03

A_2 = 1.548E-08

A_3 = 1.185E-13

A_4 = 2.538E-19

and $-1.4 \cdot 10^5 [J/kg] \leq h_l \leq -0.65 \cdot 10^5 [J/kg]$.
$\rho_l(h_l) = \rho_l(h_l, p)$ because the influence of pressure is negligible.

The correlation is fitted to data from Vargaftik (1975).

PARTICAL DERIVATIVE OF GAS DENSITY WITH RESPECT TO PRESSURE $\left(\frac{\delta \rho g}{\delta p}\right)_{h_g}$

Taking the derivative of $\rho_g(h_g, p)$ with respect to pressure the result is

$$\left(\frac{\delta \rho g}{\delta p}\right)_{hg} = - \rho_g(h_g,p)^2 (A_2 - A_3/p^2 + h_g(B_2 - B_3/p^2))$$

where

A_2 = -9.0406019E-10

A_3 = -5.7967079

B_2 = -3.5034356E-15

B_3 = 0.28550768

PARTIAL DERIVATIVE OF GAS DENSITY WITH RESPECT TO ENTHALPHY $\left(\frac{\delta \rho g}{\delta hg}\right)_p$

The result becomes

$$\left(\frac{\delta \rho g}{\delta hg}\right)_p = -\rho_g(h_g, p)^2 (B1+B2+B3/p)$$

where

B1 = 7.9632344E-09

B2 = -3.5034356E-15

B3 = 0.28550768

PARTIAL DERIVATIVE OF LIQUID DENSITY WITH RESPECT TO PRESSURE $\left(\frac{\delta \rho l}{\delta p}\right)_{h_l}$

When $\rho_l(h_l, p) = \rho_l(h_l)$ then

$$\left(\frac{\delta \rho l}{\delta p}\right)_{h_l} = 0.0$$

PARTIAL DERIVATIVE OF LIQUID DENSITY WITH RESPECT TO ENTHALPHY $\left(\frac{\delta \rho l}{\delta h_l}\right)_\rho$

$$\left(\frac{\delta \rho l}{\delta h_l}\right)_\rho = A_1 + 2A_2 h_l + 3A_3 h_l^2 + 4A_4 h_l^3$$

where

A_1 = -1.929E-03

A_2 = 1.548E-08

A_3 = 1.185E-13

A_4 = 2.538E-19

DERIVATIVE OF GAS SATURATION ENTHALPHY WITH RESPECT TO PRESSURE $\left(\frac{dhg}{dp}\right)_{sat}$, AND DERIVATIVE OF LIQUID SATURATION ENTHALPHY WITH RESPECT TO PRESSURE $\left(\frac{dhl}{dp}\right)_{sat}$.

The gas saturation enthalpy is defined as follows

$$h_{g_{sat}}\left(P_{sat}\right) = h_{l_{sat}}\left(P_{sat}\right) + h_{lg}\left(P_{sat}\right).$$

Thus,
$$\left(\frac{dh_g}{dp}\right)_{sat} = \left(\frac{dh_l}{dp}\right)_{sat} + \left(\frac{dh_{lg}}{dp}\right)_{sat},$$

where
$$\left(\frac{dh_l}{dp}\right)_{sat} = A_1 + 2A_2P_{sat} + 3A_3P_{sat}^2 + 4A_4P_{sat}^3$$

$A_1 = 2.836E-01$

$A_2 = -6.076E-07$

$A_3 = 6.687E-13$

$A_4 = -2.661E-19$

and $\left(\frac{dh_{lg}}{dp}\right)_{sat} = B_1 + 2B_2P_{sat} + 3B_3P_{sat}^2 + 4B_4P_{sat}^3$

$B_1 = -1.571E-01$

$B_2 = 3.004E-07$

$B_3 = -3.358E-13$

$B_4 = 1.350E-19.$

THERMAL CONDUCTIVITY OF GAS $k_g(h_g,p)$

Due to lack of data this property is estimated only at

$$k_g(h_g, p = 10^5\ N/m^2) = A_o + h_g\ (A_1 + h_g(A_2 + h_g(A_3 + h_g\ A_4))),$$

where

A_o = 2.688E-03

A_1 = 3.722E-08

A_2 = 4.114E-13

A_3 = -1.445E-18

A_4 = 1.644E-24

and $h_{gsat} \leq h_g \leq 3.6 \cdot 10^5$ [J/kg].

The correlation is a least-squares fit to data from the Handbook of Chemistry and Physics, p. E-3 (1976-1977).

THERMAL CONDUCTIVITY OF LIQUID $k_l(h_l)$

Suppose the influence of pressure is negligible; then,

$$k_l(h_l) = A_o + h_l\ (A_1 + h_l(A_2 + h_l\ A_3)),$$

where

A_o = 5.523E-02

A_1 = -2.469E-07

A_2 = 4.988E-12

A_3 = 1.190E-17

$-1.4 \cdot 10^5 [J/kg] \leq h_l \leq -0.65 \cdot 10^5 [J/kg]$.

and it is a least-squares fit to data from Handbook of Chemistry and Physics (1976-1977).

DYNAMIC VISCOSITY OF GAS $\mu_g (h_g, p)$

$$\mu_g (h_g, p) = A_o + h_g (A_1 + h_g (A_2 + h_g(A_3 + h_g A_4)))$$

where

A_o = 6.403E-12p+5.457E-07

A_1 = -7.684E-17p+4.666E-11

A_2 = 3.486E-22p+2.557E-16

A_3 = -5.700E-28p-1.389E-21

A_4 = 7.333E-35p+2.188E-27

and $h_{gsat} \leq h_g \leq 2.5 \cdot 10^5 [J/kg]$

$10^5 [N/m^2] \leq p \leq 10 \cdot 10^5 [N/m^2]$

and the data used is from Vargaftik.

SURFACE TENSION $\sigma(h_l)$

$$\sigma(h_l) = A_o + h_l (A_1 + h_l (A_2 + h_l A_3))$$

where

A_o = -8.295E-04

A_1 = -4.373E-08

A_2 = 3.300E-13

$A_3 = 2.371E-19$

and

$$-1.4 \cdot 10^5 [J/kg] \leq h_l \leq -0.9 \cdot 10^5 [J/kg]$$

and the data used for fitting is from Vargaftik (1975).

DYNAMIC VISCOSITY OF LIQUID $\mu_l(h_l)$

Supposing no dependence on pressure then one gets

$$\mu_l(h_l) = A_0 + h_l(A_1 + h_l(A_2 + h_l(A_3 + h_l A_4)))$$

where

$A_o = 1.731E-04$

$A_1 = 3.633E-09$

$A_2 = 4.211E-14$

$A_3 = 2.300E-19$

$A_4 = 1.003E-24$

and $-1.4 \cdot 10^5 [J/kg] \leq h_l \leq -0.65 \cdot 10^5 [J/kg]$

The data used for fitting is from Vargaftik (1975).

ANALYTICAL FITS COMPARED WITH TABLE VALUES

The approximations (analytical fits) have been compared with the experimental data (table values from the references) in the following 11 figures which give an impression of the accuracy:

Fig. 1	$T_{sat}(p_{sat})$
Fig. 2	$h_{\ell sat}(p_{sat})$
Fig. 3	$h_{\ell g}(p_{sat})$
Fig. 4	$c_{pg}(h_g,p)$
Fig. 5	$c_{p\ell}(h_\ell,p)$
Fig. 6	$\rho_g(h_g,p)$
Fig. 7	$\rho_\ell(h_\ell)$
Fig. 8	$k_g(h_g,p)$
Fig. 9	$k_\ell(h_\ell)$
Fig. 10	$\mu_g(h_g,p)$
Fig. 11	$\mu_\ell(h_\ell)$

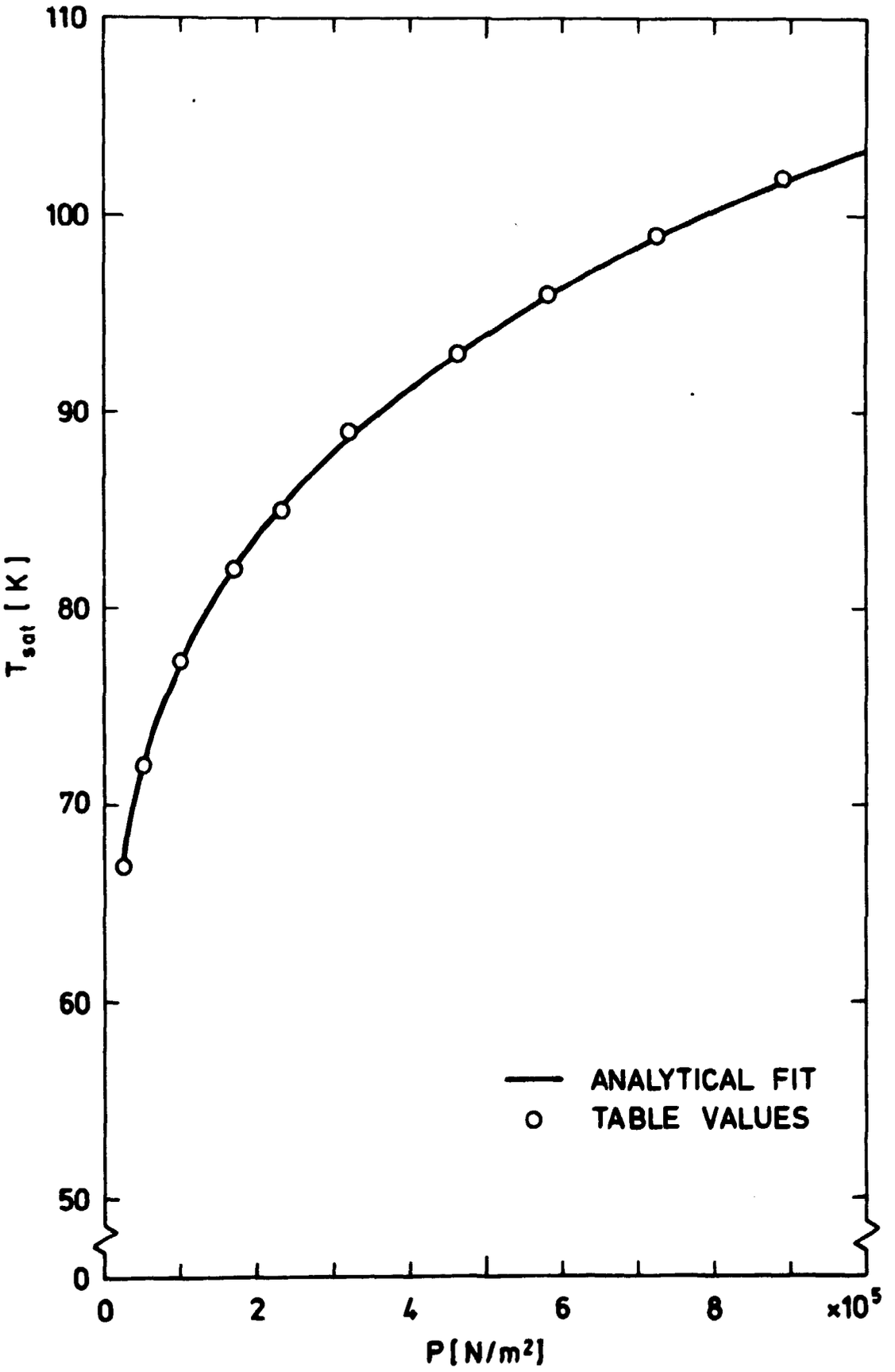

Fig. 1: N_2 saturation temperature T_{sat} versus pressure P_{sat}

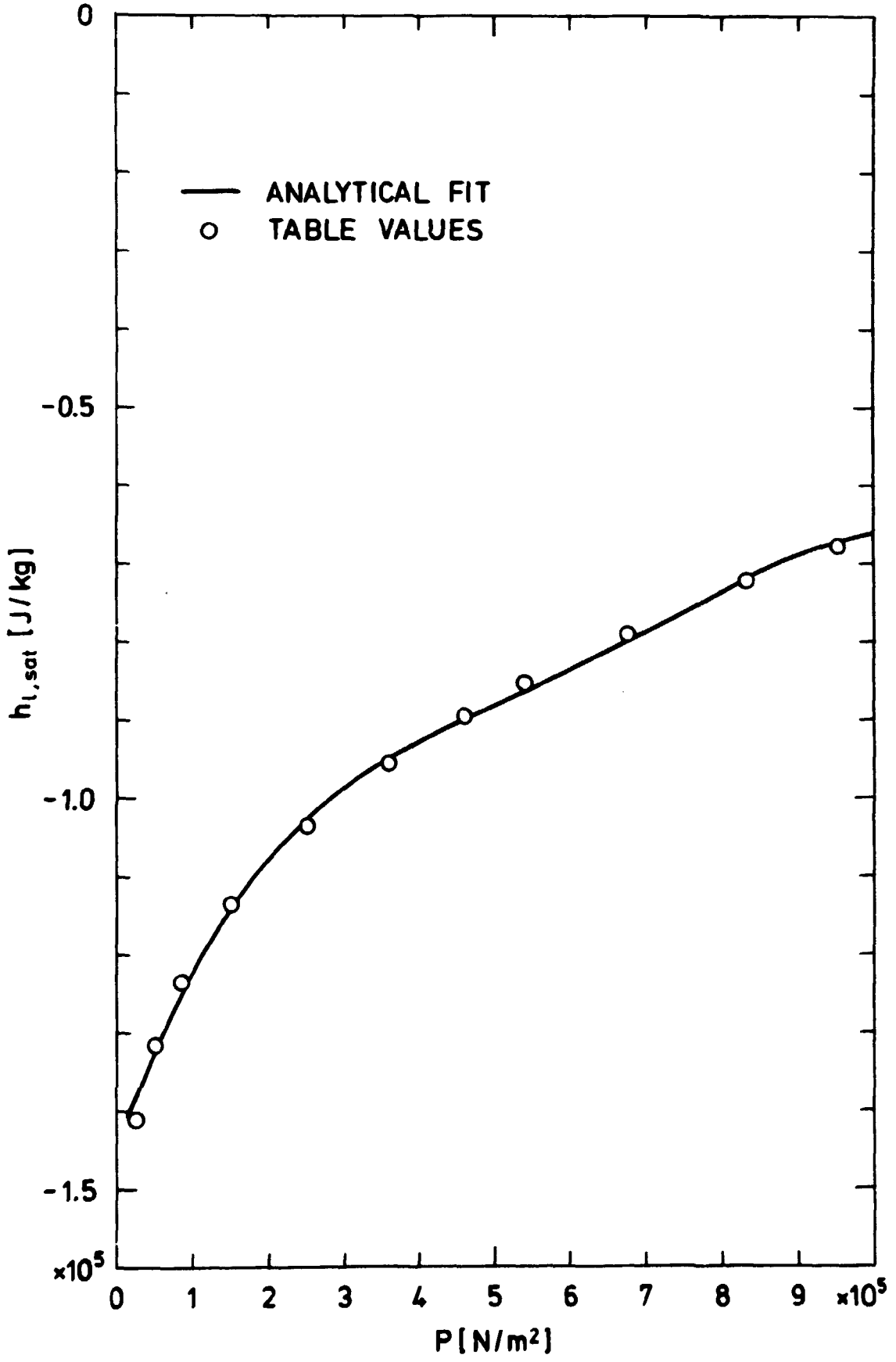

Fig. 2 : N_2 liquid entalphy $h_{\ell\,sat}$ versus pressure P_{sat}

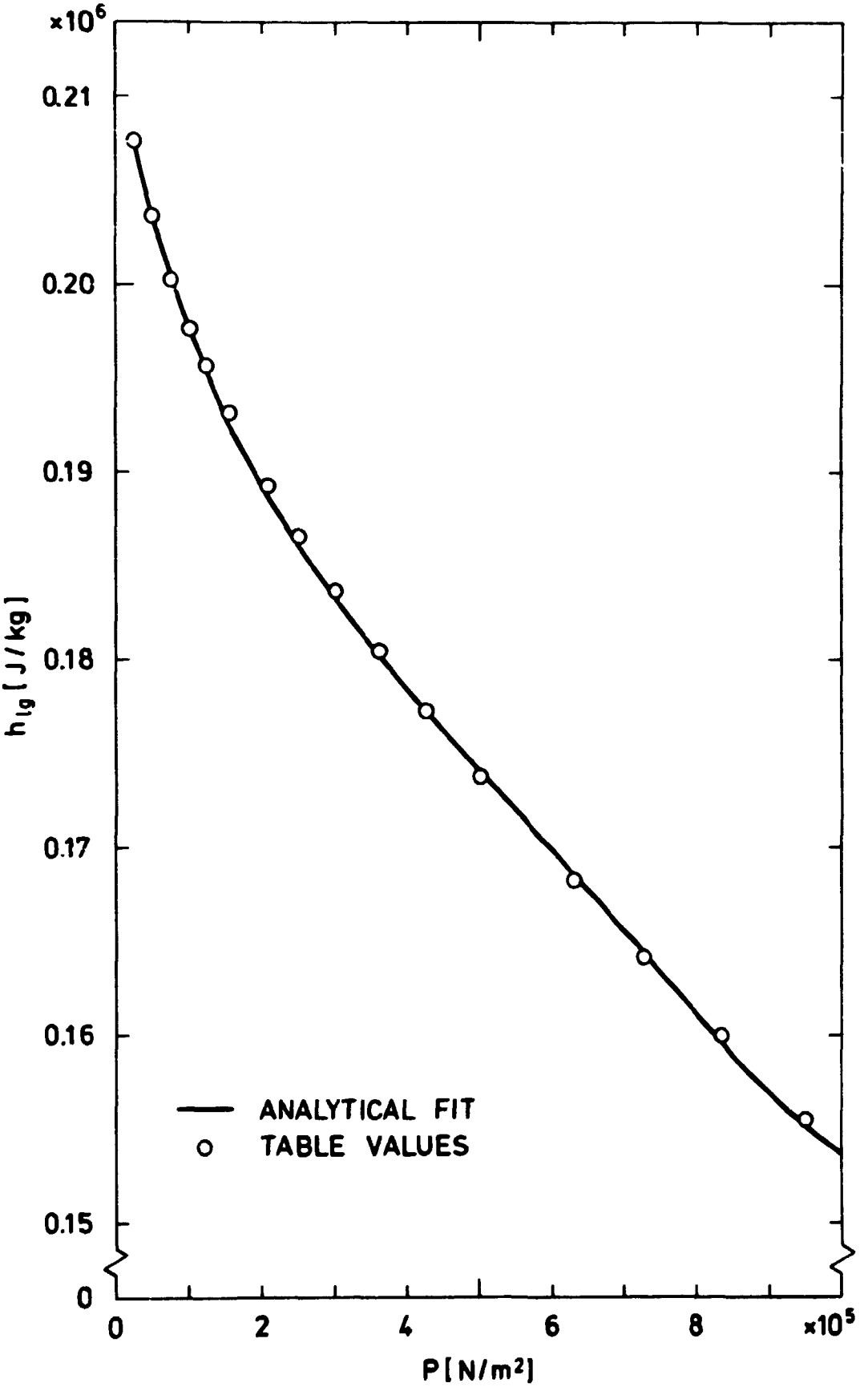

Fig 3: N_2 heat of evaporation h_{lg} versus pressure P_{sat}

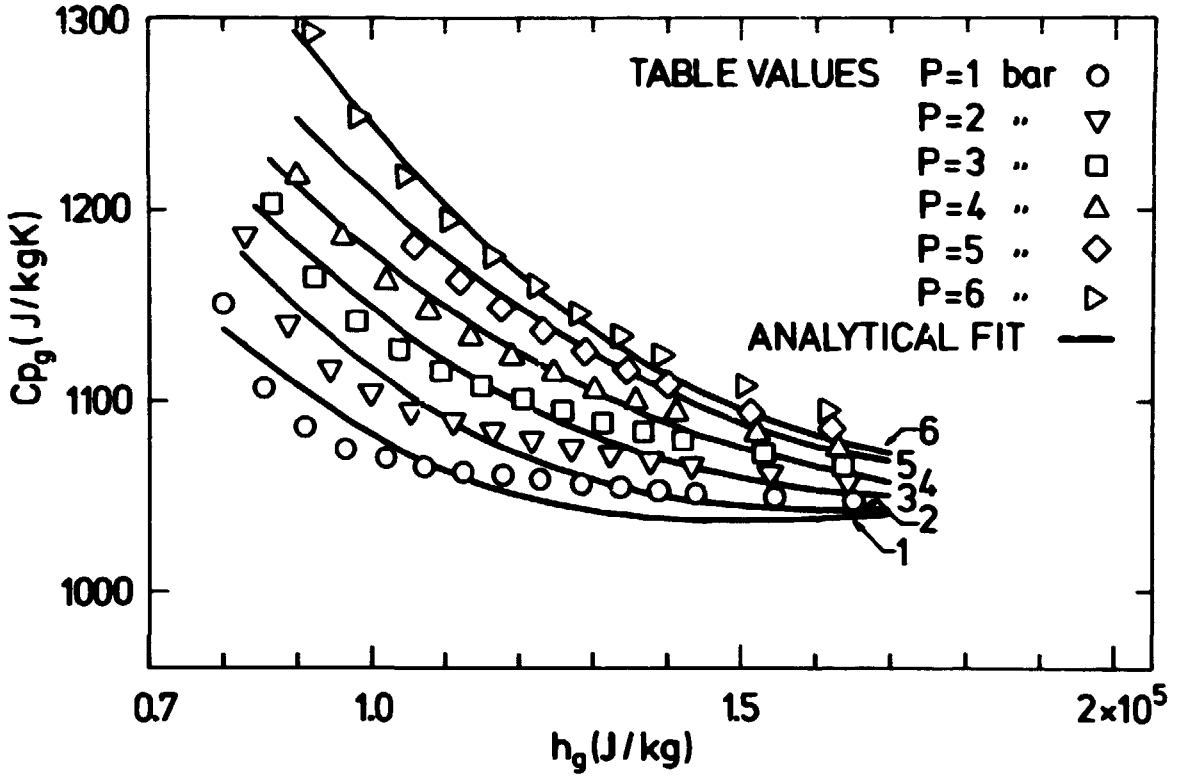

Fig. 4: N_2 gas heat capacity c_{pg} versus entalphy h_g and pressure P.

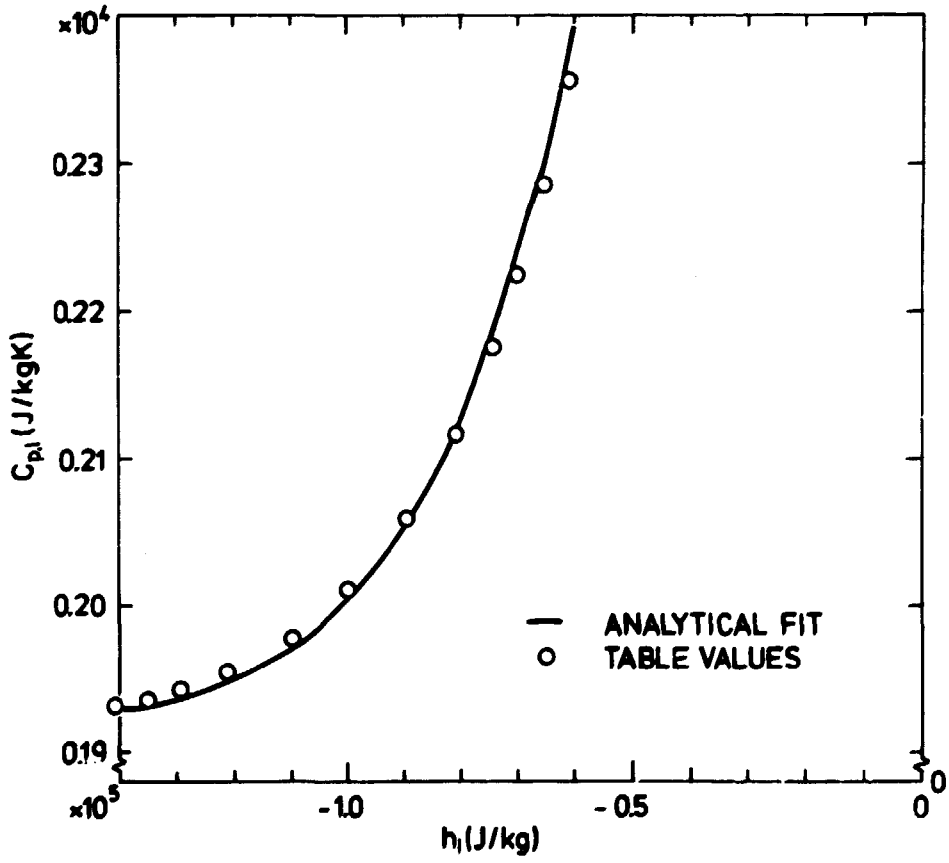

Fig. 5: N_2 liquid heat capacity $c_{p\ell}$ versus entalphy h_ℓ.

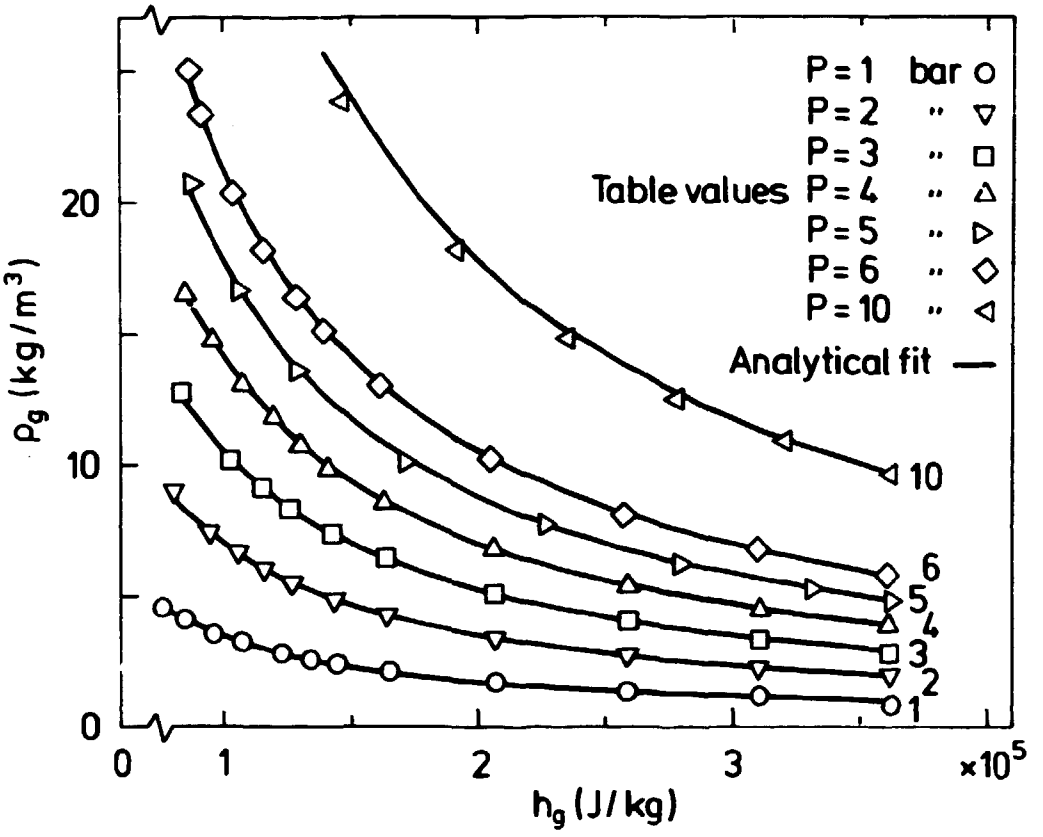

Fig.6 : N_2 gas density ρ_g versus entalphy h_g and pressure P.

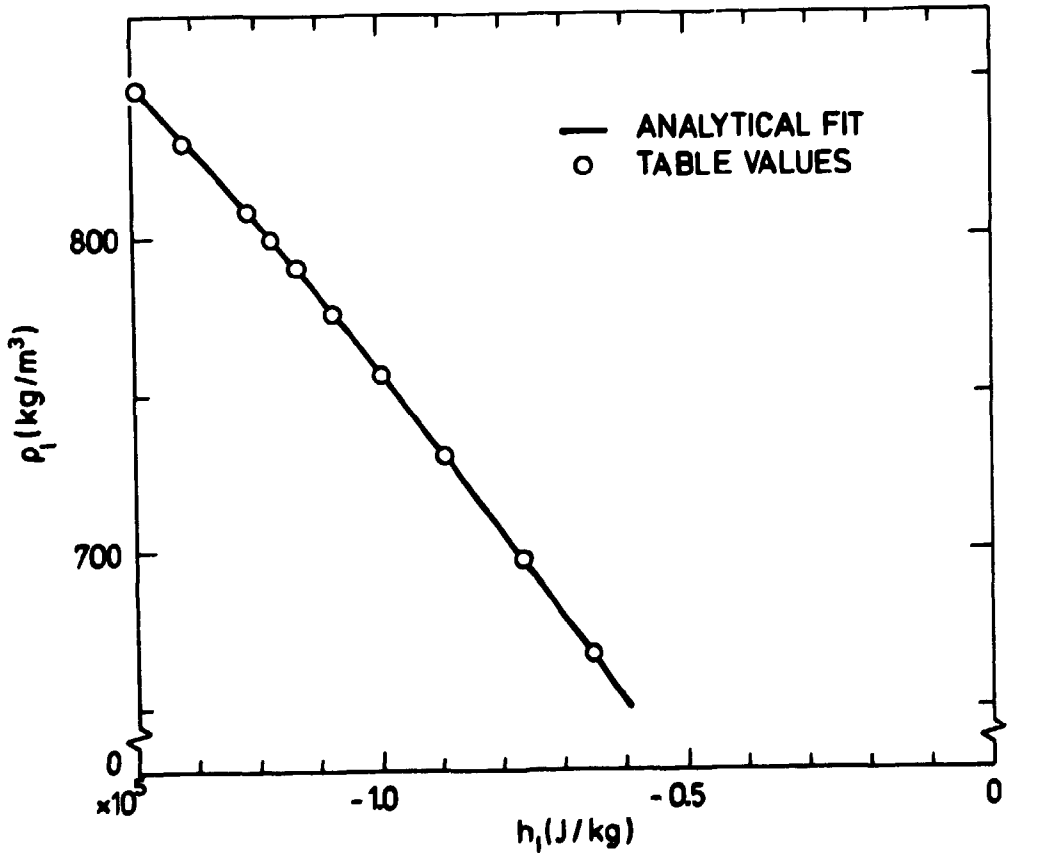

Fig. 7: N_2 liquid density ρ_ℓ versus entalphy h_ℓ.

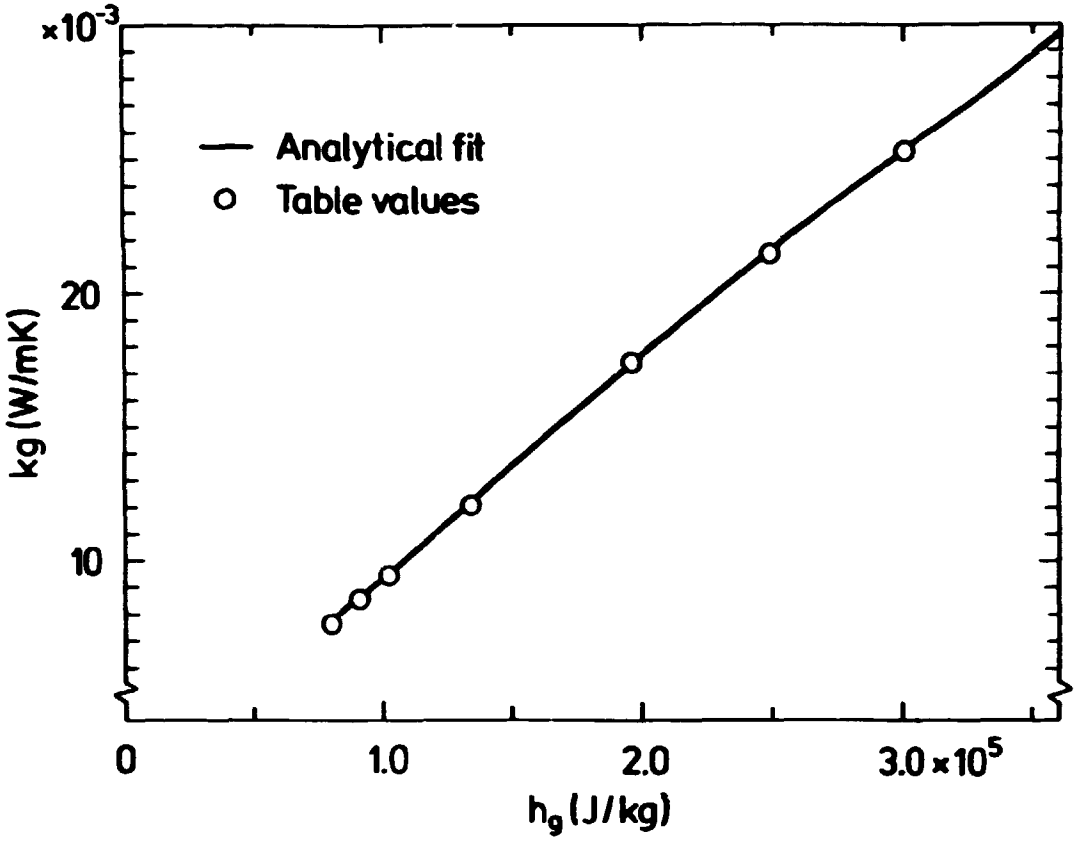

Fig. 8 : N_2 gas conductivity k_g versus entalphy h_g.

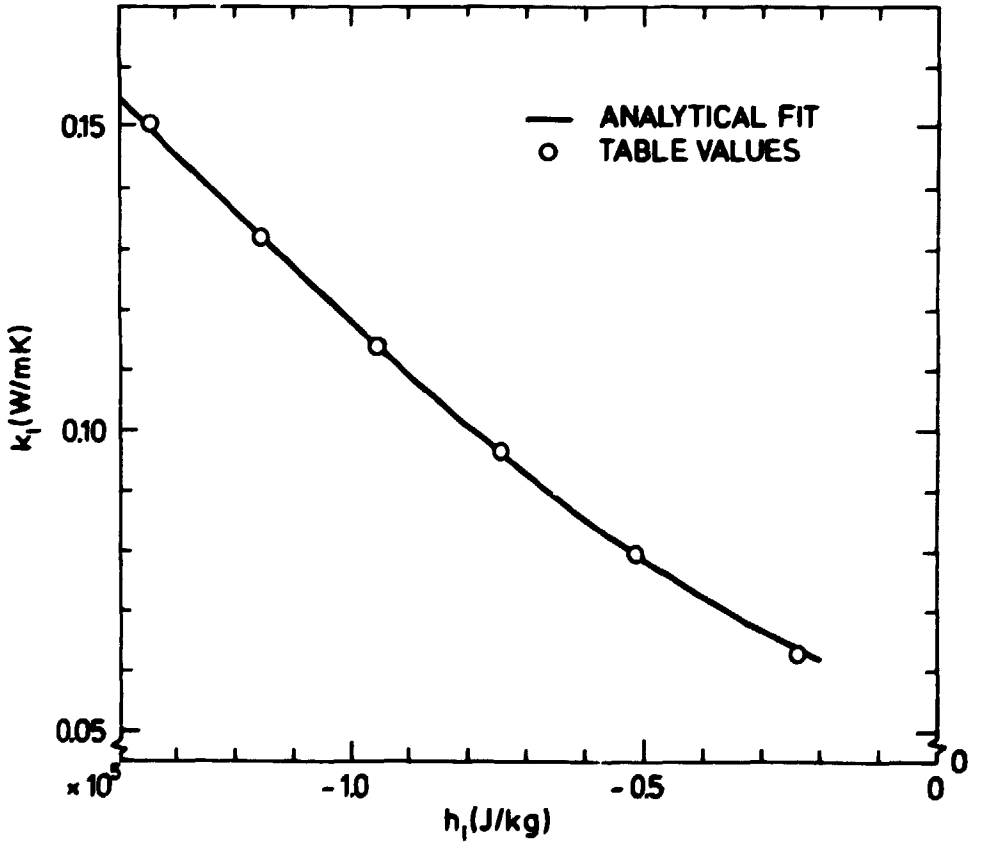

Fig. 9: N_2 liquid conductivity k_ℓ versus entalphy h_ℓ.

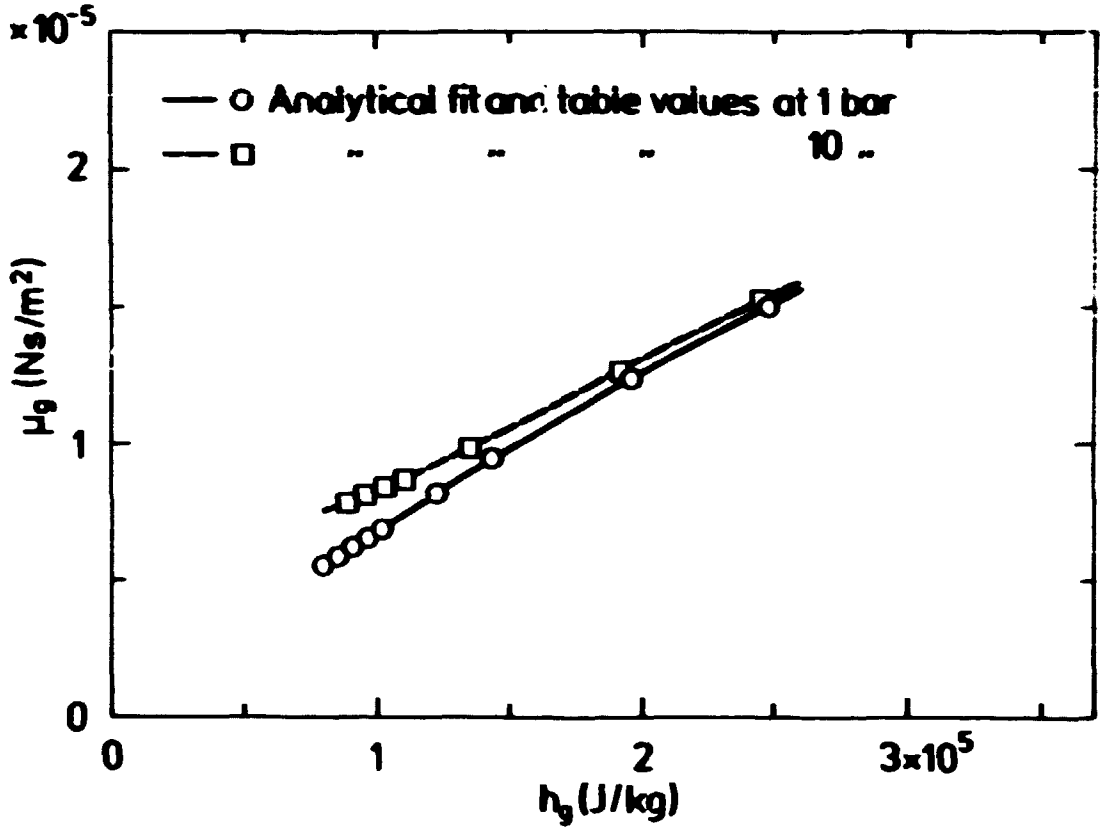

Fig. 10: N_2 gas dynamic viscosity μ_g versus entalphy h_g and pressure P.

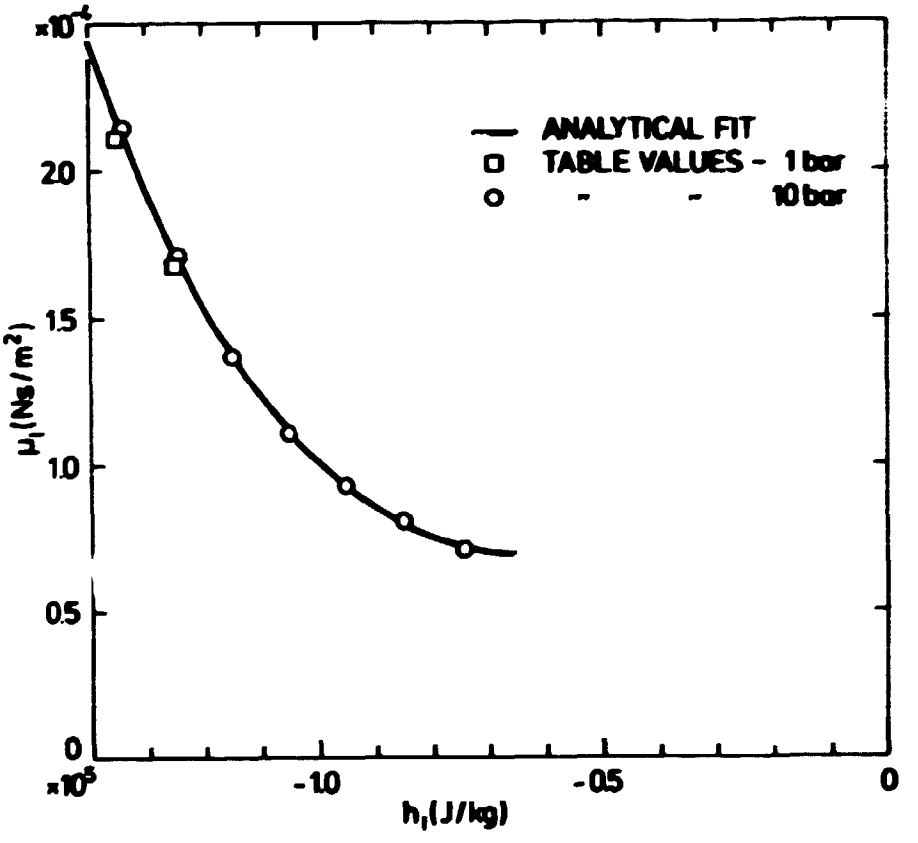

Fig. 11: N_2 liquid dynamic viscosity u_l versus entalphy h_l.

APPENDIX D

EXPERIMENTAL DATA

Inverse annular film boiling in liquid nitrogen flow

Measurements of void fraction

Table	Run	Subcooling	Level of void detectors above inlet		Mass flux
No.	No.	$\Delta\bar{t}_{sub}$ s	H_1	H_2	G
		[°C] [°C]	[mm]	[mm]	[kg/m^{2}s]
1	1- 24	0.2 ± 0.4	45	310	9.6-236.6
	25- 30		50	315	9.2-117.5
	31- 41		60	230	9.4-110.3
	42- 55		100	600	8.2-237.1
	56- 63		160	470	9.4-167.6
2	64- 74	4.2 ± 0.4	60	230	11.1-101.4
	75- 80		100	600	13.6- 95.4
	81- 89		160	470	8.6- 72.6
3	90-101	5.9 ± 0.6	45	310	9.7- 91.2
	102-110		60	230	11.0- 64.8
	111-123		100	600	13.4- 69.1
	124-131		160	470	10.8- 67.6

MEASUREMENTS OF HEAT TRANSFER

Table	Run	Subcooling		Mass flux	Wall temperature	
No.	No.	$\overline{\Delta t_{sub}}$	s	G	$\overline{t_w}$	s
		[°C]	[°C]	[kg/m²s]	[°C]	[°C]
4	301-322	-0.4	± 0.2	12.6-135.7	-2.1	± 2.9
5	323-332	5.0	± 0.6	11.4- 61.6	-1.3	± 2.5
6	333-344	6.5	± 0.5	10.8- 73.7	-2.4	± 3.9
7	345-358	8.9	± 0.7	8.8- 75.4	-2.1	± 4.7

Run	Level above inlet	Sub-cooling	N_2-liquid inlet flow	Quality		Void fraction		Mass-flux	Heat-flux	Wall temp.
		Δt_{sub}	$\dot{m}$	x	s	α	s	G	q^*	t_w
	mm	°C	g/s	%	%	%	%	kg/m^2s	W/cm^2	°C
1	0	-0.1	1.4	0.1	1.6			9.6	1.07	-4.1
	45					66.5	1.0			
	310					99.1	1.7			
	740			122.5	9.1					
2	0	0.2	1.9	-0.1	0.5			13.0	1.00	-2.6
	45					69.6	1.3			
	310					97.3	2.1			
	740			85.2	2.7					
3	0	0.4	2.2	-0.4	1.8			15.3	1.14	3.1
	45					59.1	1.6			
	310					95.5	1.0			
	740			81.8	8.7					
4	0	0.5	2.4	-0.4	1.0			16.1	1.18	1.7
	45					66.7	1.2			
	310					92.6	2.0			
	740			80.4	4.2					
5	0	1.0	2.8	-0.9	3.5			18.9	1.22	-1.0
	45					61.0	1.8			
	310					93.4	1.7			
	740			69.9	4.5					
6	0	0.0	2.9	0.0	0.6			20.1	1.09	-4.6
	45					66.9	0.9			
	310					97.1	1.4			
	740			59.8	2.2					
7	0	0.6	3.6	-0.5	1.3			24.4	1.27	-2.4
	45					59.4	1.6			
	310					92.5	2.0			
	740			56.8	2.2					
8	0	0.5	3.6	-0.5	1.1			24.5	1.33	-0.3
	45					57.6	1.3			
	310					93.3	2.1			
	740			59.3	1.6					
9	0	0.5	3.7	-0.5	0.7			25.2	1.35	-0.7
	45					56.0	1.1			
	310					92.7	1.7			
	740			58.4	1.1					
10	0	0.4	4.2	-0.3	0.4			28.9	1.36	-0.9
	45					55.9	1.3			
	310					92.7	1.0			
	740			51.3	2.8					
11	0	-0.1	6.3	0.0	0.4			43.0	1.46	-5.4
	45					55.0	2.7			
	310					91.9	1.7			
	740			37.3	0.6					
12	0	0.3	6.6	-0.2	0.2			45.6	1.49	-6.0
	45					52.6	1.7			
	310					93.8	1.6			
	740			35.8	0.4					
13	0	1.0	6.9	-0.4	0.1			47.6	1.47	-5.5
	45					55.0	2.0			
	310					92.5	1.7			
	740			33.5	0.4					

Run	Level above inlet	Sub-cooling	N_2-liquid inlet flow	Quality		Void fraction		Mass-flux	Heat-flux	Wall temp.
		Δt_{sub}	$\dot{m}$	x	s	α	s	G	$q^{"}$	t_w
	mm	°C	g/s	%	%	%	%	kg/m²s	W/cm²	°C
14	0	1.0	9.1	-0.9	1.3			62.5	1.54	-8.0
	45					54.3	1.3			
	310					90.3	1.9			
	740			26.3	1.1					
15	0	0.4	11.8	0.3	0.1			81.2	1.71	-7.7
	45					42.5	1.7			
	310					88.8	1.3			
	740			22.8	0.3					
16	0	0.3	11.9	-0.2	0.4			81.5	1.63	-7.3
	45					58.4	1.5			
	310					88.7	0.8			
	740			21.8	0.8					
17	0	0.5	12.6	-0.4	0.3			86.6	1.70	-7.6
	45					41.4	1.7			
	310					89.9	1.1			
	740			21.2	0.6					
18	0	0.7	13.9	-0.6	0.2			95.4	1.67	-7.1
	45					43.2				
	310					88.5				
	740			18.7	0.7					
19	0	0.4	13.9	-0.3	0.2			95.6	1.73	-11.0
	45					53.0	1.4			
	310					90.6	0.6			
	740			19.6	0.2					
20	0	0.1	14.9	-0.1	0.1			101.7	1.72	-10.6
	45					44.8	2.5			
	310					89.6	1.9			
	740			18.5	0.6					
21	0	0.9	18.5	-0.8	0.1			127.6	1.86	-6.9
	45					48.4	0.9			
	310					89.2	1.8			
	740			15.2	0.3					
22	0	-0.2	20.9	0.1	0.7			143.5		
	45					43.3	1.1			
	310					89.9	0.7			
	740									
23	0	0.1	24.8	0.0	0.6			170.3	2.06	-12.8
	45					38.8	1.1			
	310					82.1	1.4			
	740			13.2	0.7					
24	0	0.7	34.4	-0.8	0.1			236.6	2.19	-12.6
	45					34.5	1.2			
	310					79.7	2.0			
	740			9.4	0.1					
25	0	0.0	1.3	0.0	1.0			9.2	1.05	5.0
	50					68.5	1.6			
	315					98.6	2.1			
	740			125.4	4.0					
26	0	-0.3	5.6	0.2	0.5			38.6	1.44	-2.8
	50					64.7	1.4			
	315					92.7	1.2			
	740			41.4	0.7					

Run	Level above inlet	Sub-cooling	N_2-liquid inlet flow	Quality		Void fraction		Mass-flux	Heat-flux	Wall temp.
		Δt_{sub}	$\dot{m}$	x	s	α	s	G	q^*	t_w
	mm	°C	g/s	%	%	%	%	kg/m^2s	W/cm^2	°C
27	0	0.3	6.3	-0.3	0.9			43.5	1.48	-3.2
	50					63.1	0.9			
	315					92.7	0.7			
	740			37.3	0.9					
28	0	0.2	7.3	-0.1	0.4			50.2	1.58	-5.3
	50					63.1	1.1			
	315					93.3	1.4			
	740			34.4	0.4					
29	0	0.4	7.5	-0.3	1.5			51.6	1.77	-2.0
	50					61.0	1.6			
	315					93.0	1.3			
	740			33.3	1.4					
30	0	0.4	17.1	-0.3	0.2			117.5	1.86	-10.8
	50					50.1	1.1			
	315					90.0	1.1			
	740			17.1	0.2					
31	0	0.3	1.4	-0.3	1.1			9.4	1.05	2.3
	60					66.4	1.5			
	230					96.4	1.4			
	740			122.0	7.0					
32	0	0.2	1.4	-0.2	1.0			9.5	1.05	3.1
	60					65.2	2.2			
	230					95.5	1.6			
	740			120.6	5.7					
33	0	0.4	2.2	-0.3	0.7			14.9	1.16	0.5
	60					62.7	1.9			
	230					93.5	1.8			
	740			85.6	1.3					
34	0	0.3	2.4	-0.3	1.1			16.2	1.20	-0.8
	60					62.4	2.1			
	230					95.5	2.1			
	740			81.3	2.0					
35	0	0.3	3.2	-0.2	1.1			21.8	1.27	-2.3
	60					61.4	1.1			
	230					95.5	1.6			
	740			64.1	2.0					
36	0	0.5	5.0	-0.4	1.5			34.4	1.36	-3.9
	60					59.6	2.1			
	230					92.1	1.6			
	740			43.1	1.6					
37	0	0.2	6.2	-0.2	0.6			42.6	1.48	0.3
	60					59.3	1.1			
	230					92.2	1.0			
	740			38.1	0.7					
38	0	0.4	8.5	-0.3	0.1			58.7	1.62	-4.0
	60					59.6	2.2			
	230					88.8	0.9			
	740			30.0	0.3					
39	0	0.3	10.5	-0.3	0.4			72.5	1.66	-6.6
	60					55.4	1.1			
	230					88.5	1.2			
	740			25.0	0.5					

Run	Level above inlet	Sub-cooling	H_2-liquid inlet flow	Quality		Void fraction		Mass-flux	Heat-flux	Wall temp.
		Δt_{sub}	$\dot{m}$	x	s	α	s	G	q"	t_w
	mm	°C	g/s	%	%	%	%	kg/m²s	W/cm²	°C
40	0	0.2	11.7	-0.1	0.4			80.8	1.72	-7.9
	60					55.4	1.3			
	230					89.1	0.9			
	740			23.2	0.4					
41	0	0.3	16.0	-0.2	0.2			110.3	1.82	-10.0
	60					53.7	1.6			
	230					86.2	1.1			
	740			17.9	0.2					
42	0	-0.2	1.2	0.2	0.8			8.2	1.00	3.3
	100					80.4	1.7			
	600					99.5	1.4			
	740			133.7	4.2					
43	0	-1.2	1.4	1.1	2.5			9.5	1.03	2.3
	100					80.2	1.0			
	600					99.3	1.1			
	740			120.4	2.9					
44	0	0.8	2.6	-0.7	4.4			18.0	1.21	3.0
	100					78.6	1.1			
	600					100.0	0.6			
	740			73.3	5.2					
45	0	0.6	3.3	-0.5	2.5			22.8	1.23	2.5
	100					76.8	1.1			
	600					99.8	1.6			
	740			58.8	2.2					
46	0	0.1	4.5	-0.3	2.9			30.7	1.32	0.4
	100					76.0	1.5			
	600					100.0	1.1			
	740			47.4	2.2					
47	0	1.1	6.1	-1.0	0.8			41.7	1.42	-2.0
	100					77.3	1.4			
	600					97.9	1.5			
	740			36.5	1.6					
48	0	0.7	7.9	-0.6	1.3			54.2	1.47	0.0
	100					77.4	1.3			
	600					96.7	1.5			
	740			29.1	2.3					
49	0	1.1	9.0	-1.0	1.1			61.8	1.58	-4.8
	100					72.0	1.3			
	600					99.4	1.1			
	740			27.1	1.1					
50	0	1.0	12.7	-1.0	0.2			87.4	1.81	-5.7
	100					70.4	1.6			
	600					96.6	1.4			
	740			21.8	0.9					
51	0	0.7	16.5	-0.6	0.1			113.3	1.67	-6.8
	100					68.6	1.7			
	600					99.3	1.1			
	740			15.5	0.6					
52	0	0.7	20.5	-0.7	1.1			140.9	1.86	-7.2
	100					66.7	2.4			
	600					97.1	2.0			
	740			13.9	1.0					

Run	Level above inlet	Sub-cooling	H_2-liquid inlet flow	Quality		Void fraction		Mass-flux	Heat-flux	Wall temp.
		Δt_{sub}	$\dot{m}$	x	s	α	s	G	q^*	t_w
	mm	°C	g/s	%	%	%	%	kg/m^2s	W/cm^2	°C
53	0	-0.6	24.6	0.5	1.2			169.6	1.85	-10.6
	100					63.2	1.4			
	600					99.1	1.8			
	740			12.6	1.0					
54	0	-0.1	26.2	0.1	1.2			180.0	1.76	-9.4
	100					61.0	1.3			
	600					99.1	1.8			
	740			10.9	1.0					
55	0	-0.1	34.5	0.0	0.4			237.1	2.18	-13.1
	100					57.3	1.4			
	600					94.4	1.1			
	740			10.2	0.4					
56	0	0.1	1.4	0.0	2.2			9.4	1.08	1.0
	160					84.8	1.9			
	470					99.1	1.5			
	740			125.5	4.1					
57	0	-0.5	4.8	0.4	0.3			32.9	1.35	-1.4
	160					80.9	0.8			
	470					93.6	1.6			
	740			45.5	2.1					
58	0		4.9					33.9		
	160					81.0	1.5			
	470					98.4	1.8			
	740									
59	0	-0.2	7.7	0.2	0.4			52.8	1.55	-7.9
	160					78.5	1.9			
	470					96.9	1.5			
	740			32.5	0.5					
60	0	-0.2	8.7	0.2	0.3			60.0	1.60	-6.4
	160					77.7	1.2			
	470					92.6	1.9			
	740			29.7	0.6					
61	0	-0.9	13.0	0.8	0.3			89.4	1.69	-8.5
	160					75.5	0.6			
	470					92.2	1.8			
	740			21.7	0.4					
62	0	-0.1	13.3	0.0	0.1			91.6	1.74	-11.9
	160					77.7	1.8			
	470					98.9	1.4			
	740			21.0	0.4					
63	0	-0.3	24.4	0.2	0.2			167.6	1.95	-13.2
	160					68.6	0.6			
	470					91.5	1.7			
	740			13.1	0.2					
64	0	4.5	1.6	-4.4	0.5			11.1	1.11	1.2
	60									
	230					94.6	1.4			
	740			105.9	2.9					
65	0	4.5	1.7	-4.4	1.0			11.3	1.10	1.7
	60									
	230					95.7	1.6			
	740			102.4	7.5					

Run	Level above inlet	Sub-cooling	N_2-liquid inlet flow	Quality		Void fraction		Mass-flux	Heat-flux	Wall temp.
		Δt_{sub}	$\dot{m}$	x	s	α	s	G	q^*	t_w
	mm	°C	g/s	%	%	%	%	kg/m^2s	W/cm^2	°C
66	0	3.6	1.7	-3.6	0.9			11.4	1.18	2.6
	60					58.7	2.2			
	230					94.0	1.0			
	740			110.8	7.8					
67	0	4.3	5.2	-4.2	0.2			35.5	1.47	-5.8
	60									
	230					90.4	2.1			
	740			41.5	1.2					
68	0	4.4	5.5	-4.3	0.2			38.1	1.46	-5.5
	60									
	230					89.5	2.3			
	740			37.9	0.5					
69	0	4.6	6.0	-4.5	0.3			41.1	1.54	-8.9
	60					30.4	1.6			
	230					90.0	1.0			
	740			36.8	0.4					
70	0	4.5	8.1	-4.4	0.2			55.6	1.56	-8.0
	60									
	230					82.9	1.8			
	740			26.5	0.3					
71	0	4.6	8.6	-4.5	0.1			58.9	1.55	-7.8
	60									
	230					80.6	1.4			
	740			24.4	0.3					
72	0	4.4	10.8	-4.3	0.2			74.4	1.67	-9.9
	60									
	230					78.9	1.7			
	740			20.4	0.4					
73	0	4.2	11.2	-4.1	0.1			77.3	1.66	-11.3
	60					17.5	1.8			
	230					83.1	1.5			
	740			19.5	0.8					
74	0	4.6	14.7	-4.5	0.3			101.4	1.91	-11.3
	60					12.2	2.2			
	230					70.1	0.9			
	740			16.3	0.4					
75	0	4.1	2.0	-4.0	0.8			13.6	1.25	-3.4
	100					72.4	1.0			
	600					98.3	1.2			
	740			97.1	9.7					
76	0	4.1	4.2	-4.1	0.3			28.9	1.45	-5.7
	100					58.3	1.4			
	600					97.5	1.2			
	740			51.2	0.8					
77	0	4.3	5.5	-4.2	0.3			37.9	1.52	-8.7
	100					58.4	1.5			
	600					99.4	1.0			
	740			39.8	1.5					
78	0	4.1	5.8	-4.0	0.4			39.9	1.48	-10.0
	100					60.3	1.4			
	600					98.5	1.7			
	740			36.7	0.9					

Run	Level above inlet	Sub-cooling	H_2-liquid inlet flow	Quality		Void fraction		Mass-flux	Heat-flux	Wall temp.
		Δt_{sub}	$\dot{m}$	x	s	α	s	G	q"	t_w
	mm	°C	g/s	%	%	%	%	kg/m^2s	W/cm^2	°C
79	0	4.5	7.0	-4.4	0.1			47.8	1.44	-9.5
	100					49.9	1.3			
	600					96.3	1.5			
	740			28.9	1.5					
80	0	3.7	13.9	-3.6	0.2			95.4	1.89	-13.7
	100					25.7	1.5			
	600					98.0	0.9			
	740			18.2	0.1					
81	0	4.0	1.3	-3.9	2.5			8.6	0.87	4.9
	160					86.1	1.3			
	470					98.0	1.3			
	740			107.4	9.8					
82	0	3.7	1.5	-3.6	1.4			10.1	1.15	-1.5
	160					84.4	1.7			
	470					(101.7)	1.4			
	740			122.2	8.7					
83		4.7	1.8	-4.6	0.3			12.3	1.22	-4.0
	160					84.3	1.7			
	470					97.2	1.3			
	740			104.2	6.7					
84	0	4.7	1.9	-4.6	1.8			13.0	1.23	-1.5
	160					84.0	1.1			
	470					94.3	1.4			
	740			99.7	22.4					
85	0	4.9	3.1	-4.8	0.4			21.6	1.31	-5.8
	160					79.8	1.0			
	470					96.2	1.7			
	740			62.4	0.9					
86	0	4.0	4.3	-3.9	0.8			29.8	1.34	-5.3
	160					79.2	1.7			
	470					(99.1)	1.5			
	740			45.5	2.0					
87	0	3.9	5.9	-3.8	0.1			40.7	1.43	-7.1
	160					76.4	1.4			
	470					(99.7)	1.4			
	740			35.0	0.7					
88	0	3.4	6.9	-3.3	0.3			47.3	1.49	-8.2
	160					73.9	1.3			
	470									
	740			31.5	0.7					
89	0	4.1	10.6	-4.0	0.1			72.6		
	160					59.7	1.8			
	470					91.2	1.5			
	740									
90	0	6.8	1.4	-6.6	8.9			9.7	1.09	2.9
	45									
	310					95.6	1.2			
	740			116.0	12.9					
91	0	6.3	1.5	-6.2	1.6			10.1	1.20	-0.4
	45					50.1	1.6			
	310					92.5	1.5			
	740			125.0	6.6					

Run	Level above inlet	Sub-cooling	N_2-liquid inlet flow	Quality		Void fraction		Mass-flux	Heat-flux	Wall temp.
		Δt_{sub}	$\dot{m}$	x	s	α	s	G	q^*	t_w
	mm	°C	g/s	%	%	%	%	kg/m^2s	W/cm^2	°C
92	0	6.0	2.9	-5.9	0.6			20.0	1.34	-3.1
	45					39.3	1.4			
	310					91.9	1.2			
	740			67.8	0.9					
93	0	7.1	3.8	-7.0	0.6			26.0	1.40	-4.2
	45					31.7	1.5			
	310					90.2	1.2			
	740			52.2	0.9					
94	0	5.8	4.2	-5.6	0.5			29.0	1.45	-5.4
	45					31.2	1.4			
	310					90.7	1.9			
	740			49.6	1.0					
95	0	6.3	4.7	-6.2	0.5			32.4	1.46	-4.6
	45									
	310					91.8	1.3			
	740			43.5	0.6					
96	0	7.1	6.2	-6.9	1.7			42.9	1.50	-5.1
	45									
	310					88.7	1.2			
	740			31.6	1.4					
97	0	7.0	6.6	-6.9	0.2			45.0	1.61	-8.4
	45					20.8	1.8			
	310					87.7	1.1			
	740			32.5	0.5					
98	0	7.2	6.7	-7.1	2.1			45.9	1.58	-6.7
	45									
	310					86.7	1.8			
	740			30.7	1.9					
99	0	5.9	8.6	-5.8	0.3			59.4	1.73	-10.9
	45					13.3	1.7			
	310					85.4	1.2			
	740			26.3	0.4					
100	0	5.4	13.1	-5.3	0.1			90.0	1.82	-11.8
	45									
	310					78.5	1.5			
	740			17.0	0.2					
101	0	6.7	13.3	-6.6	0.1			91.2		
	45					4.5	1.6			
	310					75.5	1.4			
	740			16.6	0.4					
102	0	6.7	1.6	-6.6	1.4			11.0	1.26	-2.0
	60					55.9	1.4			
	230					94.6	1.2			
	740			119.8	3.5					
103	0	7.0	2.1	-6.8	0.7			14.1	1.23	-1.4
	60					56.2	2.2			
	230					94.4	1.0			
	740			89.2	2.1					
104	0	5.8	3.8	-5.6	0.7			26.1	1.45	-6.0
	60					44.9	2.2			
	230					93.1	1.0			
	740			55.6	2.2					

Run	Level above inlet	Sub-cooling	N_2-liquid inlet flow	Quality		Void fraction		Mass-flux	Heat-flux	Wall temp.
		Δt_{sub}	$\dot{m}$	x	s	α	s	G	q^*	t_w
	mm	°C	g/s	%	%	%	%	kg/m^2s	W/cm^2	°C
105	0	6.5	4.6	-6.3	0.1			31.6	1.45	-5.9
	60					38.1	1.6			
	230					93.0	1.1			
	740			44.1	0.9					
106	0	6.0	5.3	-6.6	0.3			36.6	1.52	-3.9
	60					29.8	2.2			
	230					84.6	0.6			
	740			39.2	0.8					
107	0	5.2	5.5	-5.1	2.3			37.9	1.49	-7.7
	60					30.6	1.6			
	230					91.7	1.1			
	740			38.3	2.4					
108	0	5.0	6.1	-4.9	0.6			42.0	1.54	-8.7
	60					27.0	2.0			
	230					89.0	0.8			
	740			35.3	0.6					
109	0	5.6	7.8	-5.4	0.2			53.7	1.65	-10.1
	60					25.1	1.9			
	230					88.7	0.8			
	740			28.4	0.5					
110	0	6.3	9.4	-6.2	0.1			64.8	1.77	-8.5
	60					13.7	2.3			
	230					77.1	1.0			
	740			23.9	0.2					
111	0	5.5	2.0	-5.4	0.7			13.4	1.17	-1.9
	100					72.5	1.8			
	600					99.1	1.1			
	740			91.1	7.4					
112	0	5.8	2.5	-5.7	0.4			17.2	1.25	-5.9
	100					70.7	1.6			
	600					101.1	1.4			
	740			74.1	2.6					
113	0	5.5	3.2	-5.3	0.7			21.7	1.34	-5.1
	100					65.4	1.2			
	600					96.9	0.9			
	740			62.7	1.3					
114	0	5.4	3.2	-5.3	0.2			21.8	1.31	-6.8
	100					62.6	1.0			
	600					97.9	1.8			
	740			60.8	1.6					
115	0	5.3	3.2	-5.2	1.0			22.0	1.36	-5.4
	100					64.7	1.2			
	600					97.4	0.9			
	740			62.7	1.4					
116	0	5.1	3.2	-5.0	0.7			22.1	1.35	-7.5
	100					63.0	1.2			
	600					99.6	1.5			
	740			62.0	4.7					
117	0	5.3	5.5	-5.2	0.4			37.6	1.53	-8.7
	100					54.2	1.0			
	600					98.1	1.6			
	740			39.5	0.8					

Run	Level above inlet	Sub-cooling	N_2-liquid inlet flow	Quality		Void fraction		Mass-flux	Heat-flux	Wall temp.
		Δt_{sub}	$\dot{m}$	x	s	α	s	G	q^*	t_w
	mm	°C	g/s	%	%	%	%	kg/m^2s	W/cm^2	°C
118	0	5.7	5.5	-5.6	0.2			37.7	1.48	-10.7
	100					56.8	2.2			
	600					98.4	2.3			
	740			37.7	0.7					
119	0	5.4	5.9	-5.3	0.3			40.6	1.54	-11.5
	100					53.9	1.1			
	600					100.0	1.3			
	740			36.4	0.5					
120	0	5.6	6.0	-5.4	0.1			41.1	1.43	-9.6
	100					53.0	1.4			
	600					98.1	1.7			
	740			33.0	1.1					
121	0	5.3	7.7	-5.2	0.5			52.8	1.68	-9.9
	100					41.7	2.1			
	600					97.0	2.5			
	740			29.8	0.7					
122	0	4.9	8.8	-4.8	0.7			60.3	1.74	-10.9
	100					36.5	2.3			
	600					96.3	1.2			
	740			26.9	0.6					
123	0	5.0	10.0	-4.9	0.3			69.1	1.81	-14.3
	100					30.9	2.7			
	600					100.3	1.4			
	740			24.0	0.5					
124	0	5.3	1.6	-5.2	1.5			10.8	1.16	0.1
	160					85.1	1.6			
	470					96.1	1.1			
	740			113.1	5.0					
125	0	5.4	3.8	-5.3	0.3			25.9	1.39	-6.9
	160					77.3	0.8			
	470					96.3	1.9			
	740			53.7	0.9					
126	0	5.3	4.5	-5.1	0.7			30.8	1.39	-7.1
	160					77.7	1.6			
	470					97.7	1.5			
	740			44.7	1.5					
127	0	6.5	7.1	-6.4	0.2			48.9	1.61	-8.6
	160					64.8	2.4			
	470					92.8	1.2			
	740			29.9	1.2					
128	0	5.8	7.2	-5.7	0.2			49.3	1.48	-9.2
	160					64.0	1.1			
	470					96.7	1.8			
	740			27.4	1.2					
129	0	5.7	7.8	-5.6	0.2			53.9	1.59	-11.2
	160					59.8	0.7			
	470					97.1	1.9			
	740			26.8	0.3					
130	0	5.3	8.4	-5.1	0.8			57.5	1.69	-10.4
	160					66.0	1.4			
	470					91.5	0.8			
	740			27.2	1.0					
131	0	6.1	9.8	-6.0	0.4			67.6	1.80	-12.4
	160					55.1	1.7			
	470					90.1	0.8			
	740			23.4	0.5					

Run	Level above inlet	Sub-cooling	N_2-liquid inlet flow	Quality	Mass-flux	Mean values		
						Quality	Heat flux	Wall temp.
		Δt_{sub}	$\dot{m}$	x	G	$\bar{x}$	$\bar{q}''$	$\bar{t}_w$
	mm	°C	g/s	%	kg/m^2s	%	W/cm^2	°C
301	0	-0.1	1.8	0.1	12.6	27.3	1.85	-9.1
	250			54.5		77.4	0.82	7.1
	725			100.4		60.1	1.17	1.5
302	0	-0.7	1.9	0.6	13.2	26.9	1.88	-9.2
	250			53.2		73.8	0.77	8.5
	725			94.4		57.6	1.15	2.4
303	0	-0.3	2.1	0.2	14.7	24.0	1.88	-9.4
	250			47.8		67.6	0.82	7.2
	725			87.4		52.6	1.18	1.5
304	0	-0.8	2.2	0.7	15.1	24.9	1.96	-10.7
	250			49.1		69.0	0.85	6.9
	725			89.0		53.8	1.23	0.8
305	0	-0.5	2.4	0.4	16.2	22.2	1.90	-9.6
	250			44.0		62.5	0.85	6.8
	725			81.1		48.6	1.21	1.1
306	0	-0.4	2.9	0.3	19.6	18.6	1.92	-10.2
	250			36.9		53.6	0.93	5.2
	725			70.4		41.5	1.27	-0.1
307	0	-0.7	3.1	0.6	21.3	17.6	1.94	-10.1
	250			34.7		50.4	0.95	5.2
	725			66.2		39.1	1.29	-0.1
308	0	-0.6	3.8	0.5	25.9	14.5	1.94	-10.2
	250			28.5		42.3	1.01	4.0
	725			56.1		32.7	1.33	-0.9
309	0	-0.5	4.3	0.4	29.5	12.7	1.94	-10.4
	250			25.0		37.0	1.00	4.0
	725			49.1		28.6	1.32	-1.0
310	0	-0.3	5.6	0.2	38.6	10.6	2.16	-8.7
	250			21.0		32.3	1.22	4.3
	725			43.6		24.8	1.54	-0.2
311	0	-0.4	6.4	0.3	43.9	8.7	1.97	-11.0
	250			17.1		26.7	1.19	0.1
	725			36.4		20.5	1.45	-3.7
312	0	-0.2	6.4	0.2	43.9	9.4	2.17	-8.9
	250			18.6		29.1	1.30	2.7
	725			39.7		22.3	1.60	-1.3
313	0	-0.3	7.4	0.2	51.0	8.2	2.19	-9.3
	250			16.2		25.6	1.35	1.6
	725			35.1		19.6	1.63	-2.2
314	0	-0.4	7.9	0.4	54.1	7.9	2.18	-9.5
	250			15.4		24.4	1.38	0.8
	725			33.5		18.7	1.65	-2.8
315	0	-0.4	7.9	0.3	54.3	7.7	2.17	-9.3
	250			15.2		24.3	1.39	0.6
	725			33.4		18.6	1.65	-2.8
316	0	-0.5	8.5	0.4	58.1	6.9	2.04	-12.2
	250			13.5		21.5	1.31	-2.1
	725			29.5		16.5	1.56	-5.6
317	0	-0.3	8.8	0.3	60.5	6.9	2.17	-9.1
	250			13.6		21.8	1.40	0.7
	725			30.1		16.7	1.66	-2.7

Run	Level above inlet	Sub-cooling	H_2O-liquid inlet flow	Quality	Mass-flux	Mean values		
						Quality	Heat flux	Wall temp.
		Δt_{sub}	$\dot{m}$	x	G	$\bar{x}$	$\bar{q}$	$\bar{t}_w$
	mm	°C	g/s	%	kg/m²s	%	W/cm²	°C
318	0	-0.3	10.9	0.2	74.9	5.7	2.22	-10.1
	250			11.3		18.6	1.17	4.4
	725			25.9		14.2	1.53	-0.6
319	0	-0.3	11.4	0.2	78.6	5.4	2.20	-9.7
	250			10.7		17.6	1.54	-1.0
	725			24.6		13.4	1.76	-4.5
320	0	-0.1	14.0	0.1	96.5	4.3	2.20	-9.5
	250			8.6		14.6	1.64	-3.3
	725			20.6		11.0	1.83	-5.4
321	0	-0.7	14.5	0.6	99.5	4.7	2.22	-10.3
	250			8.9		14.7	1.63	-3.7
	725			20.6		11.3	1.83	-6.0
322	0	-0.8	19.7	0.8	135.7	3.7	2.11	-13.0
	250			6.6		10.0	1.60	-6.9
	725			15.8		8.4	1.77	-9.0
323	0	5.6	1.7	-6.9	11.4	27.0	2.08	-10.5
	250			60.5		85.5	0.80	7.7
	725			110.6		65.6	1.21	1.4
324	0	4.4	1.8	-5.0	12.1	25.9	2.02	-10.8
	250			56.8		81.1	0.83	7.1
	725			105.4		62.1	1.24	0.9
325	0	5.3	2.1	-5.2	14.1	20.0	1.91	-10.4
	250			45.2		65.0	0.82	6.9
	725			86.4		50.0	1.29	0.9
326	0	4.3	2.4	-4.2	16.6	17.1	1.90	-10.8
	250			38.5		56.6	0.85	6.6
	725			74.7		43.0	1.21	0.9
327	0	5.3	2.6	-5.2	17.7	16.1	2.03	-11.2
	250			37.4		56.0	0.97	4.4
	725			76.2		42.0	1.33	-1.0
328	0	5.4	3.1	-5.3	21.2	12.0	2.06	-11.0
	250			31.0		47.5	0.98	4.2
	725			64.8		35.5	1.35	-1.3
329	0	5.5	3.8	-5.4	26.2	9.3	2.08	-12.2
	250			24.0		38.6	1.08	2.4
	725			53.2		28.5	1.42	-2.6
330	0	5.6	4.0	-5.5	27.6	8.0	2.01	-11.0
	250			21.5		36.0	1.13	1.4
	725			50.6		26.3	1.43	-2.9
331	0	4.1	4.0	-4.0	33.3	7.4	2.05	-12.3
	250			18.9		30.6	1.10	2.1
	725			42.4		22.6	1.42	-2.9
332	0	4.7	9.0	-4.6	61.6	1.7	2.10	-13.4
	250			8.0		15.8	1.35	-2.5
	725			21.6		10.9	1.60	-6.3
333	0	7.0	1.6	-6.9	10.8	23.1	1.75	-7.2
	250			53.0		74.2	0.65	9.7
	725			95.4		56.6	1.02	3.8
334	0	6.5	1.6	-6.4	10.9	26.9	1.96	-10.4
	250			60.2		85.4	0.77	7.8
	725			110.6		65.2	1.10	1.5

Run	Level above inlet	Sub-cooling	N_2-liquid inlet flow	Quality	Mass-flux	Mean values		
						Quality	Heat flux	Wall temp.
		Δt_{sub}	$\dot{m}$	x	G	$\bar{x}$	$\bar{q}''$	$\bar{t}w$
	mm	°C	g/s	%	kg/m²s	%	W/cm²	°C
335	0	7.1	1.6	-6.9	11.2	24.4	1.90	-10.4
	250			55.7		78.3	0.71	8.5
	725			101.0		59.7	1.12	2.0
336	0	6.2	1.7	-6.1	11.3	25.2	1.90	-9.5
	250			56.6		81.6	0.80	7.2
	725			106.7		62.2	1.17	1.4
337	0	5.7	2.4	-5.6	16.3	17.6	2.04	-1.5
	250			40.8		61.2	0.94	4.9
	725			81.6		46.2	1.31	-0.8
338	0	6.9	2.6	-6.8	17.7	15.1	2.09	-12.6
	250			37.1		56.5	0.97	4.1
	725			76.0		42.2	1.35	-1.7
339	0	6.0	3.4	-5.9	23.4	10.5	2.07	-12.1
	250			27.0		42.5	1.02	3.3
	725			58.1		31.5	1.38	-2.0
340	0	6.9	5.0	-6.7	34.2	4.7	2.11	-13.0
	250			16.2		28.5	1.19	0.0
	725			40.8		20.3	1.50	-4.5
341	0	6.0	5.5	-5.9	37.6	4.4	2.09	-13.5
	250			14.8		26.2	1.21	-0.2
	725			37.6		18.7	1.51	-4.8
342	0	6.5	6.0	-6.3	41.3	3.4	2.17	-13.9
	250			13.2		24.1	1.27	3.1
	725			35.1		16.9	1.58	-2.8
343	0	6.7	8.0	-6.6	55.2	0.8	2.20	-14.3
	250			8.2		17.5	1.45	-4.5
	725			26.8		11.7	1.70	-7.9
344	0	6.7	10.7	-6.5	73.7	-0.6	2.34	-16.8
	250			5.2		12.4	1.51	-5.6
	725			19.7		7.9	1.79	-9.5
345	0	8.4	1.3	-8.3	8.8	31.6	1.90	-10.3
	250			71.6		98.8	0.67	9.3
	725			126.0		75.6	1.09	2.5
346	0	9.6	1.5	-9.5	10.1	24.3	1.84	-8.2
	250			58.2		81.8	0.67	9.9
	725			105.4		62.0	1.07	3.6
347	0	9.8	2.4	-9.6	16.6	14.1	2.12	-12.7
	250			37.9		58.6	0.97	4.7
	725			79.3		43.3	1.36	-1.3
348	0	8.0	3.1	-7.8	21.2	11.6	2.20	-13.9
	250			31.0		49.3	1.09	2.6
	725			67.7		36.3	1.46	-3.0
349	0	8.3	3.1	-8.2	21.2	10.9	2.18	-13.5
	250			30.0		48.3	1.09	2.5
	725			66.6		35.4	1.46	-3.0
350	0	9.7	3.5	-9.6	24.2	7.4	2.21	-14.1
	250			24.5		40.3	1.07	2.8
	725			56.1		28.9	1.46	-3.0
351	0	9.5	4.0	-9.4	27.8	4.9	2.14	-12.9
	250			19.3		33.8	1.14	1.6
	725			48.4		23.8	1.48	3.4

Run	Level above inlet	Sub-cooling	N_2-liquid inlet flow	Quality	Mass-flux	Mean values		
						Quality	Heat flux	Wall temp.
		Δt_{sub}	$\dot{m}$	x	G	$\bar{x}$	$\bar{q}''$	$\bar{t}_w$
	mm	°C	g/s	%	kg/m^2s	%	W/cm^2	°C
352	0	7.7	4.3	-7.6	29.3	5.6	2.08	-13.6
	250			18.8		31.9	1.09	1.6
	725			45.1		22.8	1.43	3.6
353	0	8.8	4.9	-8.7	33.4	3.9	2.27	-14.8
	250			16.6		29.8	1.24	0.0
	725			43.0		20.9	1.59	-5.1
354	0	8.3	5.3	-8.1	36.3	2.9	2.15	-14.5
	250			13.9		25.7	1.21	-0.6
	725			37.6		17.8	1.53	-4.6
355	0	9.2	5.4	-9.1	37.3	0.9	2.01	-12.5
	250			10.9		21.6	1.12	0.9
	725			32.3		14.5	1.42	-3.7
356	0	9.2	6.0	-9.0	41.0	1.7	2.36	-16.6
	250			12.4		23.9	1.33	-1.6
	725			35.4		16.2	1.68	-6.8
357	0	9.4	6.1	-9.2	41.7	1.4	2.39	-17.0
	250			12.1		23.5	1.35	-1.9
	725			35.0		15.9	1.70	-7.10
358	0	8.6	11.0	-8.5	75.4	-2.7	2.34	-18.1
	250			3.0		10.1	1.51	-5.9
	725			17.2		5.7	1.79	-10.1

Sales distributors:
Jul. Gjellerup, Sølvgade 87,
DK-1307 Copenhagen K, Denmark

Available on exchange from:
Risø Library, Risø National Laboratory,
P. O. Box 49, DK-4000 Roskilde, Denmark

ISBN 87-550-0689-2
ISSN 0106-2840